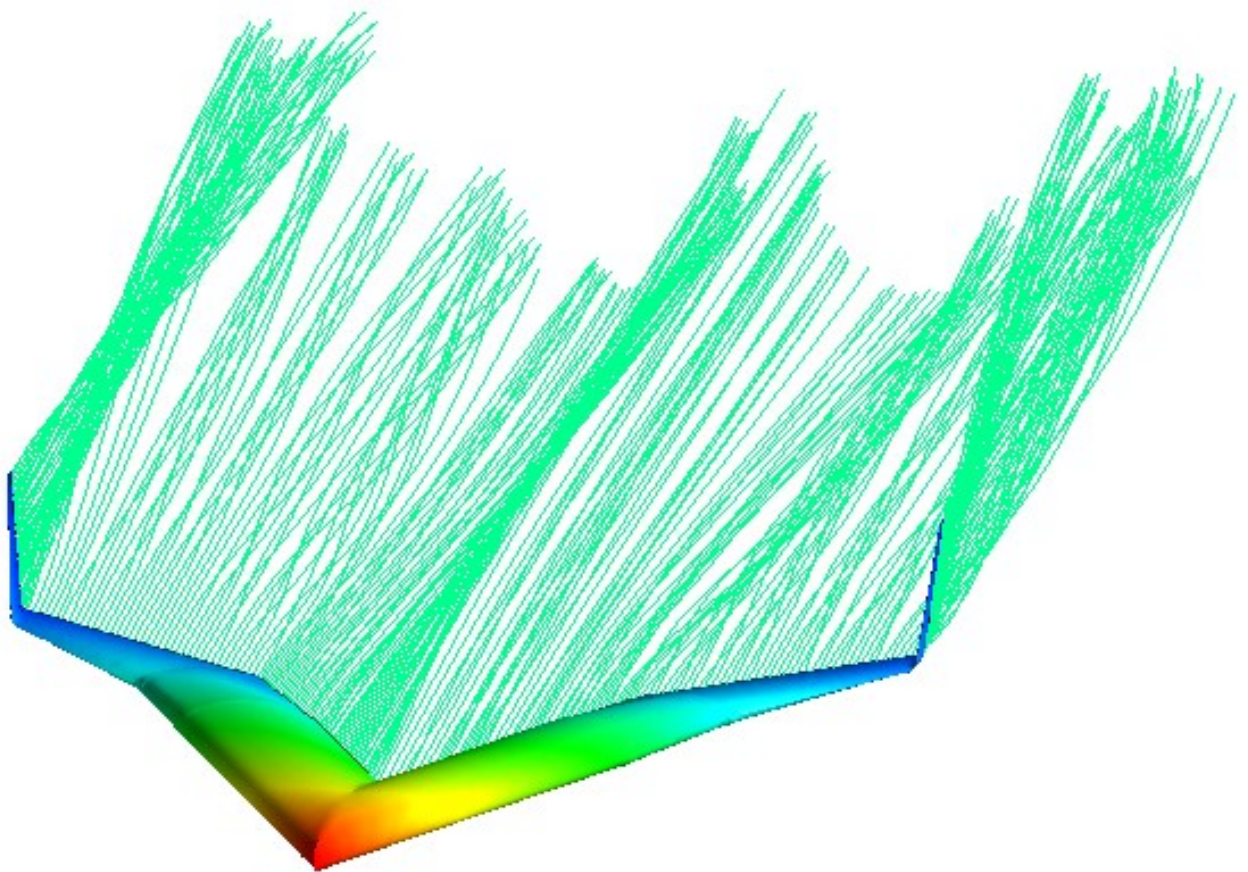


Parametric design of the Flying-V Winglets for Improved Lateral-Directional Stability and Control

J.M.T. Horwitz

Technische Universiteit Delft



Parametric Design of the Flying-V Winglets for Improved Lateral-Directional Stability and Control

by

J.M.T. Horwitz

in partial fulfillment of the requirements for the degree of

Master of Science
in Aerospace Engineering

at the Delft University of Technology,
to be defended publicly on Tuesday June 15, 2021 at 15:00 CEST.

Student number: 4784332
Project duration: June 29, 2020 – June 15, 2021
Thesis committee: Dr. ir. R. Vos, TU Delft, supervisor
Prof. dr. ing. G. Eitelberg, TU Delft
Ir. O. Stroosma, TU Delft

An electronic version of this thesis is available at <http://repository.tudelft.nl/>.

Equivalent word count: 25 081

Summary

With climate change a more pressing issue than ever before, the development of more sustainable methods of air transport is of paramount importance to the future of life on our planet. The Flying-V is a flying wing concept designed to have the same passenger capacity and cruise speed as the Airbus A350-900, but with potential fuel use reductions in excess of 20%. This makes it a strong candidate for more sustainable air transport in the near future.

Recent studies investigating the stability and control characteristics of the aircraft showed inadequacies impacting its lateral-directional handling qualities. The current work attempts to address these issues by means of a parametric design study of the Flying-V winglets, in order to determine how the geometry of the outboard wing and winglet affects the lateral-directional stability and control characteristics of the aircraft. The metrics analyzed in the research are the side force derivative $C_{y\beta}$, the rolling moment due to sideslip $C_{l\beta}$, the yawing moment due to sideslip $C_{n\beta}$ and N_β , the aerodynamic efficiency C_L/C_D , the lateral control departure parameter, $C_{n\beta_{DYN}}$, and the yawing moment due to rudder deflection $C_{n\delta_r}$. The objective of the research presented is to determine the values of the parameters defining the outboard wing and winglet geometry that will produce satisfactory lateral-directional stability and control characteristics for the aircraft. The parameters chosen to define the outer wing and winglet geometry are the winglet length, winglet cant angle, winglet leading edge sweep angle, winglet taper ratio, and the overall wing taper ratio.

A parametric definition of the winglet geometry is devised and implemented within the framework of the knowledge based engineering environment ParaPy. A space-filling Latin Hypercube sampling plan of 50 random winglet geometries is generated and each configuration is analyzed using the aerodynamic solver FlightStream. A Kriging approximation model is constructed from the aerodynamic data extracted from FlightStream in order to generate a global model and analyze how altering each design variable affects the lateral-directional stability and control characteristics of the aircraft.

A combination of increased winglet length, low cant angles, and low sweep angles result in the greatest improvements in static directional stability as compared to the baseline aircraft without winglets. Due to the strong lateral stability of the Flying-V wing alone, all winglet geometries tested and modeled exhibit strong lateral stability. The winglet taper ratio and wing taper ratio are shown to have a limited effect on these characteristics.

Given the trends determined in the current research, a winglet geometry with satisfactory stability and control performance that maximizes aerodynamic efficiency is presented as a recommendation for a starting point in future research. The recommended winglet is 10.9 m in length, has 0° of outboard cant angle, a leading edge sweep angle of 25° , a winglet taper ratio 0.65, and a wing taper ratio of 0.15. The Flying-V configuration with this winglet geometry exhibits strong lateral stability, satisfactory directional stability from an analysis of N_β , an increase in C_L/C_D of 13.4% over the baseline aircraft without winglets, and is not shown to be susceptible to departure from a preliminary analysis of the lateral control departure parameter and $C_{n\beta_{DYN}}$. Satisfactory yawing moment due to rudder deflection is not achieved for any winglet within the design space of the current research. As the winglet taper ratio and wing taper ratio were seen to have a limited effect on the stability and control characteristics of the aircraft, these values can be modified in future work to optimize lift and drag characteristics of the Flying-V.

Contents

Summary	iii
List of Figures	vii
List of Tables	ix
Nomenclature	xi
1 Introduction	1
1.1 Background and motivation	1
1.2 Research objectives and questions	2
1.3 Report structure	2
2 Stability and Control	5
2.1 Definitions and sign conventions	5
2.2 Static lateral-directional stability	5
2.2.1 Lateral-directional stability derivatives	5
2.2.2 Factors influencing stability derivatives	8
2.3 Dynamic lateral-directional stability	9
2.3.1 Spiral mode	9
2.3.2 Rolling mode	10
2.3.3 Dutch roll mode	10
2.4 Lateral-directional control	10
2.4.1 Lateral control mechanisms	10
2.4.2 Directional control mechanisms	11
3 Research Methodology	13
3.1 Winglet parametrization	13
3.1.1 ParaPy framework	14
3.2 Design exploration and performance analysis	17
3.2.1 Approach	17
3.2.2 Implementation	18
4 Validation	21
4.1 Surface mesh sensitivity study	21
4.2 FlightStream as aerodynamic solver	22
4.2.1 Validation using NACA wind tunnel data	22
4.2.2 Comparison to previous analyses of Flying-V	23
4.3 Kriging approximation model	24
5 Results	27
5.1 Winglet-off analysis of baseline aircraft	27
5.2 Side force due to sideslip	28
5.3 Rolling moment due to sideslip	31
5.4 Yawing moment due to sideslip	34

5.5	Lift-to-drag ratio	38
5.6	Lateral control departure parameter	40
5.7	Yawing moment due to rudder deflection	43
5.8	Winglet geometry recommendation for future work	44
6	Conclusions and Recommendations	47
6.1	Conclusions	47
6.2	Recommendations for future work	49
	Bibliography	51
A	UML Class Diagram	53
B	Sampling Plan	55
C	FlightStream Data	59

List of Figures

1.1	Flying-V configuration from conceptual study by Benad	2
1.2	Flying-V planform modification from aerodynamic design optimization study by Faggiano	2
2.1	Sideslip angle convention	6
2.2	Yaw angle, yawing moment, yaw rate, and side force convention	6
2.3	Bank angle, rolling moment, and roll rate convention	6
2.4	Illustration of moment arm of forces acting on wing when aircraft subjected to sideslip	8
3.1	Flying-V winglet	14
3.2	Blend axis construction	15
3.3	Blend trunk construction, front view	16
3.4	Isometric view of winglet trunk construction	16
3.5	Positioning of global and local reference coordinate systems in FlightStream	19
3.6	Flap effectiveness parameter	20
4.1	Surface mesh sensitivity study results	21
4.2	Plain wing: NACA wind tunnel data compared to FlightStream data	23
4.3	Cambered, twisted wing: NACA wind tunnel data compared to FlightStream data	23
4.4	Comparison of spanwise lift distributions from FlightStream and a RANS analysis	24
5.1	Influence of winglet length, cant angle, and leading-edge sweep angle on $C_{y\beta}$	28
5.2	Influence of winglet taper ratio on $C_{y\beta}$	29
5.3	Influence of wing taper ratio on $C_{y\beta}$	30
5.4	Influence of winglet length, cant angle, and leading-edge sweep angle on $C_{l\beta}$	31
5.5	Influence of winglet taper ratio on $C_{l\beta}$	32
5.6	Influence of wing taper ratio on $C_{l\beta}$	33
5.7	Influence of winglet length, cant angle, and leading-edge sweep angle on $C_{n\beta}$	34
5.8	Influence of winglet taper ratio on $C_{n\beta}$	35
5.9	Influence of wing taper ratio on $C_{n\beta}$	36
5.10	Influence of winglet length, cant angle, and leading-edge sweep angle on N_β	37
5.11	Influence of winglet length, cant angle, and leading-edge sweep angle on C_L/C_D	38
5.12	Influence of winglet taper ratio on C_L/C_D	39
5.13	Influence of wing taper ratio on C_L/C_D	40
5.14	Influence of winglet length, cant angle, and leading-edge sweep angle on LCDP	41
5.15	Weissman Departure and Spin Susceptibility Criterion	42
5.16	Influence of winglet length, cant angle, and leading-edge sweep angle on $C_{n\delta_r}$	44
A.1	UML class diagram of Flying-V ParaPy model	53
B.1	Sampling Plan: Samples 1-25	57
B.2	Sampling Plan: Samples 26-50	58

List of Tables

2.1	Summary of stability derivatives and the conditions for <i>static</i> stability	7
3.1	Upper and lower bounds of winglet and wing parameters defining design space	14
3.2	Quantities describing wing of FV-1000 model without winglets	18
4.1	Comparison of Flying-V aerodynamic efficiency at $M = 0.85$, $\alpha = 2.5^\circ$	24
4.2	RMSE values corresponding to the different correlation and regression models for each output	26
5.1	Wing parameters of FV-1000 model without winglets used for aerodynamic coefficient calculation	27
5.2	Lateral-directional stability coefficients for baseline aircraft without winglets	27
5.3	Ranking of parameters influencing $C_{y\beta}$ based on activity parameter θ	28
5.4	Ranking of parameters influencing $C_{l\beta}$ based on activity parameter θ	31
5.5	Ranking of parameters influencing $C_{n\beta}$ based on activity parameter θ	34
5.6	Ranking of parameters influencing C_L/C_D based on activity parameter θ	38
5.7	Ranking of parameters influencing LCDP based on activity parameter θ	41
5.8	Ranking of parameters influencing $C_{n\delta_r}$ based on activity parameter θ	43
5.9	Recommended values of winglet design variables for future work	45
5.10	Stability and control metrics predicted for recommended winglet geometry	45
B.1	Parameters defining the 50 samples used to construct the Kriging approximation model	56
C.1	Raw data from analysis of 50 samples in FlightStream at $C_L = 0.80$, $M = 0.2$, sea level standard conditions; X_{ref} at forward CG location, $S_{ref} = 927.11 \text{ m}^2$, $\bar{c} = 18.23 \text{ m}$ (longitudinal reference length), $b_{ref} = 64.6 \text{ m}$ (lateral reference length)	60
C.2	Raw data from analysis of 50 samples in FlightStream at $C_L = 0.80$, $M = 0.2$, sea level standard conditions; X_{ref} at aft CG location, $S_{ref} = 927.11 \text{ m}^2$, $\bar{c} = 18.23 \text{ m}$ (longitudinal reference length), $b_{ref} = 64.6 \text{ m}$ (lateral reference length)	61

Nomenclature

Roman Symbols

\bar{c}	Mean aerodynamic chord	[m]
ℓ_{wl}	Winglet length	[m]
\hat{y}	Set of predicted responses from surrogate model at test data sites	[–]
b	Wing span	[m]
c	Chord length	[–]
C_D	Drag coefficient	[–]
C_L	Lift coefficient	[–]
C_l	Rolling moment coefficient	[–]
c_l	Section lift coefficient	[–]
C_m	Pitching moment coefficient	[–]
C_n	Yawing moment coefficient	[–]
C_y	Side force coefficient	[–]
I_x	Moment of inertia about the body-fixed x-axis	[kg m ²]
I_z	Moment of inertia about the body-fixed z-axis	[kg m ²]
L	Rolling moment	[N]
m	Aircraft mass	[m]
N	Yawing moment	[N]
n_t	Size of test data set	[–]
q	Dynamic pressure	[Pa]
R_b	Winglet blend radius	[m]
S	Wing reference area	[m ²]
V_v	Vertical tail volume ratio	[–]
Y	Side force	[N]
y	Set of test data, acquired from direct analysis in FlightStream	[–]

Greek Symbols

α	Angle of attack	[deg]
β	Sideslip angle	[deg]
η_v	Tail efficiency factor	[–]
λ_{wing}	Wing taper ratio	[–]

Λ_{wl}	Winglet leading-edge sweep angle	[deg]
λ_{wl}	Winglet taper ratio	[-]
τ	Flap effectiveness parameter	[-]
θ	Kriging correlation model parameter	[-]
φ	Winglet cant angle	[deg]

Subscripts

α	Derivative with respect to angle of attack	[1/rad]
β	Derivative with respect to sideslip angle	[1/rad]
δ_α	Derivative with respect to aileron deflection	[1/rad]
δ_r	Derivative with respect to rudder deflection	[1/rad]
p	Derivative with respect to roll rate	[s/rad]
r	Derivative with respect to yaw rate	[s/rad]

Introduction

The air transport sector accounts for more than 3.6 % of the anthropogenic carbon emissions globally. With the total number of passenger-kilometers increasing by approximately 5 % each year, climate scientists predict increases in CO₂ and NO_x emissions in excess of 21 % and 16 %, respectively, by the year 2040 [1]. Technological developments, the use of sustainable biofuels, and continuing fleet renewal efforts have offset some of the environmental impact resulting from this growth. However, an apparent plateau in terms of efficiency for conventional ‘tube and wing’ aircraft, a category encompassing nearly all transport aircraft in operation today, has been driving researchers and aircraft manufacturers to consider unconventional aircraft configurations to address pressing climate change concerns. The Flying-V, under development in an ongoing project at TU Delft in collaboration with Airbus and KLM, is one such unconventional configuration that has shown promising results, with current estimates indicating a fuel reduction of 20% over the Airbus A350-900, considered one of today’s most advanced aircraft.

1.1. Background and motivation

The Flying-V concept began as TU Berlin student J. Benad’s thesis project in collaboration with Airbus Operations GmbH [2]. Benad proposed a pure flying wing that utilizes the volume within the wing for commercial passenger and cargo transport. The aircraft as proposed in [2] is shown in Figure 1.1. The aircraft was designed to have the same passenger capacity and cruise speed as the Airbus A350-900, but with considerable improvements in terms of performance. Preliminary estimations showed a 10 % increase in aerodynamic efficiency (C_L/C_D), and a 2 % decrease in operating empty weight, as compared to the A350-900. The configuration offered additional advantages including compactness, simplicity, reduced noise pollution, and an elliptical lift distribution in trimmed cruise. Notable changes to the design were made during an aerodynamic design optimization study by F. Faggiano at TU Delft [3], in which the planform shape was modified to more closely resemble its current design, as shown in Figure 1.2. An additional reduction in subsonic drag of 12 % and an improved lift-to-drag ratio of 23.7 at design cruise conditions were achieved. Faggiano also performed a preliminary study on the design of the aircraft’s rudder-incorporated winglets, which provide directional stability and control in addition to improved aerodynamic efficiency.

More recent studies investigating the stability and control characteristics of the Flying-V [4] have shown inadequacies that may significantly impact the handling qualities of the aircraft. A flight mechanics analysis using linearized aerodynamic models of the Flying-V with rudder-incorporated winglets revealed a number of distinct issues relating to stability and control, namely:

- Excessive rolling moment due to sideslip (dihedral effect)
- Insufficient natural yaw damping of the aircraft
- Insufficient rudder (yaw) control of the aircraft

The compounding of these issues indicates an inadequacy in lateral-directional handling qualities of the aircraft. Excessive dihedral, in combination with deficient yaw damping, may produce unstable yaw-roll coupling and a tendency for the aircraft to Dutch roll. Insufficient rudder control may pose prob-

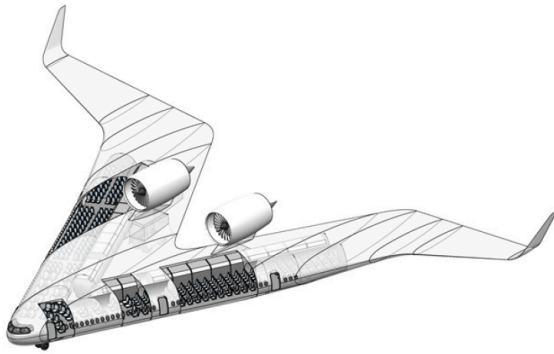


Figure 1.1: Flying-V configuration from conceptual study by Benad [2] ¹

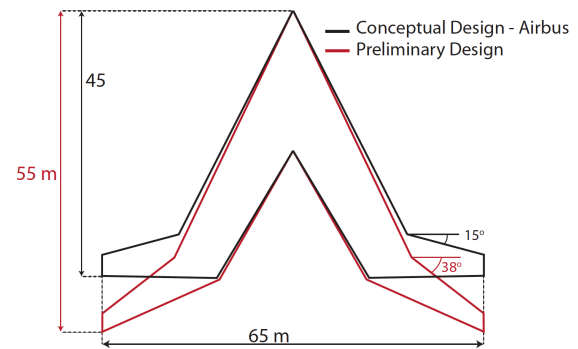


Figure 1.2: Flying-V planform modification from aerodynamic design optimization study by Faggiano [3] ²

lems when considering critical flight conditions including one engine inoperative (OEI) and maximum crosswind landing.

Given this information, a dedicated study into the influence of the outer wing and winglet geometry on the aerodynamics affecting the lateral-directional stability and control characteristics of the Flying-V is an important next step to further developing the project. It is therefore also the main focus of the current research task.

1.2. Research objectives and questions

With the problem posed as discussed above, the objective of the research task becomes clear: **to analyze how the geometry of the outboard wing and winglet of the Flying-V affects the lateral-directional stability and control characteristics of the aircraft.** Additionally, the effect on the aerodynamic performance of the aircraft will be measured. In pursuit of this goal, a set of sub-objectives are defined:

- Determine how the geometry of the winglets will be parametrized and defined.
- Analyze the pertinent aerodynamic coefficients of a set of winglet designs using a suitable aerodynamic solver.
- Construct a surrogate model using the observed sample responses to generalize the effect of changes to each design variable.
- Establish winglet designs providing sufficient stability and control characteristics for use in future research.

Given these objectives, the main research question is then: **What outboard wing and winglet geometry will produce satisfactory lateral-directional stability and control characteristics for the Flying-V?** To answer this question, answers to the following sub-questions are sought:

1. Which parameters most effectively define the geometry and positioning of the winglet and outboard wing, and how will they be defined within the ParaPy framework?
2. Which aerodynamic coefficients are good indicators of an aircraft's stability and control characteristics, and what are their values (or thresholds) that generally indicate satisfactory performance?
3. How should a surrogate model be constructed to ensure a good global model of the wing and winglet design space?
4. How does each design variable affect the pertinent aerodynamic coefficients and stability and control characteristics of the Flying-V?

1.3. Report structure

In the following chapters, the research performed to answer the research questions is described in detail. Chapter 2 provides a description of the pertinent lateral-directional stability and control quantities

¹Image from J. Benad, *The Flying V*, URL: <https://www.jbenad.com/flyingv>, accessed 22 Aug., 2019

²Image from F. Faggiano, *Aerodynamic Design Optimization of a Flying V Aircraft*, 2016, accessed 22 Aug., 2019

that are assessed in the current research, as well as some of the factors that influence them. Chapter 3 outlines the research methodology, including strategies for parametrizing and generating, as well as analyzing, various winglet geometries. Chapter 4 describes the validation exercises performed on the tools and procedures used in the current research task. Chapter 5 presents the results from the aerodynamic analysis of the winglet geometries and highlights trends and important observations found in the data. Finally, the conclusions drawn from the study, as well as recommendations for future work, are discussed in Chapter 6.

2

Stability and Control

The following sections outline pertinent lateral-directional stability and control quantities, their sign conventions, and some of the factors influencing them.

2.1. Definitions and sign conventions

The angles, moments, forces, and rates describing the lateral-directional motion of an aircraft are defined below; their corresponding sign conventions are illustrated in Figures 2.1 to 2.3.

Sideslip angle β : The angle between the relative wind vector (also the aircraft velocity vector or flight-path tangent) and the aircraft center line (body-fixed x -axis); it is positive nose-left, i.e., when the relative wind is approaching the aircraft from the right side.

Yaw (heading) angle ψ : The angle between the aircraft center line (body-fixed x -axis) and an arbitrarily chosen heading direction; it is positive nose-right. The *yaw rate* is denoted by r .

Bank (roll) angle ϕ : The angle between the body-fixed y -axis and the horizontal; it is positive right (starboard) wing down. The roll rate of the aircraft is denoted by p .

Yawing moment N : The moment about the yaw axis (body-fixed z -axis) of the aircraft; it is positive nose-right.

Side force Y : The force acting on the aircraft in the pitch axis (body-fixed y -axis); it is positive in the positive y -direction.

Rolling moment L : The moment about the roll axis (body-fixed x -axis) of the aircraft; it is positive if the moment acts to bring the left (port) wing down. Note that this is the opposite sign convention from that of the bank (roll) angle ϕ .

2.2. Static lateral-directional stability

Most generally, static stability is the rudimentary tendency of an aircraft to return to its initial state after a disturbance. It follows that the *lateral-directional* static stability of an aircraft indicates the tendency of an aircraft to return to equilibrium in the yaw (directional) and roll (lateral) axes after a disturbance in yaw or roll. Yawing and rolling forces and motions are often strongly coupled, making the analysis of these motions by and large more nuanced than that of longitudinal forces and motions. However, it is often useful to look at the lateral and directional derivatives separately to get a better understanding of how an aircraft may behave.

2.2.1. Lateral-directional stability derivatives

An aircraft is said to have static directional stability if an increase in sideslip angle β produces a yawing moment N that tends to restore the aircraft to symmetric flight. This restoring moment is the yawing moment due to sideslip; it is calculated as shown in equation 2.1a, and in nondimensionalized form as

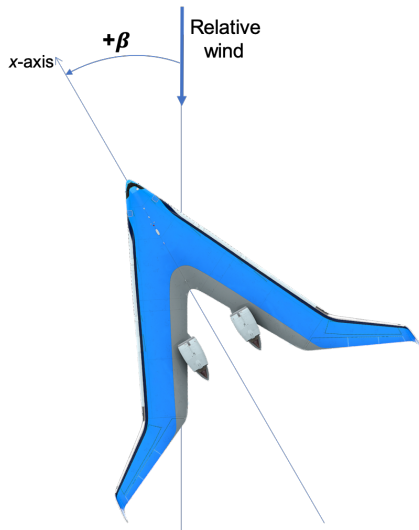


Figure 2.1: Sideslip angle (β) convention, viewed from above ¹

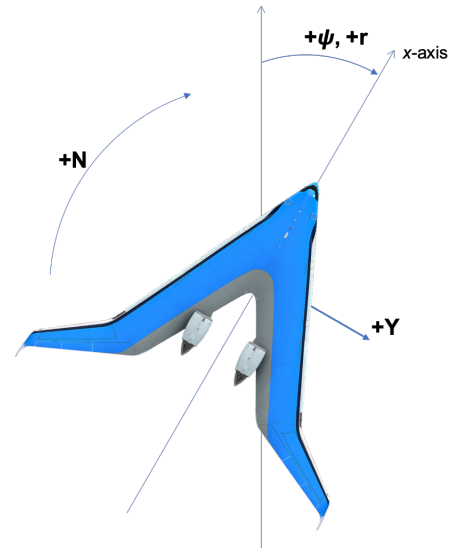


Figure 2.2: Yaw angle (ψ), yawing moment (N), yaw rate (r), and side force (Y) convention, viewed from above ¹

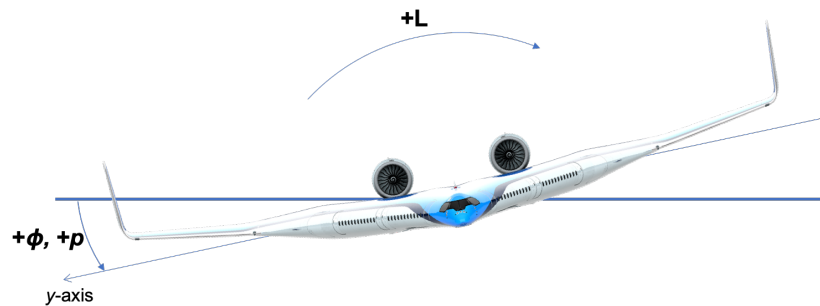


Figure 2.3: Bank angle (ϕ), rolling moment (L), and roll rate (p) convention, viewed from nose ¹

shown in equation 2.1b.

$$N_{\beta} = \frac{\partial N}{\partial \beta} \quad (2.1a)$$

$$C_{n_{\beta}} = \frac{\partial C_n}{\partial \beta} \quad (2.1b)$$

with C_n the nondimensional coefficient of the yawing moment N calculated as follows:

$$C_n = \frac{N}{qSb} \quad (2.2)$$

Using the sign conventions as previously defined, static directional stability requires N_{β} and $C_{n_{\beta}}$ be *positive*. The dimensional derivative N_{β} and nondimensional derivative $C_{n_{\beta}}$ are related as shown in equation 2.3.

$$N_{\beta} = \frac{qSbC_{n_{\beta}}}{I_z} \quad (2.3)$$

¹Images of Flying-V from <https://www.tudelft.nl/lr/flying-v/>

Similarly, an increase in sideslip angle β should produce a restoring side force Y ; this is the side force due to sideslip, calculated as shown in equation 2.4a and nondimensionalized in equation 2.4b.

$$Y_\beta = \frac{\partial Y}{\partial \beta} \quad (2.4a)$$

$$C_{y\beta} = \frac{\partial C_y}{\partial \beta} \quad (2.4b)$$

with C_y the nondimensional coefficient of the side force Y . For stability, Y_β and $C_{y\beta}$ should be *negative*. The dimensional derivative Y_β and nondimensional derivative $C_{y\beta}$ are related as shown in equation 2.5.

$$Y_\beta = \frac{qSbC_{y\beta}}{m} \quad (2.5)$$

An aircraft is said to have static lateral stability if an increase in sideslip angle β produces a rolling moment L that tends to bring the wings level. Static lateral stability is usually framed in terms of the dihedral effect or the effective dihedral, which is measured as the rolling moment due to sideslip, calculated as shown in equation 2.6a and nondimensionalized in equation 2.6b.

$$L_\beta = \frac{\partial L}{\partial \beta} \quad (2.6a)$$

$$C_{l\beta} = \frac{\partial C_l}{\partial \beta} \quad (2.6b)$$

with C_l the nondimensional coefficient of the rolling moment L . Static lateral stability requires L_β and $C_{l\beta}$ be *negative*. The physical manifestation of this property requires, of an aircraft possessing lateral-directional stability, a right wing down bank angle to balance a nose-left (positive) sideslip angle. The dimensional derivative L_β and nondimensional derivative $C_{l\beta}$ are related as shown in equation 2.7.

$$L_\beta = \frac{qSbC_{l\beta}}{I_x} \quad (2.7)$$

The lateral-directional stability derivatives introduced above are collated in Table 2.1, along with the condition generally imposed on each for static lateral-directional stability of an aircraft. Note that satisfying these conditions does not guarantee stability of the aircraft. More specific recommendations have been given for the value of $C_{n\beta}$ [5]. A minimum value of $C_{n\beta} = 0.03$ is sometimes recommended, though a value this low generally leads to inadequate Dutch roll damping. The values of $C_{n\beta}$ for transport aircraft generally fall in the range from 0.10 to 0.25. More specific guidelines for the minimum recommended values of $C_{y\beta}$ and $C_{l\beta}$ were not found in literature. To better understand the target values of these stability derivatives in the initial design phase, a limited number of data points from existing handling quality data on representative contemporary transport aircraft are collected from literature [6, 7]. The aircraft sampled include the Boeing 747, Convair 880M, Lockheed Jetstar, Lockheed C-5A, and three unnamed subsonic jet transport aircraft. The average values of $C_{n\beta}$, $C_{y\beta}$, and $C_{l\beta}$ from this limited data set are included in Table 2.1. Note that this data set is limited due to the limited pool of data available in literature on the subject.

Table 2.1: Summary of stability derivatives and the conditions for *static* stability

Stability derivative	Condition for stability	Average observed
$C_{n\beta}$	positive	0.13
$C_{y\beta}$	negative	-0.80
$C_{l\beta}$	negative	-0.18

2.2.2. Factors influencing stability derivatives

Each of the above mentioned stability derivatives is influenced by many aspects of an aircraft's design. Much of the available research on the individual contributions of each aircraft component to the respective stability derivatives pertains predominantly to conventional 'tube-and-wing' aircraft. However, a lot can be applied when considering the components on the Flying-V serving the same or similar functions.

As with each of the stability derivatives, the directional stability derivative C_{n_β} is often estimated by a synthesis of contributions of the various components of an aircraft. The main contributions to C_{n_β} on a conventionally configured aircraft come from the fuselage and the vertical tail. The side area of the body forward of the CG is destabilizing; conversely, side area aft of the CG will have a stabilizing effect. Fortunately, the Flying-V, like many flying wings, does not suffer greatly from a destabilizing effect of the fuselage [4]. A vertical tail surface aft of the CG is stabilizing. The vertical tail area, as well as the moment arm of the vertical tail to the CG, determine the extent of the stabilizing contribution: the larger the vertical tail, and the greater the moment arm, the greater the positive effect on the aircraft's directional stability. To a lesser degree, the wing, CG position, engine position, and nacelles influence C_{n_β} . The wing, in particular the effect of wing sweepback, has a slight stabilizing effect due to the increased moment arm of the induced drag forces acting on the upwind wing, as illustrated in Figure 2.4. Introducing winglets on the wing also influences directional stability; the winglet geometry will determine the extent to which the winglet influences C_{n_β} . A parametric study on the effect of modifying winglet parameters on the lateral-directional stability derivatives of a generic wing showed the following [8]:

- Moving the winglet aftward and/or increasing winglet sweepback increases directional stability.
- Winglet incidence angle, cant angle, and length appear to have relatively little effect on directional stability.
- Keeping winglet parameters constant and modifying the wing parameters indicated that wing sweep and wing twist have an effect on the *winglet* contribution to directional stability: wing sweepback and washout increase directional stability. Wing span and wing taper ratio both have minimal effect.

Note that C_{n_β} will vary depending on the lift coefficient C_L (or angle of attack α), Mach number M , control surface (e.g., aileron, elevon) or flap deflection, and other influences. This is particularly true for higher angles of attack, when largely separated flow and leading edge vortices may significantly alter the flow field around the wing [9].

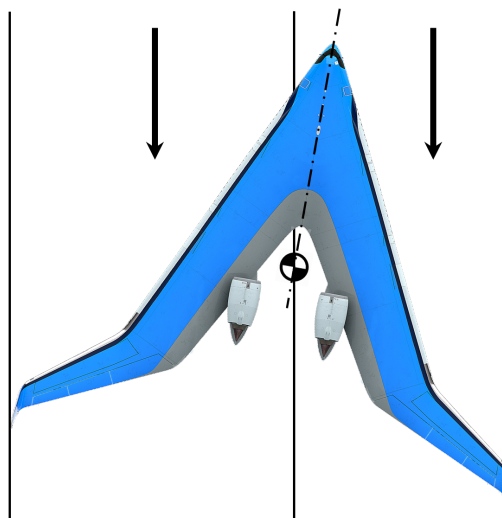


Figure 2.4: Illustration of moment arm of forces acting on wing when aircraft subjected to sideslip

The side-force derivative C_{y_β} is influenced largely in the same way as C_{n_β} . The main contributions come from the body side area and vertical stabilizing surfaces, with the wing having generally a lesser effect. The addition of winglets to the wing generally influences the side-force derivative in the same

way as $C_{n\beta}$ [8]. As with $C_{n\beta}$, the value $C_{y\beta}$ will vary depending on the lift coefficient, Mach number, control surface or flap deflection, and other influences.

The lateral stability derivative $C_{l\beta}$, like $C_{n\beta}$ and $C_{y\beta}$, is influenced by many aspects of an aircraft's design. The wing has the greatest influence on $C_{l\beta}$. The dihedral angle of the wing has a strong influence on the dihedral effect. A positive dihedral angle (*upward* from the horizontal) increases the effective dihedral of the aircraft, while a negative dihedral angle, or 'anhedral,' decreases the effective dihedral. The sweep angle of the wing may also have a significant influence on $C_{l\beta}$. The influence of sweepback is highly lift-dependent: at higher lift coefficients, the effect is notably greater than at lower lift coefficients. From aerodynamic theory, it's possible to estimate that for sweep angles on the order of 45° , and for large values of C_L , the wing sweepback could have a similar contribution to the effective dihedral as that of a wing with 10° geometric dihedral angle [10]. Additionally, introducing winglets on the wing also increases the dihedral effect; the winglet geometry will determine the extent to which the winglet influences $C_{l\beta}$. A parametric study on the effect of modifying winglet parameters on the lateral-directional stability derivatives of a generic wing showed the following [8]:

- increasing the winglet length and/or increasing outward cant angle of the winglet increases dihedral effect (outward cant also increases roll damping)
- winglet incidence angle has relatively little effect on the overall effective dihedral
- moving the winglet aftward and/or increasing winglet sweepback reduces the increment in dihedral effect
- keeping winglet parameters constant and modifying wing parameters indicated that wing sweep, wing twist, wing span, and wing taper ratio all have minimal effect on the *winglet* contribution to dihedral effect

Moreover, any vertical stabilizer or winglet surfaces with a center of pressure markedly offset from the CG and rolling axis of the aircraft may have a nontrivial rolling moment due to sideslip.

The above mentioned influences on the stability derivatives are based on trends observed in past research, and do not necessarily present a satisfactory means of determining these values. These aerodynamic coefficients, as well as trends observed in their values when altering the aircraft geometry, are determined for the Flying-V by means of aerodynamic flow solver in the current research. It's important to note that most changes to the aircraft geometry, particularly to the vertical tail surface area and the wing dihedral, will affect all stability derivatives, and as such these effects are studied across all pertinent stability derivatives [11].

2.3. Dynamic lateral-directional stability

The dynamic lateral-directional stability of the Flying-V is not analyzed in the current research. However, the static stability derivatives will influence the dynamic stability of the aircraft, so a brief explanation of the dynamic modes is provided. The dynamic lateral-directional response of an aircraft to a disturbance is strongly coupled in yawing and rolling motion; therefore, these responses are most often discussed in terms of three lateral-directional modes: the spiral mode, the rolling mode, and the Dutch roll mode. These three modes correspond to the roots of the characteristic equation for the lateral-directional motion of an aircraft. The two real roots correspond to the spiral and roll modes, and a pair of complex roots correspond to the Dutch roll mode.

2.3.1. Spiral mode

The spiral mode is one of the two exponential modes associated with the real roots of the characteristic equation. On a typical transport aircraft, the spiral mode may be stable or slightly unstable. In most cases, an unstable spiral mode poses few problems for piloted aircraft as the time constant is quite long. This mode is characterized by displacements in both roll and yaw, and when allowed to diverge results in a tightening spiraling motion of the aircraft. The aerodynamic coefficients most strongly influencing the spiral mode are the dihedral effect $C_{l\beta}$, directional stability derivative $C_{n\beta}$, yaw rate damping C_{nr} , and rolling moment due to yaw rate C_{lr} . Excessive directional stability $C_{n\beta}$ and insufficient dihedral effect $C_{l\beta}$ are generally the causes of an unstable spiral mode [11]; as such, increasing dihedral effect or yaw damping, or both, tend to stabilize the mode.

2.3.2. Rolling mode

The rolling mode is the second of the two exponential modes associated with the real roots of the characteristic equation. On a typical transport aircraft, the rolling mode is heavily damped and thus stable. The dynamic response of the aircraft in roll is described by this mode. The aerodynamic coefficient primarily influencing the rolling mode is the roll damping C_{l_p} .

2.3.3. Dutch roll mode

The Dutch roll mode is a damped oscillatory mode associated with the pair of complex roots of the characteristic equation. On a typical transport aircraft, the Dutch roll mode has a relatively short period and is often relatively lightly damped. This mode is characterized by a highly coupled oscillatory motion in roll, sideslip, and yaw, which can lead to discomfort for passengers and crew and may pose problems with aircraft certification if not properly addressed. The aerodynamic coefficients typically influencing the frequency and damping of the Dutch roll mode are the side force derivative C_{y_β} , yaw rate damping C_{n_r} , directional stability derivative C_{n_β} , and the side force due to yaw rate C_{y_r} . In particular, the relative values of directional stability and dihedral effect have a strong impact on the Dutch roll stability: excessive dihedral effect and insufficient directional stability tend to result in an aircraft susceptible to unstable Dutch roll oscillations, as was observed in a recent dynamic analysis of the current Flying-V design [4]. It is possible to actively damp these oscillations using a certifiable yaw damper, however the yaw damper must be shown to have a failure rate not greater than 10^{-9} .

Mass and inertia properties are required to perform a full dynamic analysis of the aircraft and to determine the time constraints and damping values of the dynamic lateral-directional modes. A full dynamic analysis is outside the scope of the current research. However, inertia properties from previous research [4] can be used to roughly estimate certain dynamic stability properties of the aircraft.

2.4. Lateral-directional control

Lateral-directional control surfaces are not modeled on the Flying-V in the current research. However, data from previous research may be used in combination with data collected to estimate empirically how the lateral and directional control capabilities of the Flying-V depend on the geometry of the aircraft's winglets.

2.4.1. Lateral control mechanisms

Lateral control on the Flying-V is achieved by deflecting control surfaces at the trailing edge of the wing. These control surfaces are deflected in opposite directions on either side of the wing, producing an asymmetric lift distribution that results in a rolling moment toward the upward deflected aileron. The trailing edge control surfaces on the Flying-V have been shown to provide sufficient lateral control power [4]. The lateral control power of an aircraft can be measured by the rolling moment produced due to aileron (or similar lateral control surface) deflection, $C_{l_{\delta_a}}$.

Potential issues arise when considering the phenomenon known as 'adverse' yaw, referring to the yawing moment induced when deflecting ailerons for roll control. This effect is most often unwanted as the yawing moment pushes the nose of the aircraft in the direction opposite of the intended turn. Unfortunately, flying wings are more susceptible to adverse yaw than their conventionally configured counterparts as they generally have weaker directional stability and little yaw damping; the lack of large vertical stabilizing surfaces drastically reduces resistance to sudden motions in yaw [12]. The danger includes the possibility of triggering potentially uncontrollable oscillations in yaw if the initial motion is large and the pilot or flight system overcorrects with directional control surfaces. Reduced effectiveness of the lateral control surfaces could also result from a combination of strong adverse yaw and large dihedral effect, particularly at lower speeds and high lift coefficients. A potential solution to these challenges is employing spoilers on the wing to aid in roll control, which could improve roll rates and limit adverse yaw [4]. Spoilers have not yet been modeled on the Flying-V, but they may be a relatively simple remedy if the adverse yaw challenge proves insurmountable with the directional control allocation and sizing on the aircraft.

2.4.2. Directional control mechanisms

Ensuring an aircraft has sufficient directional control capability is an essential step when analyzing handling qualities, particularly in critical conditions such as one engine inoperative (OEI) and maximum crosswind landing. Understanding how the geometry of the winglets and control mechanisms affects the control capability of the aircraft is an important step towards ensuring satisfactory handling qualities. The directional control power of an aircraft can be measured by the yawing moment produced due to rudder deflection, $C_{n_{\delta_r}}$.

Directional control on a conventionally configured transport aircraft is typically achieved by deflecting a rudder at the trailing edge of the vertical tail, sometimes referred to as a side-force rudder. The side force produced at the vertical tail in combination with a long lever arm to the CG produces a yawing moment to turn the nose in the desired direction. On flying wings with substantial sweepback, the wingtips are often the points on the aircraft farthest from the CG, making them the logical locations to place fins with yaw control devices incorporated. Rudder-incorporated winglets are currently employed for directional control on the Flying-V; however, in recent tests performed using a flight mechanics model to simulate aircraft performance in critical certification maneuvers, the lateral-directional control power of the Flying-V was deemed insufficient with the current control allocation and sizing [4]. In fact, the aircraft showed inadequate directional control power with rudder deflections at or exceeding the maximum deflection in one engine inoperative conditions for coordinated turn, bank to bank, and steady heading sideslip maneuvers. This does not necessarily mean that wingtip rudders cannot function as directional control devices for this configuration.

The parameters defining the geometry of the winglet, as well as the geometry of the control surface, likely have a strong influence on the effectiveness of the control surface. The current research attempts to quantify the effects of changing the winglet parameters on the directional control capabilities of the aircraft equipped with rudder-incorporated winglets.

3

Research Methodology

In the following sections, the strategies for winglet parametrization and geometry generation, as well as the methods for aerodynamic analysis and surrogate model generation, are discussed.

3.1. Winglet parametrization

In the initial aerodynamic design optimization of the Flying-V [3], three parameters were used to define the winglet: aspect ratio, leading edge sweep angle, and taper ratio. The root chord of the winglet was assumed to be equal to the wing tip chord, and the winglet was constrained to be vertical (i.e., 0° cant angle), as the total span of the wing was set to the prescribed gate limit. Additionally, the blending of the wing-winglet juncture was not considered in this initial study.

Common parameters used to define a winglet from design studies in literature include [8, 13, 14]: winglet length (or span), root chord length, taper ratio, aspect ratio, leading edge (or quarter chord) sweep angle, cant angle, toe angle, and twist angle. These parameters, as well as the parametrization method employed in building the parametric model within the ParaPy framework, were taken into consideration when determining the set of parameters chosen to define the Flying-V winglet.

In addition to the parameters already used to define the outboard wing, the winglet is fully defined by the following parameters:

- Winglet length, l_{wl}
- Cant angle, φ
- Winglet leading-edge sweep angle, Λ_{wl}
- Taper ratio, λ_{wl}
- Blend radius, R_b
- Winglet tip twist angle

The airfoils of the blended section and winglet trunk are assumed to be the same as the wing tip profile. This is common in winglet design studies to avoid the added complexity of including the airfoil parameters in the design space. The effect of the winglet twist is also not studied in the current research; this parameter has been shown to have marginal influence on the stability and control properties of a wing [8]. The winglet tip twist angle - relative to the winglet root twist - is fixed at 0° in the design study. Additionally, the winglet blend radius is fixed at 0.48 m - the value used in [4] - in the current design study, as this parameter will also have a relatively smaller influence on the stability and control characteristics. The airfoils, winglet twist, and blend radius may all be optimized in a future aerodynamic design study to minimize drag or modify the spanwise lift distribution of the wing.

Figure 3.1 shows an example of the Flying-V winglet geometry generated from the above parameters. Although the geometric definitions of these parameters generally align with what would be expected, as shown in the figure, special care is taken to explain how the above parameters translate to a geometric definition of the winglet in the geometry generation tool ParaPy in the following subsection.

The parameters included in the design study are collected in Table 3.1, along with their upper and lower bounds, and units. The bounds imposed on each parameter were chosen based on a number

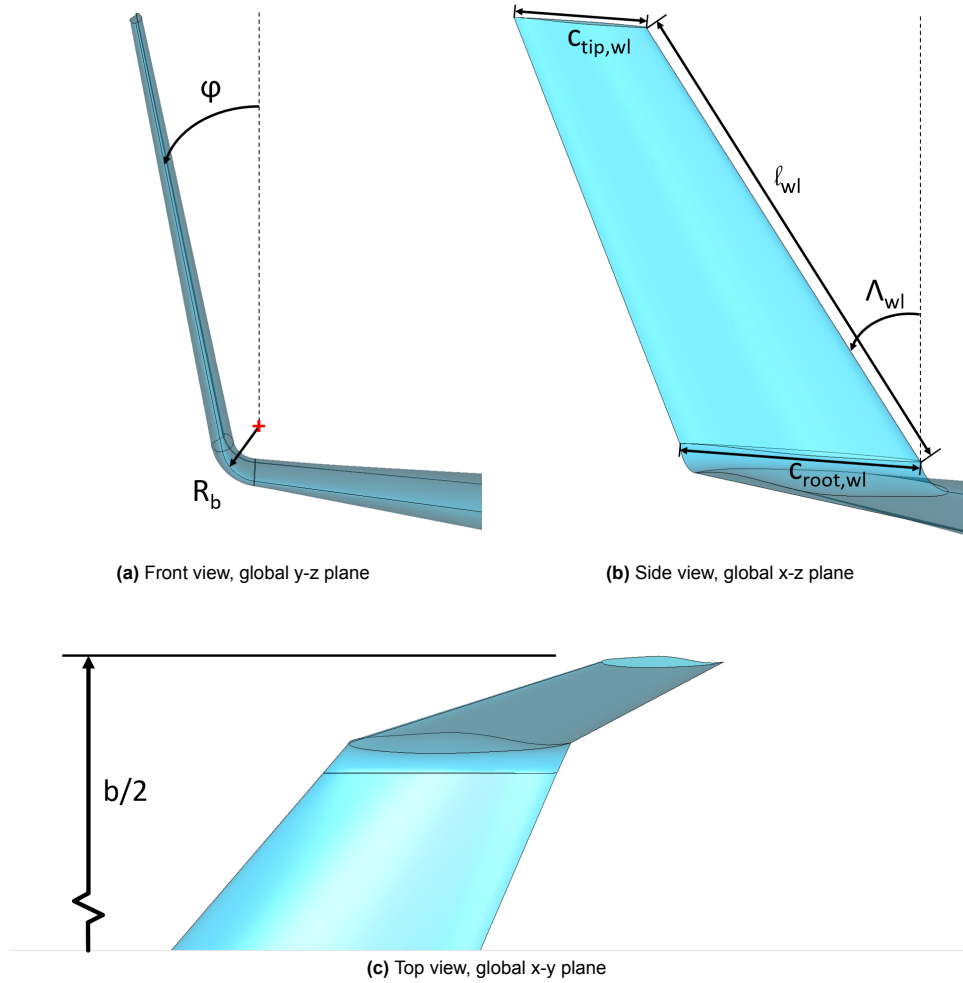


Figure 3.1: Flying-V winglet

of criteria, including the bounds from similar winglet design studies in recent years [15], restrictions imposed on the maximum height of the winglet tip from the cabin floor, the values used in previous studies of the Flying-V wing and winglet, as well as aerodynamic limitations and requirements.

3.1.1. ParaPy framework

Much of the previous work on the Flying-V, including the most recent parametric model definition of the aircraft, has used the knowledge based engineering (KBE) environment ParaPy as a tool to define and generate the geometry of the aircraft. The merging of computer aided design and object-oriented programming within a KBE system allows designers to visualize, analyze, and manipulate the geometry of an aircraft using unit basis three-dimensional parametric ‘building blocks’, often referred to as high level primitives, or HLPs [16, 17]. The `WingShapeTrunk` (super)class is one such HLP, from the new

Table 3.1: Upper and lower bounds of winglet and wing parameters defining design space

Parameter	Symbol	Lower bound	Upper bound	Unit
Length	ℓ_{wl}	3.0000	12.0000	[m]
Cant angle	φ	0.0000	45.0000	[deg]
Leading-edge sweep angle	Λ_{wl}	25.0000	55.0000	[deg]
Winglet taper ratio	λ_{wl}	0.3000	1.0000	[-]
Wing taper ratio	λ_{wing}	0.1125	0.1875	[-]

Flying-V parametrization established by M. Hillen [18], used in the current model to generate a wing trunk shape, and is defined by at least two airfoil profiles required as inputs. These airfoil profiles are themselves building blocks in the form of the `Aerofoil` or `OuterAerofoil` (super)classes, defined by parameters often characterizing airfoils, including chord length and 2-D airfoil curve, or alternatively, class function/shape function (CST) coefficients parametrizing the 2-D airfoil curve shape [19]. The `WingShapeTrunk` and `OuterAerofoil` classes form the basis for the geometric representation of the Flying-V winglet in ParaPy. The method employed to translate the winglet parameters listed above to a fully defined outer wing and winglet shape in ParaPy is as follows:

The outboard wing and winglet of the Flying-V are defined in the parametric model by three instances of the `WingShapeTrunk` class. The winglet, which consists of a blended section (blend trunk) and a winglet trunk, is constructed at the end of the most outboard wing trunk.

The blend trunk of the winglet is constructed by first defining a blend axis about which an extension of the outboard wing is bent (or folded) upwards to create the blended section. The blend axis and the blending radius are represented geometrically by an instance of the `Cylinder` class in ParaPy. The axis (i.e., the cylinder centerline direction vector, or alternatively, the z-direction of the cylinder orientation axes) is oriented to be parallel to the wingtip chord line direction vector, so as to account for the wingtip twist angle. The axis location is defined at a point translated one blending radius (equal to 0.48 m) from the wingtip quarter chord point in a direction normal to both the wingtip chord line direction vector and the projection of the wing leading edge rail on a plane normal to the blend axis, so as to account for the wing dihedral angle. Figure 3.2 shows the positioning of the cylinder instantiated to represent the blend axis.

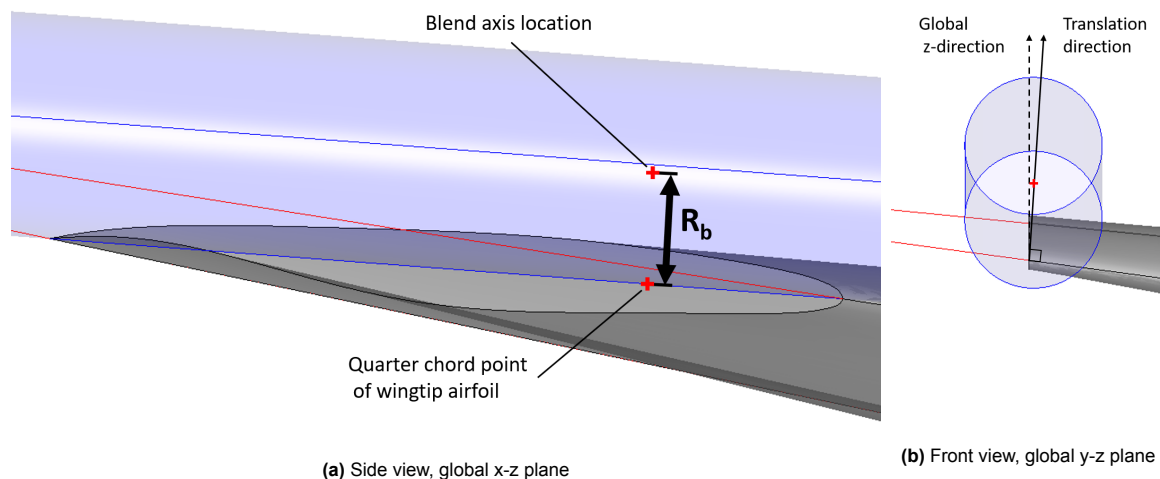


Figure 3.2: Blend axis construction

The outboard trunk of the wing is extended to create the leading edge and trailing edge lines that, when projected onto the blend cylinder, form the leading edge and trailing edge rails of the blended winglet trunk. The projected leading edge and trailing edge curves are split by a plane representing the cant angle of the winglet to make the final rails, as shown in Figure 3.3a; the green plane (the largest plane visualized in the figure) represents the ‘cant plane.’ These rails are then used to define a number of blend trunk profiles, each an instance of the `OuterAerofoil` class, with the help of a sequence of blend planes positioned from the outboard wingtip profile up to and including the cant plane. The number of blend planes, and therefore the number of blend profiles, is dictated by an input to the `Winglet` class. The CST coefficients defining the airfoil curve shape for each blend profile are set to match the CST coefficients of the wing tip; the chord length is measured as the distance between the intersection points of the leading edge and trailing edge rails and the blend plane defining that section. The blend planes and resulting blend profiles are shown in Figures 3.3a and 3.3b, respectively. Finally, the wingtip profile and blend profiles are used as inputs to create an instance of the `WingShapeTrunk` class that forms the blend trunk of the winglet, shown in Figure 3.3c.

The last profile of the blend trunk then becomes the root profile of the winglet trunk, and is the first

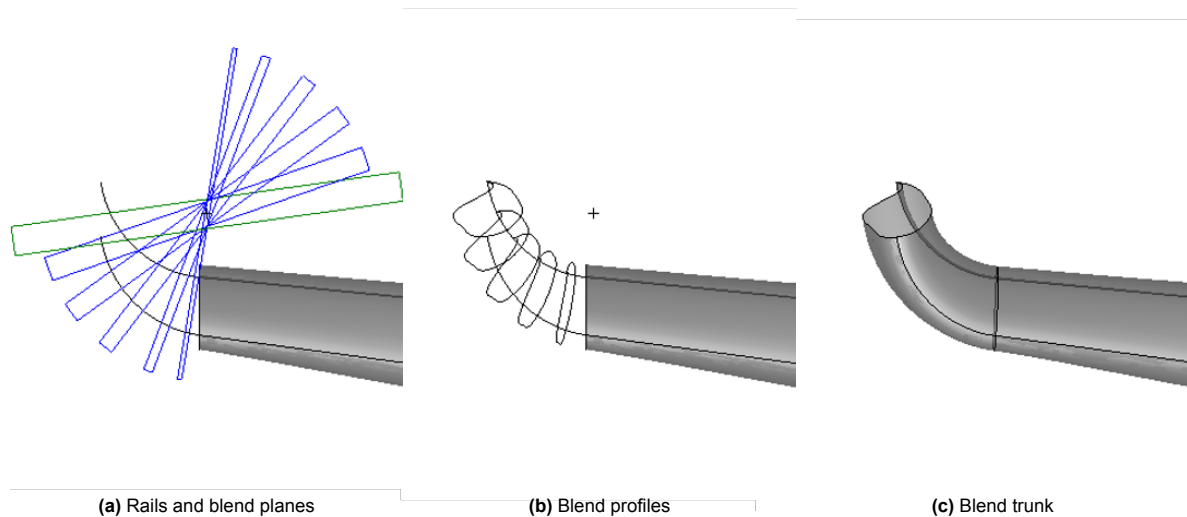


Figure 3.3: Blend trunk construction, front view

input for the instance of `WingShapeTrunk` that defines the winglet trunk. The winglet tip profile chord length is determined using the winglet taper ratio; the CST coefficients defining the airfoil curve shape again match those of the wing tip profile. The position of the winglet tip profile is determined using the winglet length, leading edge sweep angle, and the tip twist angle. The location of the tip profile is defined relative to the winglet root profile, translated from the root profile location the length of the winglet in the x-y plane of the local (airfoil) reference frame at an angle from the local y-axis equal to the winglet leading edge sweep. The winglet root airfoil reference frame is visualized in Figure 3.6. V_x , V_y , and V_z represent the x, y, and z axes, respectively, of the local reference frame used to position the winglet tip profile. The orientation of the tip profile is defined as the orientation of the winglet root profile rotated about its y-axis by the winglet tip twist angle. In the current study, the winglet tip profile orientation is equal to the winglet root profile orientation, as the winglet tip twist angle is equal to 0° . The root and tip profiles together fully define the winglet trunk.

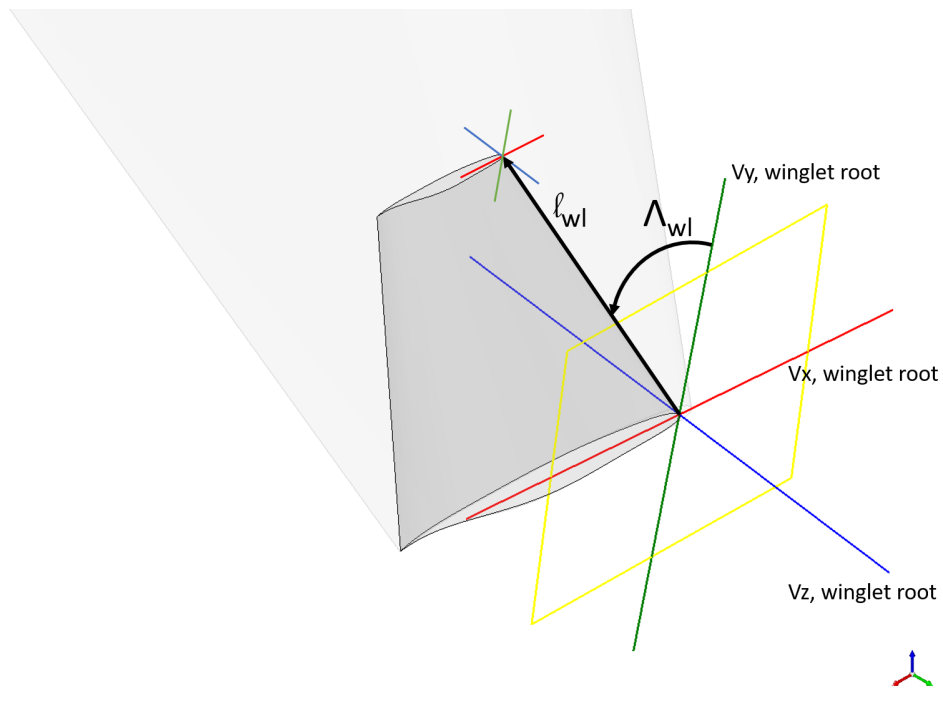


Figure 3.4: Isometric view of winglet trunk construction

As a final step, the total length of the wing and winglet together is measured. The wing span is kept constant at 64.6 m throughout the design exploration in order to ensure comparability between winglet designs. To keep the span constant, the span of the most outboard wing trunk is reduced such that the span of the full wing measured from the winglet tips is 64.6 m; the chord length and the airfoil shape of the wing tip profile is maintained. It should be noted that the leading edge sweep of the outboard wing is maintained when reducing the span. The area of the outboard wing is reduced in this process; the sweep angle of the trailing edge rail of the outboard wing will also change in this process.

A Unified Modeling Language (UML) Class diagram of the Flying-V ParaPy model, adapted from [18] to include the addition of the winglet in the model, is presented in Appendix A.

3.2. Design exploration and performance analysis

A full aerodynamic design optimization of the outboard wing and winglet is outside the scope of the current study. Instead, a design space exploration to decipher trends in key performance metrics was carried out. The approach to the current study and its implementation are discussed in the following sections.

3.2.1. Approach

The objective of the current study – to determine how the geometry of the winglets affect the lateral-directional stability and control characteristics of the Flying-V – is a driving factor in determining the method of performing the analysis. The ability to compute and analyze lateral-directional stability derivatives is therefore an important element to consider when selecting a suitable solver to analyze winglet geometries.

Potential flow methods are widely used in aircraft design tasks due to their computational speed and relative simplicity. A vortex lattice method (VLM), which represents wings and bodies by infinitely thin panels with camber, twist, and dihedral, is often satisfactory when analyzing conventional configurations. However, when thickness effects become more prominent, as is often the case with an unconventional configuration, it is desirable to more accurately represent the geometry of the aircraft using a three-dimensional potential flow surface model [20]. The 3D panel method selected for the analysis is FlightStream, a surface-vorticity solver developed by Research in Flight. The program is capable of analyzing both structured and unstructured surface meshes, which can be imported directly or generated and modified using built-in meshing tools. FlightStream performs an inviscid analysis of the flow field, along with a separate skin friction prediction based on the surface vorticity. Results obtained using FlightStream found in literature compare favorably to both experimental wind tunnel data and other CFD analyses, with improved results over a vortex lattice model tested [20–23].

Although FlightStream boasts relatively short computation times compared to other solvers, a full analysis of a single geometric configuration, including solver computation time, aerodynamic data extraction, and post-processing, takes one to two hours to complete. As such, in the interest of limiting computation time, a surrogate model is constructed to visualize trends and make predictions based upon the analyses of a limited sample of geometric configurations. A Kriging approximation model is selected as the surrogate for a full aerodynamic analysis using FlightStream. In order to achieve a uniform level of model accuracy throughout the design space, and to limit the statistical uncertainty of the computed approximation, a space-filling Latin Hypercube sampling plan is chosen to select a uniform, randomized spread of points [24]. Considering the five-dimensional design space, an initial sample of 50 winglet geometries is generated, adhering to the $n = 10d$ rule discussed in literature [25, 26]. Each of the 50 geometries in the sample are shown in Appendix B.

Each of the 50 geometries are analyzed in FlightStream at simulated approach conditions: sea-level standard, at Mach number $M = 0.2$ and total lift coefficient $C_L = 0.80$. Angle of attack (α) and sideslip angle (β) sweeps generate aerodynamic data that is used to calculate the lateral-directional stability and control derivatives of interest, namely $C_{y\beta}$, $C_{l\beta}$, and $C_{n\beta}$. Data on the aerodynamic efficiency of each geometry is also collected. Additional handling and control quality metrics, including the lateral control departure parameter (LCDP) and estimates of rudder control capacity, will be calculated using empirical formulas and data from previous work at Airbus [4]. The above characteristics will be used to train the Kriging approximation model, using the MATLAB toolbox DACE.

Table 3.2: Quantities describing wing of FV-1000 model without winglets

Parameter	Symbol	Value	Unit
Wing area	S	927.11	[m ²]
Mean aerodynamic chord	\bar{c}	18.23	[m]
Span	b	64.60	[m]

3.2.2. Implementation

The implementation of the approach described above can be divided into two parts: the aerodynamic evaluation in FlightStream, and the subsequent analysis and model fitting of the data.

Aerodynamic solver

The input file used to generate the initial geometry of the Flying-V upon which the winglet is constructed contains the parameters defining the FV-1000 model of the aircraft. The wing area, mean aerodynamic chord, and wing span of this model without winglets are provided in Table 3.2. These values are used to calculate all aerodynamic coefficients in the subsequent aerodynamic analysis.

The 50 geometries generated, each having a different winglet geometry, are exported from the ParaPy framework as IGES files and then uploaded in FlightStream. Each IGES file contains the geometry of just the starboard wing; the geometry is mirrored about the global x-z plane at the wing root to produce the full geometry of the aircraft. The geometry is split further into separate bodies for the inboard wing trunks, the outboard wing trunks, and the winglets, in order to analyze the aerodynamic loads on these bodies individually. The meshing of the geometry is performed within the FlightStream GUI; the built-in FlightStream meshing algorithm is used to create an unstructured surface mesh of the geometry. The mesh density of the winglet bodies is notably higher than that of the remaining bodies of the model, as the winglet performance is the primary focus of the study. The trailing edges of the geometry are also marked, as these are required boundary conditions for the calculation of aerodynamic loads on the body. The solver settings are set to simulate the desired flow conditions as described above, as well as the convergence threshold of 5.0×10^{-6} . Once these steps are complete, the solver is initialized and then run to convergence.

Once the solver has converged, the angle of attack is modified to match the specified lift coefficient of $C_L = 0.80$. The location of the neutral point, and the centre of gravity (CG) locations for static margins of 15% and 5% of the mean aerodynamic chord (MAC), are calculated iteratively using equation 3.1. The reference point X_{ref} for each centre of gravity (CG) position is calculated by defining local coordinate systems in FlightStream. These local coordinate systems are positioned with respect to the global reference coordinate system, as shown in Figure 3.5. The global reference coordinate system in FlightStream is located at the nose of the aircraft, as is the case in the ParaPy model; the axes are also oriented the same as the global reference frame in ParaPy. The axes of the local coordinate systems are oriented using the convention of stability and control coordinate systems for the proper calculation of the loads and moments on the aircraft. Each configuration is first analyzed with respect to the $X_{c/4}$ local reference frame, which is positioned 27.71 m from the global reference coordinate system in the global positive x-direction. This reference point is positioned at the quarter chord point of the mean aerodynamic chord of the baseline aircraft. Equation 3.1 is rearranged to form equation 3.2, which is used to calculate the next reference point at which C_{m_α} and C_{L_α} are again calculated in FlightStream to determine the following point. This process is repeated until the static margin at X_{ref} reaches the target value $K_{n,target}$ (0 for the neutral point, 0.15 for a 15% static margin, etc.). The CG locations at 15% and 2.5% static margins represent the forward and aft limits of the CG range for the geometry, and are the reference locations about which the lateral-directional coefficients are calculated.

$$K_n = \frac{X_{NP}}{\bar{c}} - \frac{X_{ref}}{\bar{c}} = -\frac{C_{m_\alpha}}{C_{L_\alpha}} \quad (3.1)$$

$$X_{next} = \left(-\frac{C_{m_\alpha}}{C_{L_\alpha}} - K_{n,target} + \frac{X_{ref}}{\bar{c}} \right) \bar{c} \quad (3.2)$$

The Solver Sweeper toolbox in FlightStream is then used to generate a sweep of results for varying

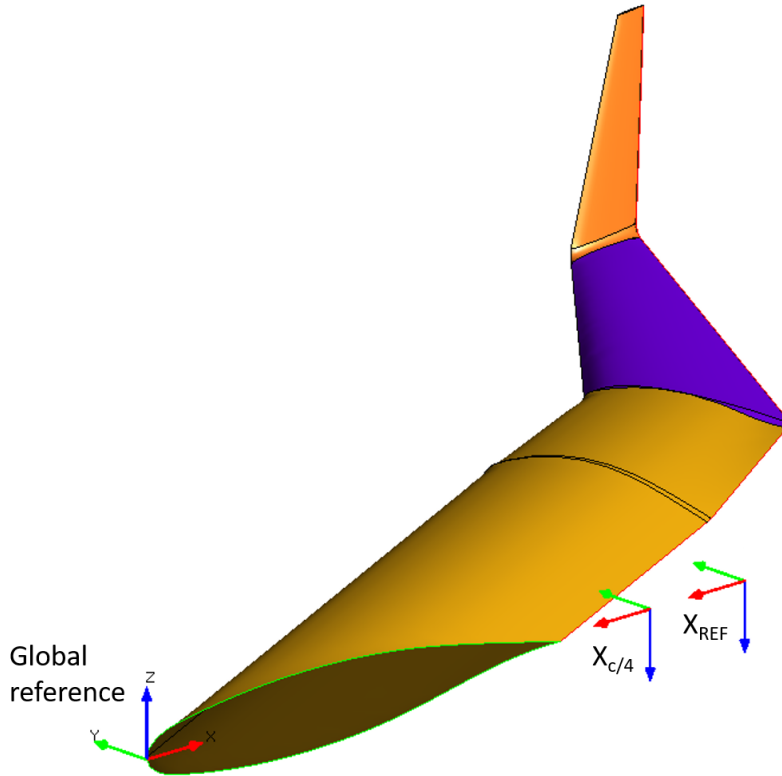


Figure 3.5: Positioning of global and local reference coordinate systems in FlightStream

sideslip angles, between $\beta = -5^\circ$ and $\beta = 5^\circ$ in steps of 1° , for the 15% and 5% static margin CG locations. The sweep returns the aerodynamic loads both on the whole body and on each of the split bodies representing the inboard wing, outboard wing, and winglets. This data is then processed and used in the subsequent post-aerodynamic analysis.

Analysis and model fitting

The aerodynamic data collected is parsed and the aerodynamic coefficients are extracted. The sideslip angle sweep data is collected, and the lateral-directional coefficients C_y , C_l , and C_n are plotted against the sideslip angle to fit a linear trend to each curve. The resulting slopes of these lines are recorded as the lateral-directional derivatives $C_{y\beta}$, $C_{l\beta}$, and $C_{n\beta}$ corresponding to each geometric configuration.

As mentioned in the previous section, additional lateral-directional handling quality and control capability metrics are calculated to more fully understand how each geometric configuration will affect performance. The first metric is the lateral control departure parameter (LCDP), a parameter which is often used to predict departure susceptibility. The LCDP is calculated as shown in equation 3.3. Its value should be positive; negative values usually correspond to roll reversal conditions [27].

$$LCDP = C_{n\beta} - C_{l\beta} \frac{C_{n\delta a}}{C_{l\delta a}} \quad (3.3)$$

An attempt is also made to estimate the yaw control capabilities of a rudder-incorporated winglet on the Flying-V. Although the modeling of the control surface on the winglet is outside the scope of the current study, the empirical formulas in equations 3.4 and 3.5 [28] are used to estimate the yawing moment due to rudder deflection, $C_{n\delta_r}$. These formulas use the vertical tail volume ratio, tail efficiency factor, lift curve slope, and a flap effectiveness factor to estimate the derivative.

$$C_{n_{\delta_r}} = -\eta_v V_v \frac{\partial C_{L_v}}{\partial \delta_r} \quad (3.4)$$

$$\frac{\partial C_{L_v}}{\partial \delta_r} = \frac{\partial C_{L_v}}{\partial \alpha_v} \frac{\partial \alpha_v}{\partial \delta_r} = C_{L_{\alpha_v}} \tau \quad (3.5)$$

With the lift and drag data, lateral-directional derivatives, and additional handling quality and control capacity metrics calculated and tabulated, the focus then shifts to constructing a surrogate model in the form of a Kriging approximation model. The model is constructed using the software package DACE (Design and Analysis of Computer Experiments) [29], a MATLAB toolbox built specifically for working with Kriging approximation models of computer experiments. The `dacefit` function computes the DACE model to a set of design data with specified regression and correlation models. Design data in this context refers to an $m \times n$ array of design sites with each of the m rows containing the n design variables for that site, as well as the $m \times q$ array of responses at each design site. The DACE toolbox offers three regression models: zero order polynomial, first order polynomial, and second order polynomial. It offers six correlation models, including linear, Gaussian, and cubic spline, as well as the ability to define a new correlation model. Once the DACE model is constructed, the `predictor` function uses the model to predict the function value, or responses, at a set of trial sites. This function can also be used to visualize trends in responses for varying design variables.

When fitting the Kriging approximation (DACE) model to a set of observed responses, a vector θ , comprised of elements θ_j corresponding to dimensions of the design space x_j , is optimized. The values θ_j affect the correlation between points in the design space. Assuming a Gaussian process, the optimization problem corresponds to maximum likelihood estimation of the observed responses [29]. These θ_j 's are sometimes referred to as 'activity parameters,' and can be used to estimate the order of importance of variables when considering their influence on the output of interest. Low θ_j indicates that points have a higher correlation, meaning that varying x_j has a smaller effect on the output $y(x_j)$. Conversely, high θ_j suggests much more variation in $y(x_j)$ for different values of x_j . Note that the values θ do not provide information on the interactions between parameters [24].

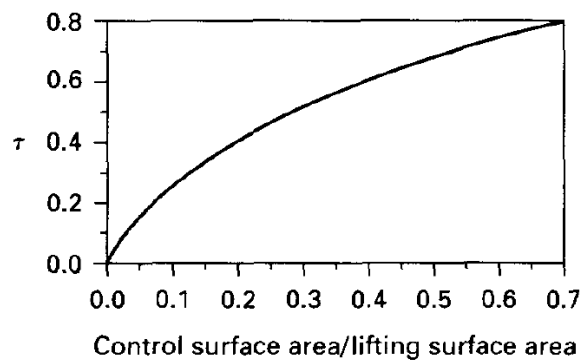
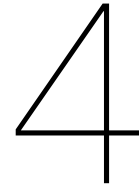


Figure 3.6: Flap effectiveness parameter ¹

¹Image from R. Nelson, *Flight Stability and Automatic Control*, 1998 [28]



Validation

The following sections outline validation exercises performed on the various components of the current research task. A mesh sensitivity study in FlightStream is performed, and output data from the aerodynamic solver is validated against wind tunnel data and previous research on the Flying-V. The Kriging approximation model is also validated against observed data.

4.1. Surface mesh sensitivity study

Unlike pressure solvers, which require highly refined surface meshes in regions of higher curvature in order to accurately capture pressure gradients, vorticity solvers are not limited in their fidelity by an appropriately refined mesh based on local surface curvature [30]. Effective solutions can be obtained even from surface meshes with sharply varying facet size gradients along the geometry surface. Vorticity solvers are also much less sensitive to local bumps in the surface mesh; the method of integrated circulation, which converts the arbitrarily oriented surface vorticity into directed circulation distributions for evaluation of aerodynamic loads on the body, smooths out the effects of topological perturbations [22].

Even given the above information, a surface mesh sensitivity study is performed to measure the effect of changes to the surface mesh on the calculated loads in FlightStream. The study is performed on the Flying-V geometry without winglets, at the optimization point used in the analyses of Faggiano [3] and Cappuyns [4]: fluid properties are set to simulate air at 13 000 m, the freestream velocity is set for a Mach number of 0.85, and the angle of attack is set to 2.5°. The results of the sensitivity study are

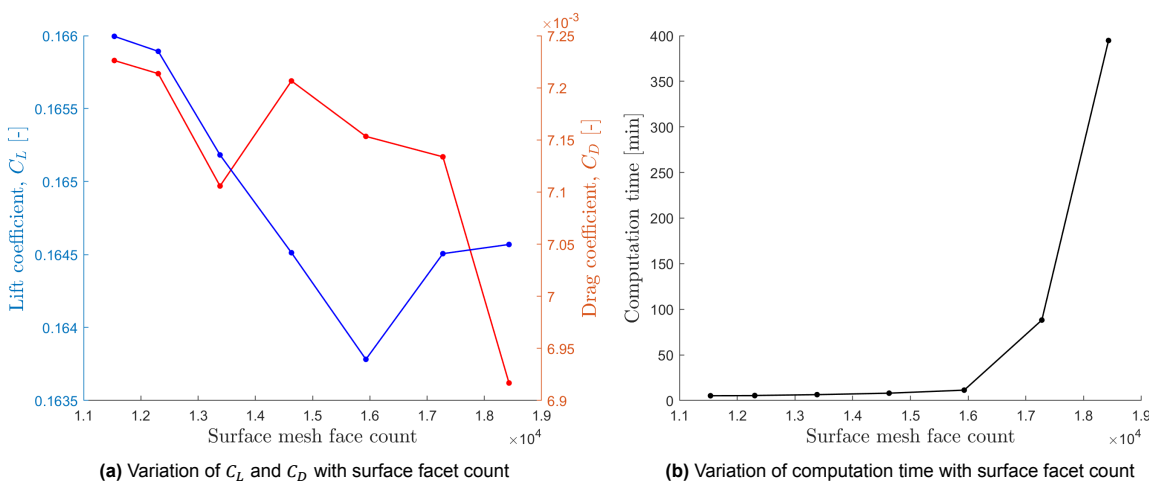


Figure 4.1: Surface mesh sensitivity study results

show in Figure 4.1. As Figure 4.1a suggests, there is no obvious trend in the variation of lift coefficient or drag coefficient as the mesh is refined and the number of facets increases. This is in contrast with what one might expect when refining a surface mesh intended to be used with a pressure-solver, where mesh refinement will continually improve the solution. Note also that the surface mesh face count has a limited effect on the calculated lift and drag coefficients in FlightStream: the standard deviation of the set of lift coefficients calculated is 7.32×10^{-4} , and the standard deviation of the set of drag coefficients calculated is 1.15×10^{-4} . The total range of the measured drag coefficients is just slightly over 3 drag counts.

Figure 4.1b illustrates how the computation time increases with increasing surface mesh face count. Below a face count of approximately 16 000, the computation time is proportional to the square of the number of facets. Due to computational limitations of the machine on which the solver software is used (HP Spectre x360 laptop, Intel(R) Core(TM) processor, i7-1065G7 CPU @ 1.30GHz, 16GB RAM), the computation time increases substantially above a total face count of 16 000.

As the surface mesh is seen to have a limited effect on the the calculated loads in FlightStream, the decision was made to limit the facet count to 16 000 in subsequent analyses in the interest of reduced computational time. An effort is made to keep the surface mesh as consistent as possible between the geometric configurations tested, with the same meshing technique and mesh sizing employed for each section of the wing across all configurations. It should be noted, however, that variations in surface mesh and facet count between configurations could have a nontrivial effect on the solver output.

4.2. FlightStream as aerodynamic solver

Although a number of studies using FlightStream as an aerodynamic solver have been published in journals and presented at various conferences [20–23], validation exercises were still performed on the tool. This process allowed for the validation not only of the aerodynamic data outputted by FlightStream but also the methodology employed to collect the data.

4.2.1. Validation using NACA wind tunnel data

Data from a National Advisory Committee for Aeronautics (NACA) study [31] is used to validate FlightStream lift and drag data. The study reports the lift, drag, and pitching moment characteristics of two large-scale semispan wing-fuselage models. The data was collected using both a wind tunnel six-component balance system and static-pressure orifices distributed along the upper and lower wing surfaces. Each wing-fuselage model had the following characteristics in common: 45° of sweepback, an aspect ratio of 6, a taper ratio of 0.5, and 10% thick sections normal to the quarter-chord line. One wing model, hereafter referred to as the plain wing, had no camber or twist; the other wing model, hereafter referred to as the cambered wing, was cambered and twisted for approximately elliptic loading at $C_L = 0.4$. The analyses were conducted at a Reynolds number of 8×10^6 based on the mean aerodynamic chord of 6.21 feet and a Mach number of 0.2.

Both wing-fuselage geometries are replicated in ParaPy for analysis. A surface mesh for each model is produced in FlightStream using the same method described in Chapter 3. The Solver Sweeper toolbox is used to generate a sweep of results for varying angles of attack, between $\alpha = 0^\circ$ and $\alpha = 24^\circ$ for the plain wing, and $\alpha = -3^\circ$ and $\alpha = 24^\circ$ for the cambered wing. The lift and drag data collected in FlightStream is compared to the NACA wind tunnel data for the plain wing in Figure 4.2 and for the cambered wing in Figure 4.3; the data for the plain wing will be shown in the full thesis. Note that the dashed lines in the figure represent the angle of attack and lift coefficient thresholds at which the onset of flow separation at the wing tip was detected during wind tunnel testing. For the plain wing, the flow remained attached up until an angle of attack of approximately 11.5° , corresponding to $C_L = 0.65$. For the cambered wing, the flow was attached for the angle of attack range from 1° to approximately 12° , corresponding to $C_L = 0.09$ and $C_L = 0.72$, respectively.

Figures 4.2a and 4.3a show that the FlightStream model underpredicts the drag coefficient C_D for both the plain and cambered wings. For the ranges of angles of attack in which the flow is attached, the percent error averages 16.9% and 8.3% for the plain wing and cambered wing, respectively. Despite the underprediction, the FlightStream model appears to capture the behaviour of the C_L vs C_D curves well. Figures 4.2b and 4.3b shows the resulting C_L/C_D curves calculating using the lift and drag data. The FlightStream error in maximum lift-to-drag ratio prediction is 22.4% and 11.5% for the plain wing

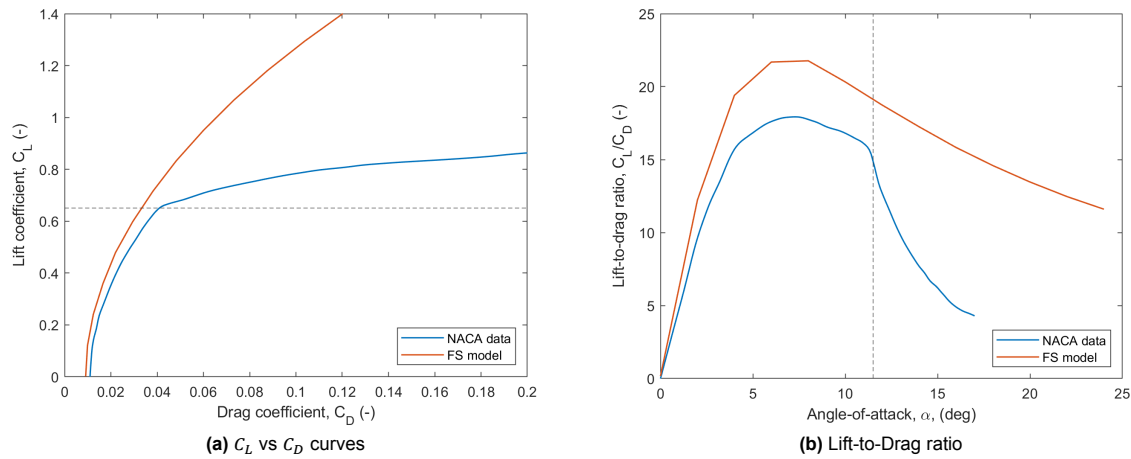


Figure 4.2: Plain wing: NACA wind tunnel data compared to FlightStream data

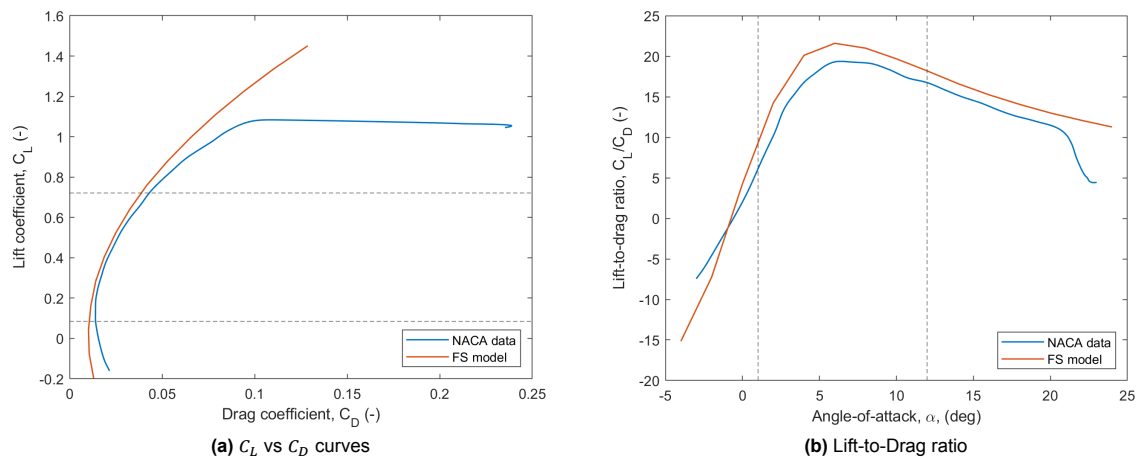


Figure 4.3: Cambered, twisted wing: NACA wind tunnel data compared to FlightStream data

and cambered wing, respectively.

A number of different aspects may contribute to the discrepancy between FlightStream and the NACA wind tunnel data in the calculation of lift and drag. Though the dimensions of each wing were given in [31], construction of the CAD wing-fuselage geometries in ParaPy may differ from the physical models built for the wind tunnel. The absence of tunnel-wall effects in the FlightStream model may also skew the output data, as the tunnel wall is not modeled in this analysis. Additionally, the use of vorticity models for computing lift and drag forces, with flow separation modeling disabled, indicates that the modeled flow in FlightStream is strictly linear for lift and induced drag forces and moments. Any nonlinear flow effects, including the formation of laminar separation bubbles, are not captured in the FlightStream model.

4.2.2. Comparison to previous analyses of Flying-V

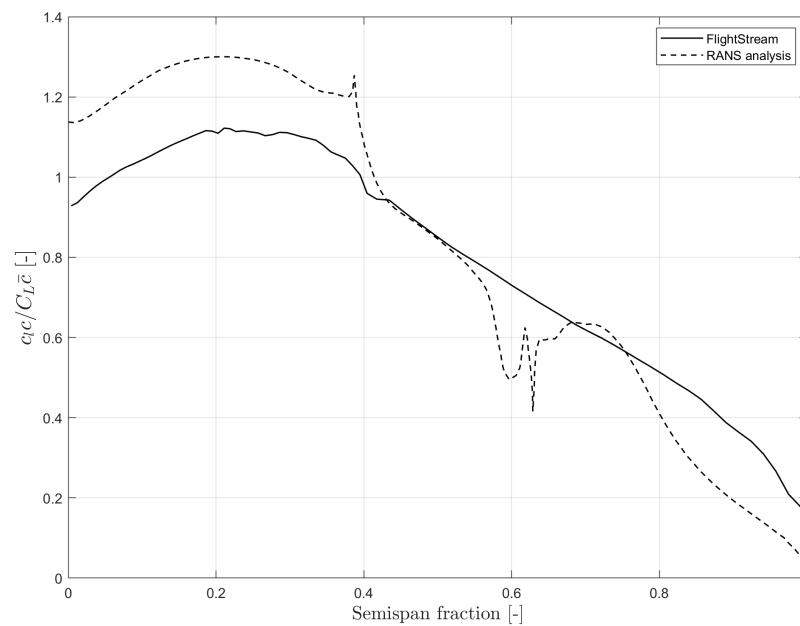
In order to ensure comparability to and build off of past research done on the Flying-V, an analysis of the Flying-V geometry at conditions previously tested is performed in FlightStream. The analysis is performed at the same optimization point used in the analyses of Faggiano [3] and Cappuyns [4]. Fluid properties are set to simulate air at 13 000 m, the freestream velocity is set to simulate a Mach number of 0.85, and the angle of attack is set to 2.5°. The geometric configuration analyzed in FlightStream is the Flying-V without winglets; the input variables are set such that the geometry is comparable to Faggiano's optimized Flying-V geometry. A comparison of the aerodynamic efficiency (lift-to-drag ra-

Table 4.1: Comparison of Flying-V aerodynamic efficiency at $M = 0.85$, $\alpha = 2.5^\circ$

Analysis	C_L/C_D
Faggiano [3]	23.7
Cappuyns [4]	23.9
FlightStream	23.8

ratio, C_L/C_D) of the Flying-V calculated in FlightStream to those calculated by Faggiano and Cappuyns is shown in Table 4.1. As evidenced in the table, the calculated aerodynamic efficiency closely matches those found in previous analyses. It should be noted, however, that the lift and drag coefficients calculated in FlightStream are both smaller than those calculated in the analyses of Faggiano and Cappuyns. In FlightStream, the calculated lift coefficient is $C_L = 0.165$ and the calculated drag coefficient is $C_D = 0.0069$, compared to $C_L = 0.26$ and $C_D = 0.0111$ from the analysis of Faggiano.

An attempt was also made to compare the lift distribution from the Flying-V model without winglets in FlightStream to one from a Reynolds-averaged Navier-Stokes (RANS) CFD analysis performed by M. Palermo [32]. In FlightStream, this analysis is performed at simulated approach conditions: at sea-level standard, a Mach number of 0.2, and lift coefficient $C_L = 0.80$. The RANS CFD analysis is performed using the commercial software Ansys Workbench 19.1. Air density and viscosity were set to match data registered from instruments in the concurrent wind tunnel testing, and the Mach number was set to 0.06. The resulting normalized lift distributions $c_l c / C_L \bar{c}$ are plotted in Figure 4.4. As the figures suggest, the spanwise lift distribution calculated in FlightStream closely matches that from the full RANS CFD analysis performed by Palermo. Although FlightStream may not capture the effects of leading-edge vortical structures that are visible from the full RANS analysis, the shape of the normalized lift curve, including the spanwise location of the peak, are quite comparable.

**Figure 4.4:** Comparison of spanwise lift distributions from FlightStream and a RANS analysis

4.3. Kriging approximation model

The initial space-filling Latin Hypercube sampling plan of 50 geometric configurations was to be used entirely to build the Kriging approximation model, and five to ten additional randomly generated samples were to be collected in order to validate and test the model. However, in the time between the analysis

of the 50 geometric configurations and the planned analysis of the model validation geometries, the FlightStream software and TU Delft licenses were updated from FlightStream 2020.1 to FlightStream 2020.2. The software update altered a number of available settings and functions in FlightStream, including the built-in unstructured meshing algorithm. This rendered the analysis of the additional geometries in the updated FlightStream software impossible, as the exact testing settings and conditions could not be replicated.

In an effort to validate the Kriging model with the data already collected from the initial pool of samples, three samples were selected at random and set aside to be used to test the model. The three randomly selected samples were 9, 20, and 33. The remaining 47 samples were used to construct the Kriging surrogate model. Note that the initial samples were chosen to be space-filling, i.e., uniformly spread throughout the design space in order to ensure uniformity of model accuracy throughout the design space. Removing any number of samples from the 50 generated will therefore be to the detriment of the uniformity ('space-fillingness') of the sampling plan, and may reduce the model's accuracy. Using a smaller set of data points to build the model will also reduce its accuracy at a global level.

With the observed data split into a model-building set and a test set, the accuracy of the model could be tested. The metric selected to measure model accuracy is the root mean squared error (RMSE), which is calculated as shown in equation 4.1. Note that the small size of the test set relative to the model-building set will affect how well the accuracy of the model can be measured.

$$\text{RMSE} = \sqrt{\frac{\sum_{i=0}^{n_t} (y^{(i)} - \hat{y}^{(i)})^2}{n_t}} \quad (4.1)$$

The RMSE is normalized by dividing by the range of the responses of the set of samples used to construct the model. The normalized RMSE is an indicator how good the model is in predicting the response of a new sample or set of samples outside of the observed set of data. A RMSE under 10 % of the range of observed responses implies a reasonable global model; RMSE under 2 % implies a very good model [24].

As mentioned in the previous chapter, the MATLAB toolbox DACE is used to construct the Kriging approximation model. The regression and correlation models selected affect the model fitted to the observed data. DACE offers three regression models with polynomials of orders 0, 1, and 2. A higher order regression model generally increases model approximation accuracy, though the possibility of overfitting any noise or error that could mask responses in the data also increases with increasing model order [24]. The correlation models offered are: linear, exponential, Gaussian, spherical, and cubic spline. The selection of correlation model should be driven by the process to be modeled. If the process is a continuously differentiable phenomenon to be optimized, a correlation model showing parabolic behaviour near the origin should be selected; these include the Gaussian and cubic spline functions. If the process exhibits more linear behaviour near the origin, such as many physical phenomena, a correlation model with linear behaviour near the origin would usually perform better; these include the linear, exponential, and spherical functions [29].

A sensitivity study is performed to analyze the effect of choice of regression and correlation models on the accuracy of the predictions from the approximation models, measured as the RMSE of the predictions at the set of test data sites. The results are shown in Table 4.2. Notably, many of the RMSE values fall within the 10 % threshold for a reasonably good global model, and some even fall within or approach the 2 % threshold for a very good model. Another interesting observation is that RMSE generally decreases with increasing polynomial order, but not in every case. This may be attributed to overfitting as discussed above. However, in nearly every case, the second order polynomial regression model offers the smallest prediction error of the three. Additionally, the correlation model is seen to have a relatively limited influence on RMSE for many of the outputs analyzed, particularly for the second order polynomial regression model. This contradicts an earlier remark about the importance of selecting an appropriate correlation model for the specific process to be modeled. This observation may be attributed to a data saturation of the surrogate model, i.e., the number of data points is approaching a limit at which any further additions would not improve global model accuracy [24].

Given the data from Table 4.2 and the above observations, as well as information in literature about choosing the proper correlation model, a second order polynomial regression model and linear correlation model are selected for Kriging approximation model which will be discussed and analyzed in the

following chapter.

Table 4.2: RMSE values corresponding to the different correlation and regression models for each output

Correlation model	Polynomial order	Normalized RMSE					
		C_{y_β}	C_{l_β}	C_{n_β}	C_L/C_D	LCDP	$C_{n_{\delta_r}}$
Linear	Zero	0.1546	0.2808	0.0910	0.1378	0.0870	0.0283
	First	0.1231	0.0974	0.1779	0.0848	0.1220	0.0405
	Second	0.0174	0.0616	0.0359	0.0316	0.0485	0.0227
Exponential	Zero	0.0164	0.1376	0.0582	0.0433	0.1106	0.0445
	First	0.1227	0.0938	0.1253	0.0620	0.1510	0.0519
	Second	0.0175	0.0622	0.0358	0.0316	0.0485	0.0236
Gaussian	Zero	0.0707	0.1175	0.0423	0.0786	0.0899	0.0317
	First	0.0992	0.0974	0.1779	0.0856	0.0713	0.0378
	Second	0.0129	0.0616	0.0360	0.0316	0.0485	0.0247
Spherical	Zero	0.1546	0.2808	0.0910	0.1378	0.0892	0.0221
	First	0.1231	0.0974	0.1779	0.0848	0.1437	0.0286
	Second	0.0174	0.0616	0.0359	0.0316	0.0485	0.0213
Cubic spline	Zero	0.1546	0.2808	0.0910	0.1378	0.0770	0.0353
	First	0.1231	0.0974	0.1779	0.0848	0.2006	0.0696
	Second	0.0174	0.0616	0.0359	0.0316	0.0485	0.0194

5

Results

The results from the aerodynamic analyses of the winglet geometries in FlightStream, as well as the global surrogate models constructed to generalize the results for the entire design space, are presented in the following sections. The raw aerodynamic data extracted from FlightStream can be found in Appendix C.

5.1. Winglet-off analysis of baseline aircraft

An analysis of the Flying-V model FV-1000 without winglets is first presented for comparison to the winglet-on cases presented in the following sections. The wing parameters of the FV-1000 model without winglets are presented in Table 5.1. These are the wing parameters used to calculate the aerodynamic coefficients for the baseline case, as well as every case in the following sections where the winglet parameters are investigated.

Table 5.1: Wing parameters of FV-1000 model without winglets used for aerodynamic coefficient calculation

Parameter	Symbol	Value	Unit
Wing area	S	927.11	[m ²]
Mean aerodynamic chord	\bar{c}	18.23	[m]
Span	b	64.60	[m]

The lateral stability coefficients for the baseline aircraft without winglets are presented in Table 5.2. These coefficients are calculated at a lift coefficient of $C_L = 0.80$, with reference point at a forward CG position (static margin of 15%), mach number $M = 0.2$, and standard sea level atmosphere. These flight conditions are replicated for all subsequent analysis in the following sections.

Table 5.2: Lateral-directional stability coefficients for baseline aircraft without winglets

Coefficient	Value	Unit
$C_{y\beta}$	-0.0297	rad ⁻¹
$C_{l\beta}$	-0.2757	rad ⁻¹
$C_{n\beta}$	-0.0269	rad ⁻¹

As the values in Table 5.2 suggest, the aircraft exhibits directional instability, with $C_{n\beta} < 0$. The baseline aircraft is marginally stable when considering the side force due to sideslip. The dihedral effect, or rolling moment due to sideslip $C_{l\beta}$ shows strong lateral stability. The coefficients $C_{y\beta}$, $C_{l\beta}$, and $C_{n\beta}$ are discussed at length in sections 5.2, 5.3, and 5.4, respectively.

The aerodynamic efficiency of the baseline aircraft at the aforementioned flight conditions is calculated to be $C_L/C_D = 22.83$. The aerodynamic efficiency is discussed at length in section 5.5.

An analysis of the potential departure susceptibility of the baseline aircraft indicated that the calculated lateral control departure parameter for the configuration was equal to -0.00135 ; the value of $C_{n_{\beta_{\text{DYN}}}}$ was calculated to be 0.00158 . These quantities, how they are calculated, and their implications are discussed at length in section 5.6. The important takeaway from this analysis is that the baseline aircraft without winglets could exhibit mild initial yaw divergence, mild rolling departure, and low spin susceptibility.

5.2. Side force due to sideslip

The optimized parameters θ from the fitting of the Kriging DACE model to the set data collected in FlightStream are used to rank the design parameters on their influence on $C_{y_{\beta}}$ in Table 5.3. From the table, it appears that the winglet leading edge sweep angle is the most active parameter, followed by the winglet length and cant angle, and then the winglet taper ratio and wing taper ratio as the least active parameters. The wing taper ratio and winglet taper ratio have notably little influence on $C_{y_{\beta}}$, according to their optimal θ values.

Table 5.3: Ranking of parameters influencing $C_{y_{\beta}}$ based on activity parameter θ

Parameter	θ
Sweep	1.7027
Length	0.7430
Cant	0.6484
Wing taper	0.1746
Winglet taper	0.1161

The influence of the winglet length, cant angle, and sweep angle on $C_{y_{\beta}}$ based on the Kriging approximation model is shown in Figure 5.1. The figure shows the trends in $C_{y_{\beta}}$ for varying winglet lengths from 3 m to 12 m, at seven values of cant angle and four values of leading edge sweep angle. The winglet taper ratio is fixed at 0.65 and the wing taper ratio is fixed at 0.15. In almost every case, increasing the winglet length results in a more negative $C_{n_{\beta}}$. Lower cant angles generally also result in more negative $C_{n_{\beta}}$ values. The exceptions to these trends are found at a leading edge sweep angle

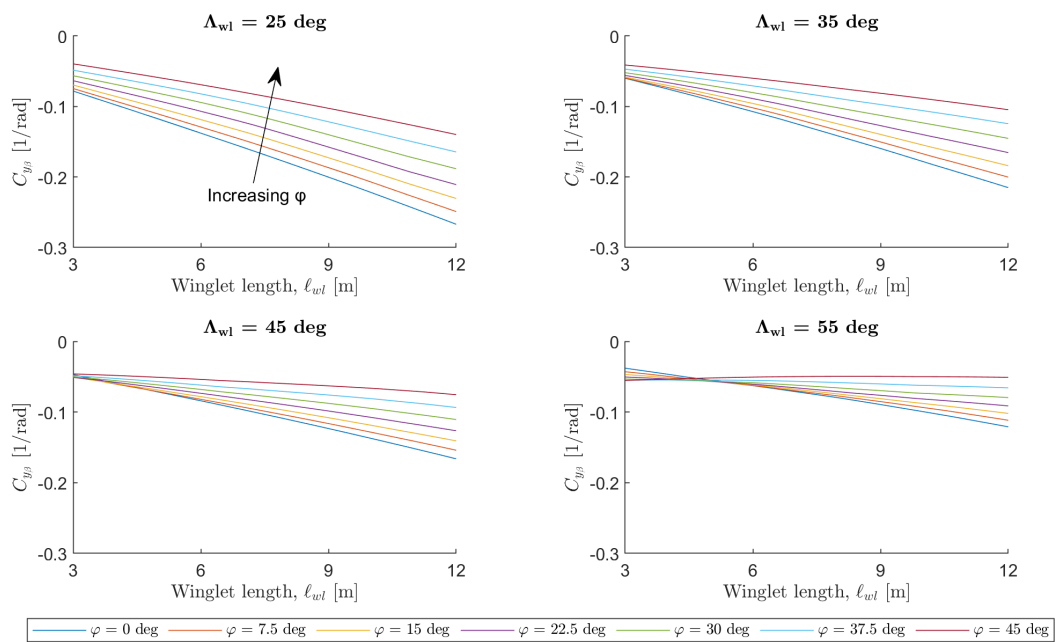


Figure 5.1: Influence of winglet length, cant angle, and leading-edge sweep angle on $C_{y_{\beta}}$ at forward/aft CG locations

of 55° and shorter winglet lengths, between approximately 3 m to 5 m. Increasing sweep angle has the effect of shifting the curves upward, such that the range of C_{y_β} values for each curve is decreased. This results in less negative values at higher winglet lengths.

The trends appearing in Figure 5.1 and discussed above appear logical for a wide range of winglet lengths, sweep angles, and cant angles. As the winglet length increases, the winglet side area increases across all combinations of cant and sweep angles; consequently, the side force generated by the winglets also increases, and C_{y_β} becomes more negative. Similarly, reducing the winglet cant angle (i.e., having a more vertical winglet) increases the side area. This is true across a majority of combinations of winglet length and sweep angles, the exception being at higher sweep angles and winglet lengths at the lower end of the tested range. In these exceptional cases, the side area first increases as the cant angle is reduced from the upper end of the tested range, up until an inflection point is reached, after which the side area begins to decrease as the cant angle is reduced further; this inflection point is reached at higher cant angles as the leading edge sweep angle of the winglet increases (around $\varphi = 7.5^\circ$ for $\Lambda_{wl} = 35^\circ$, around $\varphi = 22.5^\circ$ for $\Lambda_{wl} = 55^\circ$). This is a by-product of the chosen parametrization method for the winglet.

The trends seen in the graph for $\Lambda_{wl} = 55^\circ$, where a higher cant angle results in a more negative C_{y_β} for shorter winglet lengths, may be explained partially by the above mentioned geometric trends at high sweep angles and shorter winglet lengths. However, this reduction in side area may not capture the phenomenon entirely. The aerodynamic data extracted from FlightStream indicates that, as the winglet cant angle increases, the percentage of the total lift generated by the winglets increases. This is particularly true for winglets with higher leading edge sweep angles. Concurrently, as the cant angle increases, the outboard wing area decreases due to the span correction built in to the winglet parametrization; this results in a decrease in lift produced at the outboard wing sections. Although the forces produced by a winglet with higher cant may not be directed primarily in the body-fixed y-axis, the component of the force in the body-fixed y-axis may still be higher than for a more vertical winglet with reduced aerodynamic loading. This results in a slightly more negative value of C_{y_β} for a shorter winglet with high sweep and higher cant angle. This is seen only for winglets at the lower end of the tested range of winglet lengths (up until approximately $\ell_{wl} = 5$ m); above this threshold, the increased side area of winglets with lower cant angles has a dominant effect on the side force produced, and a lower cant angle will always result in a more negative value of C_{y_β} .

The influence of the winglet taper ratio on C_{y_β} based on the Kriging approximation model is shown

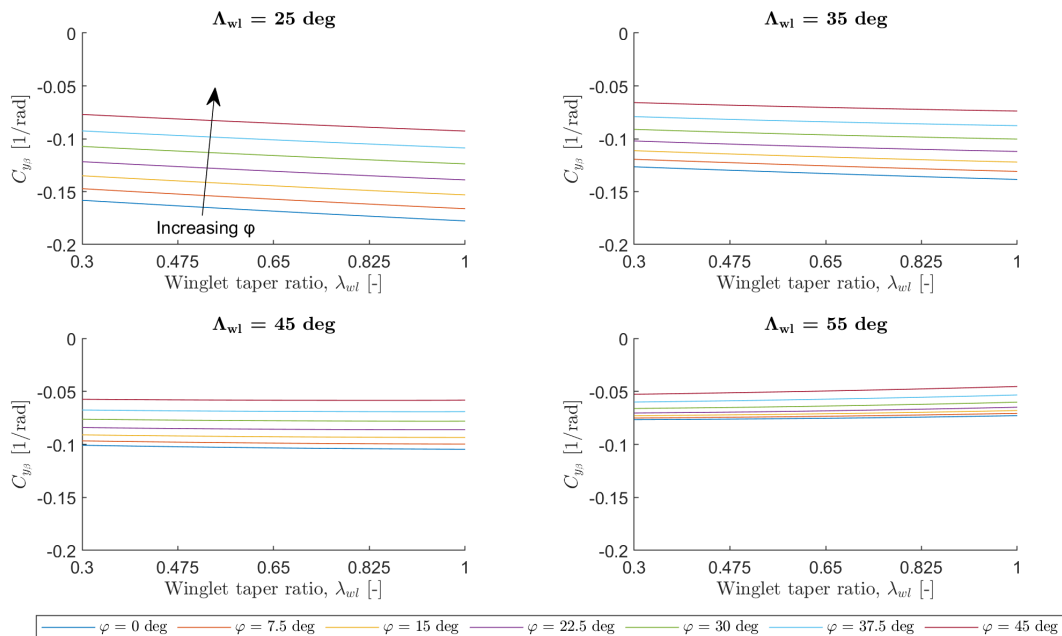


Figure 5.2: Influence of winglet taper ratio on C_{y_β} at forward/aft CG locations

in Figure 5.2. The winglet length is fixed at 7.5 m and the wing taper ratio is fixed at 0.15. As expected from the activity parameter analysis, the winglet taper ratio has a limited effect. Increasing winglet taper ratio results in a slightly more negative $C_{y\beta}$ across the range of cant angles for lower sweep angles; the trend is flat or slightly increasing for higher sweep angles.

The trends seen in Figure 5.2 generally align with what would be expected. With the winglet length fixed at 7.5 m, it can be seen clearly that increasing the cant angle results in a less negative value of $C_{y\beta}$ as the side area of the winglet is reduced. This is more pronounced at lower sweep angles, which is a by-product of the chosen parametrization method of the winglet. For a majority of the range of tested winglet leading edge sweep angles, an increase in winglet taper ratio results in a less negative value of $C_{y\beta}$ due to the increased side area of the winglet. The only exceptions to this trend are at the upper end of the range of sweep angles tested, where increasing the winglet taper ratio has a marginal effect on $C_{y\beta}$. This is likely a result of the parametrization method chosen, or may also be a result of systematic error or noise in the data due to small changes in computational mesh between test cases.. Nevertheless, the effect of the winglet taper ratio on $C_{y\beta}$ is so marginal compared to the other design variables that it may be considered negligible.

The influence of the wing taper ratio on $C_{y\beta}$ based on the Kriging approximation model is shown in Figure 5.3. The winglet length is fixed at 7.5 m and the winglet taper ratio is fixed at 0.65. As expected from the activity parameter analysis, the wing taper ratio also has a limited effect. At lower sweep angles, increasing wing taper ratio results in a slightly more negative $C_{y\beta}$ for all cant angles. At higher sweep angles, the trend remains decreasing for most cant angles, with the exception of the 37.5° and 45° lines, which show a flat or slightly increasing trend.

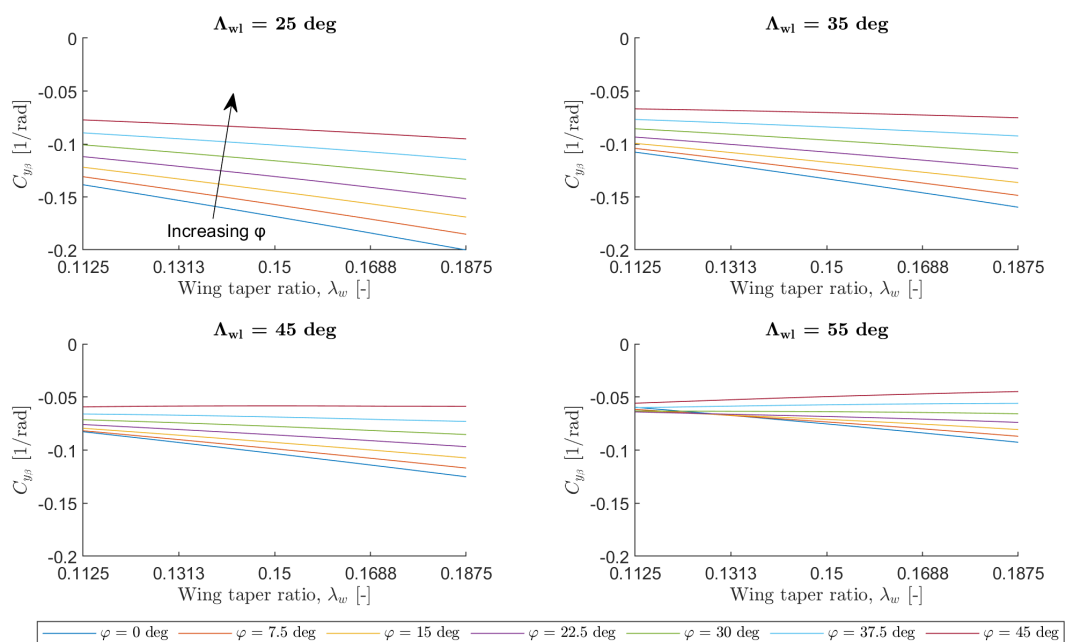


Figure 5.3: Influence of wing taper ratio on $C_{y\beta}$ at forward/aft CG locations

The trends in Figure 5.3 align with the trends seen in Figure 5.2 and described above. Increasing the wing taper, while keeping the winglet taper ratio constant, still has the effect of increasing the winglet side area, as the winglet root chord will increase as the wing taper ratio increases. Consequently, the value of $C_{y\beta}$ decreases. This trend is more pronounced at lower sweep angles as a result of the chosen parametrization method. Nevertheless, like the effect of the winglet taper ratio, the effect of the wing taper ratio on $C_{y\beta}$ is so marginal compared to the other design variables that it may be considered negligible.

As a final note, the magnitude of the $C_{y\beta}$ values compared to a ‘target’ value from an analysis of existing handling quality data on representative contemporary transport aircraft [6, 7] is discussed. From Table 2.1, the average value of $C_{y\beta}$ observed is -0.80 with a sample standard deviation of 0.11.

To be within one standard deviation of the average observed, the target value for $C_{y\beta}$ is -0.69 . This indicates that even the lowest predicted value of $C_{y\beta} = -0.27$ from Figure 5.1, for a winglet of length $\ell_{wl} = 12$ m, cant angle $\varphi = 0^\circ$ and leading edge sweep angle $\Lambda_{wl} = 25^\circ$, does not fall even markedly close to the range of observed values. However, this result is to be expected, given the absence of a fuselage and large vertical tail surface on the Flying-V. The aircraft analyzed in the handling quality studies were all of the conventional ‘tube-and-wing’ configuration, meaning that they had both a large fuselage with side area aft of the CG and large vertical tail surface with large moment arm aft of the CG contributing to the significantly more negative side force derivative.

5.3. Rolling moment due to sideslip

The optimized parameters θ are used to rank the design parameters on their influence on $C_{l\beta}$ in Table 5.4. From the table, it appears that the winglet leading edge sweep angle is the most active parameter, followed by the winglet length and cant angle, and then the winglet taper ratio and wing taper ratio as the least active parameters.

Table 5.4: Ranking of parameters influencing $C_{l\beta}$ based on activity parameter θ

Parameter	θ
Sweep	1.8771
Length	0.8673
Cant	0.8553
Winglet taper	0.6001
Wing taper	0.5361

The influence of the winglet length, cant angle, and sweep angle on $C_{l\beta}$ based on the Kriging approximation model is shown in Figure 5.4. The figure shows the trends in $C_{l\beta}$ for varying winglet lengths from 3 m to 12 m, at seven values of cant angle and four values of leading edge sweep angle. The winglet taper ratio is fixed at 0.65 and the wing taper ratio is fixed at 0.15. Note that the average value of $C_{l\beta}$ from an analysis of existing handling quality data on representative contemporary transport aircraft is indicated in the figure by a dashed horizontal line. In all cases, increasing winglet length results in a

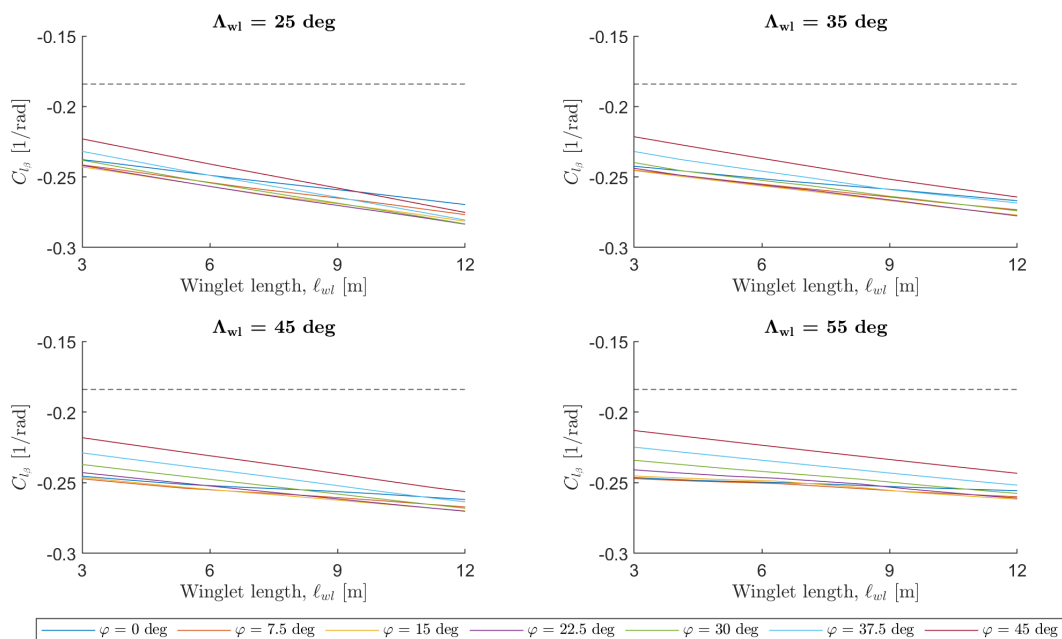


Figure 5.4: Influence of winglet length, cant angle, and leading-edge sweep angle on $C_{l\beta}$ at forward/aft CG locations

more negative value of $C_{l_{\beta}}$. Lower cant angles also generally result in a more negative $C_{l_{\beta}}$, though the spacing between lines for the lower cant angles is notably smaller than those for the higher cant angles. A closer look at the curves appears to indicate that the slope of the $C_{l_{\beta}}$ curves decrease with decreasing cant angle, such that increasing the length of the winglet has less influence on $C_{l_{\beta}}$ for a more vertical winglet. Increasing the sweep angle appears to marginally shift the curves upward, as well as reduce the slope of the curves, resulting in slightly less negative values of $C_{l_{\beta}}$ at the upper end of the range of winglet lengths.

The winglet-off analysis of the Flying-V showed that the value of $C_{l_{\beta}}$ in the winglet-off configuration is equal to -0.2757 . A majority of the combinations of winglet length, cant angle, and sweep angle show a $C_{l_{\beta}}$ value that is less negative than the winglet-off configuration. As discussed above, the addition of the winglets has the effect of reducing the span and area of the outboard wing, which results in a reduction of the dihedral effect for the Flying-V. However, given the observation from previous research on the Flying-V [4] that the aircraft exhibited excessive dihedral, a slight increase in $C_{l_{\beta}}$ from the addition of the winglets is likely not a great concern.

The trends appearing in Figure 5.4 and discussed above generally align with what would be expected. As discussed in Chapter 2, a parametric study on the effect of modifying winglet parameters on the lateral-directional stability derivatives of a generic wing [8] showed that increasing the winglet length and increasing outward cant angle of the winglet increases dihedral effect. The first of these observations is mirrored in the results of the current research: increasing the winglet length results in a more negative value of $C_{l_{\beta}}$. However, the trends in Figure 5.4 show less negative values of $C_{l_{\beta}}$ as the winglet cant angle. This is likely attributed to the span correction built into the the winglet parametrization. As the winglet cant angle increases, the span and area of the outboard wing decreases to correct for the increase in span from the outboard canted winglet. The wing of an aircraft has the greatest influence on the value of $C_{l_{\beta}}$; as such, reducing the span and area of the ‘planar’ section of the outboard wing with the addition of the winglet has the effect of reducing the dihedral effect, i.e., resulting in a less negative value of $C_{l_{\beta}}$. Additionally, from [8], moving the winglet aftward and increasing winglet sweepback was shown to reduce the increment in dihedral effect. This correlation is seen in the data and trends from Figure 5.4.

The influence of the winglet taper ratio on $C_{l_{\beta}}$ based on the Kriging approximation model is shown in Figure 5.5. The winglet length is fixed at 7.5 m and the wing taper ratio is fixed at 0.15. Note that the

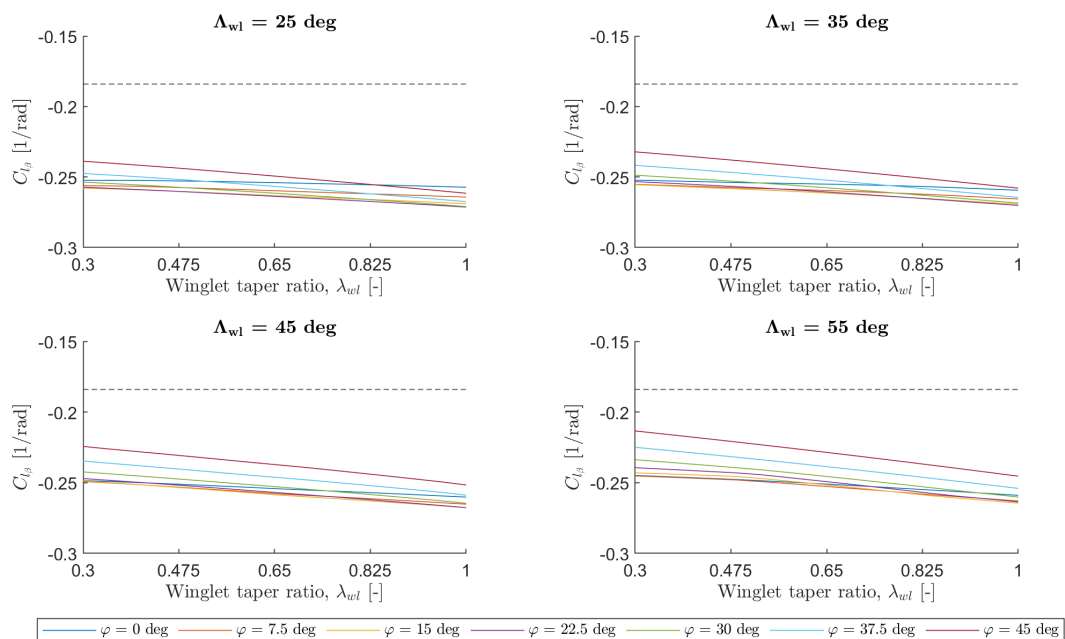


Figure 5.5: Influence of winglet taper ratio on $C_{l_{\beta}}$ at forward/aft CG locations

average value of C_{l_β} from an analysis of existing handling quality data on representative contemporary transport aircraft is indicated in the figure by a dashed horizontal line. The trends are decreasing for all cases, such that increasing the winglet taper ratio results in a more negative C_{l_β} .

The trends in Figure 5.5 appear logical across the range of sweep and cant angles. As the winglet taper ratio is increased, more lift is generated at the winglet due to increased area of the winglet trunk. This increase in lift produces a larger corrective rolling moment as the aircraft is subjected to sideslip, thus resulting in more negative values of C_{l_β} .

The influence of the wing taper ratio on C_{l_β} based on the Kriging approximation model is shown in Figure 5.6. The winglet length is fixed at 7.5 m and the winglet taper ratio is fixed at 0.65. Note that the average value of C_{l_β} from an analysis of existing handling quality data on representative contemporary transport aircraft is indicated in the figure by a dashed horizontal line. The trend shows that an increase in wing taper ratio generally results in a more negative C_{l_β} , the exceptions being for lower cant angles at lower sweep angles. The slope of each curve becomes more negative as the wing taper ratio increases, such that an increase or decrease in wing taper ratio at the upper end of the tested range has a greater effect on C_{l_β} .

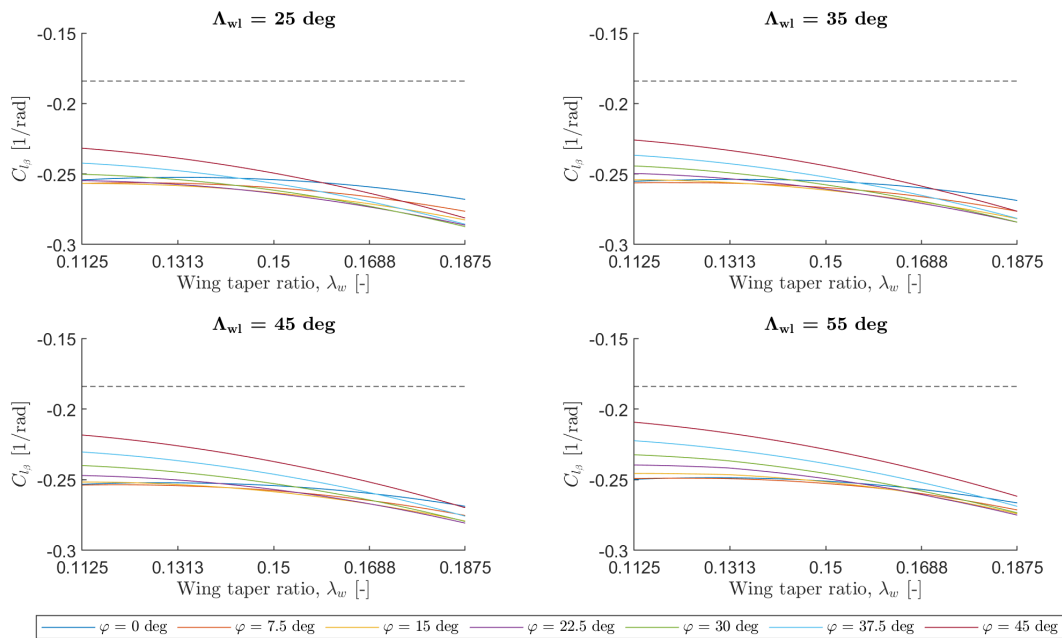


Figure 5.6: Influence of wing taper ratio on C_{l_β} at forward/aft CG locations

As discussed above, the wing of an aircraft has the most significant influence on the value of C_{l_β} . This is clearly seen in the trends shown in Figure 5.6. As the wing taper ratio increases, the value of C_{l_β} becomes more negative, as the outboard wing area increases and more lift is generated on the outboard wing sections.

As a final note, the magnitude of the C_{l_β} values compared to a ‘target’ value from an analysis of existing handling quality data on representative contemporary transport aircraft [6, 7] is discussed. From the trends in Figures 5.4 to 5.6, it is clear that the values of C_{l_β} lie below the average value of C_{l_β} observed for every combination of winglet length, cant angle, and sweep angle tested. From Table 2.1, this value is -0.18 with a sample standard deviation of 0.04 . To be within one standard deviation of the average observed, the target value for C_{l_β} is -0.22 . As stated in Chapter 2, the wing sweep angle has a significant influence on the value of C_{l_β} . Given the considerably high inboard sweep angle of 64.5° on the Flying-V, it is logical that the dihedral effect exceeds that of the transport aircraft analyzed from the handling quality data.

5.4. Yawing moment due to sideslip

The optimized parameters θ are used to rank the design parameters on their influence on C_{n_β} in Table 5.5. From the table, it appears that the winglet cant angle is the most active parameter, followed by the winglet length and leading edge sweep angle, and then the winglet taper ratio and wing taper ratio as the least active parameters.

Table 5.5: Ranking of parameters influencing C_{n_β} based on activity parameter θ

Parameter	θ
Cant	1.3252
Length	1.0378
Sweep	1.0314
Wing taper	0.9546
Winglet taper	0.8727

The influence of the winglet length, cant angle, and sweep angle on C_{n_β} based on the Kriging approximation model is shown in Figure 5.7. The figure shows the trends in C_{n_β} for varying winglet lengths from 3 m to 12 m, at seven values of cant angle and four values of leading edge sweep angle. The winglet taper ratio is fixed at 0.65 and the wing taper ratio is fixed at 0.15. Note that the values of C_{n_β} are calculated with reference point at a forward CG location, i.e., with a static margin of 15%. Note also that the average value of C_{n_β} from an analysis of existing handling quality data on representative contemporary transport aircraft is indicated in the figure by a dashed horizontal line. In almost all cases, increasing the winglet length increases C_{n_β} , the exceptions being for cant angles at the upper end of the range tested and at higher sweep angles. Increasing the cant angle shifts the curve down, resulting in lower values of C_{n_β} . Increasing the cant angle also appears to reduce the slope of the curve, particularly at higher sweep angles; this results in flat or even slightly negative trends for high cant angles at higher sweep angles. Increasing the sweep angle has the effect of shifting the curves down, as well as reducing the slope of each curve.

The trends appearing in Figure 5.7 and discussed above appear logical for lower winglet leading edge sweep angles, across the range of winglet lengths and cant angles. As was the case when

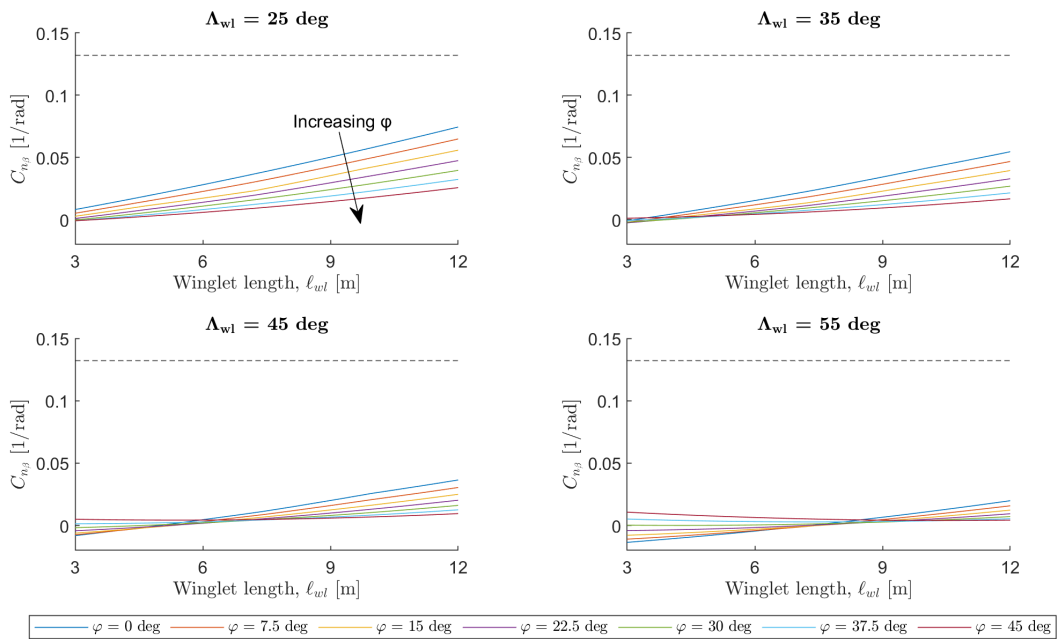


Figure 5.7: Influence of winglet length, cant angle, and leading-edge sweep angle on C_{n_β} at forward CG location

discussing the side force derivative, an increase in winglet length results in an increase in the winglet side area across all combinations of cant and sweep angles; consequently, the side force generated by the winglet also increases, as does the restorative yawing moment, and C_{n_β} increases. Similarly, reducing the winglet cant angle increases the side area, resulting in increased values of C_{n_β} . The exceptions to these trends are found at higher sweep angles and winglet lengths at the lower end of the tested range. In these exceptional cases, the side area first increases as the cant angle is reduced from the upper end of the tested range, up until an inflection point is reached, after which the side area begins to decrease as the cant angle is reduced further. As discussed in Section 5.2, this is a by-product of the chosen parametrization method for the winglet.

The trends seen in the graphs for $\Lambda_{wl} = 45^\circ$ and $\Lambda_{wl} = 55^\circ$, where a higher cant angle results in a higher C_{n_β} for shorter winglet lengths, may be explained partially by the above mentioned geometric trends at high sweep angles and lower winglet lengths. However, this reduction in side area likely does not capture the phenomenon entirely. As mentioned previously, the aerodynamic data extracted from FlightStream indicates that, as the winglet cant angle increases, the percentage of the total lift generated by the winglets increases. This is particularly true for winglets with higher leading edge sweep angles. Concurrently, as the cant angle increases, the outboard wing area decreases due to the span correction built in to the winglet parametrization; this results in a decrease in lift produced at the outboard wing sections. As the lift shifts outboard towards the winglets, the induced drag at the winglets also increases. This increase in induced drag may explain why at higher winglet leading edge sweep angles and shorter winglet lengths, a higher cant angle results in greater values of C_{n_β} . Due to the high sweep angle of the Flying-V inboard wing, as the aircraft is subjected to sideslip, the induced drag (and the profile drag) at the most outboard sections of the upwind wing act on a longer moment arm to the CG (see Figure 2.4). The induced drag at the upwind winglet is also greater than that at the downwind winglet. The combination of increased induced drag and longer moment arm of the upwind winglet produces a net restorative yawing moment that would tend to reduce sideslip, resulting in greater values of C_{n_β} for these for shorter winglets with high sweep angle and higher cant angle. This is seen only for winglets at the lower end of the tested range of winglet lengths (up until approximately $\ell_{wl} = 6$ m for $\Lambda_{wl} = 45^\circ$, and $\ell_{wl} = 8$ m for $\Lambda_{wl} = 55^\circ$); above this threshold, the increased side area of winglets with lower cant angles likely has a dominant effect on the side force produced, and thus the restorative yawing moment produced, and a lower cant angle will always result in a greater value of C_{n_β} .

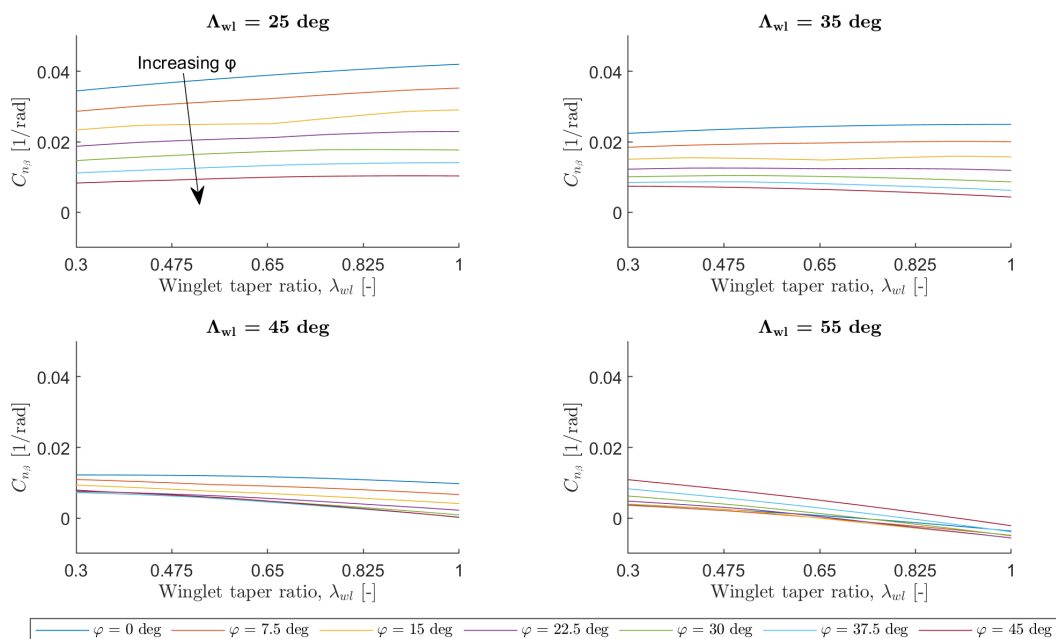


Figure 5.8: Influence of winglet taper ratio on C_{n_β} at forward CG location

The influence of the winglet taper ratio on C_{n_β} based on the Kriging approximation model is shown in Figure 5.8. The winglet length is fixed at 7.5 m and the wing taper ratio is fixed at 0.15. Note that the values of C_{n_β} are calculated with reference point at a forward CG location, i.e., with a static margin of 15%. At lower sweep angles, the curves are notably flat across all cant angles. For higher sweep angles, increasing the winglet taper ratio appears to decrease C_{n_β} .

The trends seen in Figure 5.8 generally align with what would be expected, and also align well with the trends of Figure 5.2 for the influence of winglet taper ratio on C_{y_β} . With the winglet length fixed at 7.5 m, it can be seen clearly that increasing the cant angle results in a smaller value of C_{n_β} as the side area of the winglet is reduced. This is more pronounced at lower sweep angles, which is a by-product of the chosen parametrization method of the winglet. For a majority of the range of tested winglet leading edge sweep angles, an increase in winglet taper ratio results in a greater value of C_{n_β} due to the increased side area of the winglet. The only exceptions to this trend are at the upper end of the range of sweep angles tested, where increasing the winglet taper ratio has a marginally decreasing effect on C_{n_β} . This is likely a result of the parametrization method chosen, or may also be a result of systematic error or noise in the data due to small changes in computational mesh between test cases. Nevertheless, the effect of the winglet taper ratio on C_{n_β} is marginal compared to the other design variables.

The influence of the wing taper ratio on C_{n_β} based on the Kriging approximation model is shown in Figure 5.9. The winglet length is fixed at 7.5 m and the winglet taper ratio is fixed at 0.65. Note that the values of C_{n_β} are calculated with reference point at a forward CG location, i.e., with a static margin of 15%. Increasing the wing taper ratio appears to increase C_{n_β} for lower cant angles and decrease C_{n_β} for higher cant angles. The differences between the trends for low and high cant angles are more pronounced at high sweep angles.

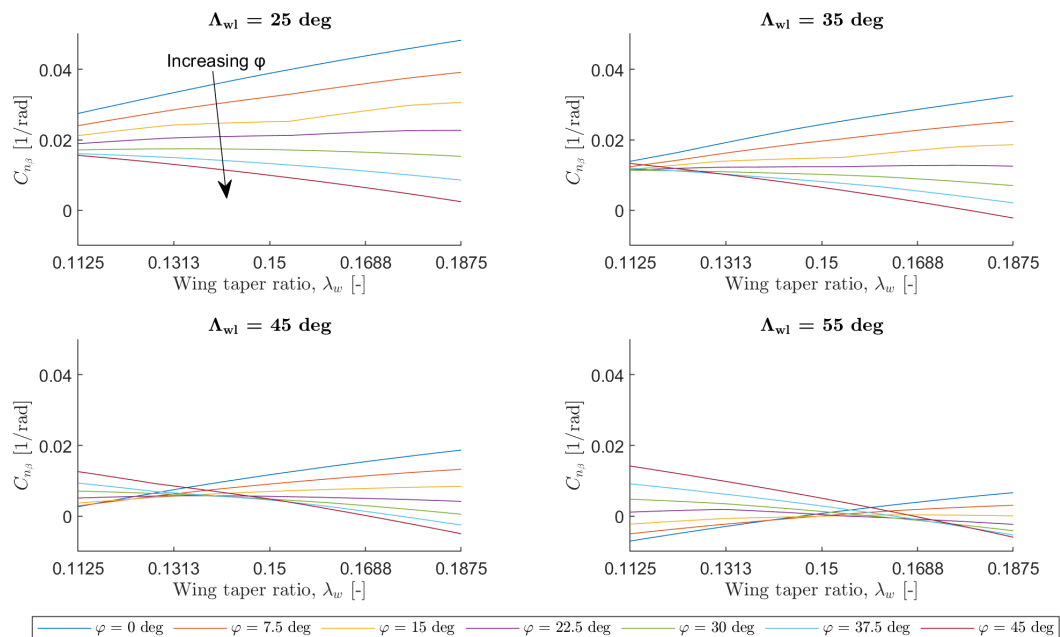


Figure 5.9: Influence of wing taper ratio on C_{n_β} at forward CG location

The trends in Figure 5.9 generally align with the trends seen in Figures 5.7 and 5.8 and described above. Increasing the wing taper, while keeping the winglet taper ratio constant, still has the effect of increasing the winglet side area. This results in greater values of C_{n_β} at lower cant angles. At higher cant angles, however, this increase is not observed. This is likely a result of the parametrization method chosen, or may also be a result of systematic error or noise in the data due to small changes in computational mesh between test cases. Nevertheless, the effect of the wing taper ratio on C_{n_β} is marginal compared to the other design variables.

As a final note, the magnitude of the $C_{n\beta}$ values compared to a ‘target’ value from an analysis of existing handling quality data on representative contemporary transport aircraft [6, 7] is discussed. From Table 2.1, the average value of $C_{n\beta}$ observed is 0.13 with a sample standard deviation of 0.02. To be within one standard deviation of the average observed, the target value for $C_{n\beta}$ is 0.11. As is evident in Figure 5.7, even the highest predicted value of $C_{n\beta} = 0.074$, for a winglet of length $\ell_{wl} = 12$ m, cant angle $\varphi = 0^\circ$ and leading edge sweep angle $\Lambda_{wl} = 25^\circ$, does not fall close to the range of observed values. However, the aircraft sampled to calculate this average value had an average wing area of approximately 255 m², whereas the Flying-V wing area used to calculate the aerodynamic coefficients is 927 m², more than 3.5 times greater. To account for this discrepancy in wing area used to calculate $C_{n\beta}$, a brief analysis of the dimensional derivative N_β , calculated as shown in equation 2.3, is provided.

The value of I_z used to calculate N_β for the Flying-V winglet cases is the value calculated using a moments of inertia model from [4] for the Flying-V at operating empty weight (OEW). This value of I_z at OEW is chosen because only two cases were sampled in the analysis of the Flying-V inertia model in [4]: maximum takeoff weight (MTOW) and operating empty weight. From these two cases, OEW more closely matches the analysis of the current research at simulated approach conditions. Although the Flying-V geometric model used in [4] does not match the model in the current research exactly, it was the only available data on the inertia properties of the aircraft, and is satisfactory for an estimate of the dimensional derivative N_β . The influence of the winglet length, cant angle, and sweep angle on N_β based on the Kriging approximation model is shown in Figure 5.10. The figure shows the trends in N_β for varying winglet lengths from 3 m to 12 m, at seven values of cant angle and four values of leading edge sweep angle. The winglet taper ratio is fixed at 0.65 and the wing taper ratio is fixed at 0.15. Note that the values of N_β are calculated with reference point at a forward CG location, i.e., with a static margin of 15 %.

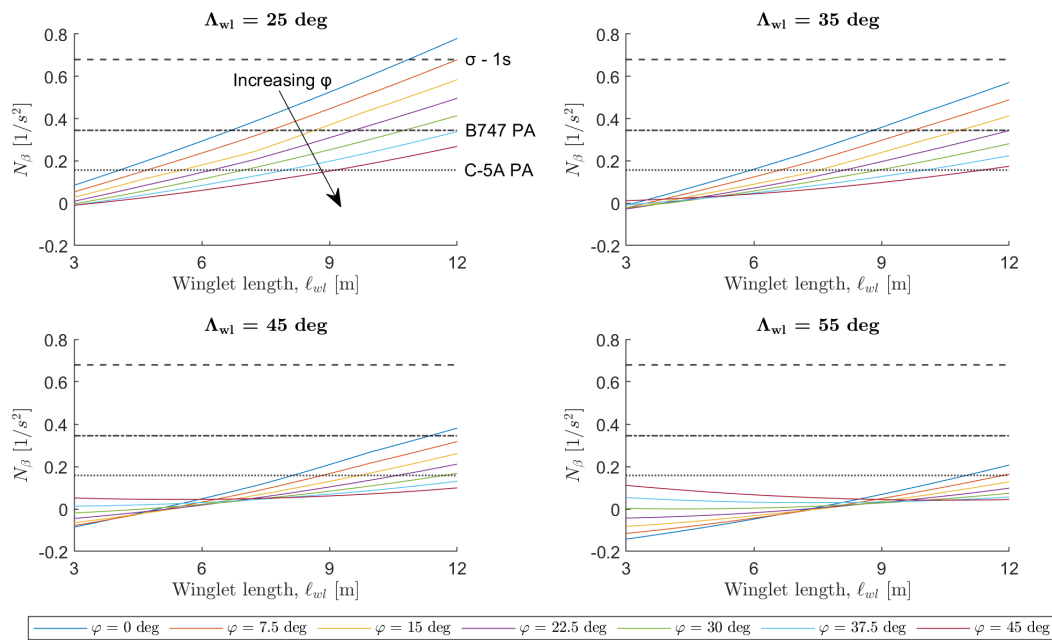


Figure 5.10: Influence of winglet length, cant angle, and leading-edge sweep angle on N_β at forward CG location

The average value of N_β observed from the handling quality data on representative contemporary aircraft is 1.26 with a sample standard deviation of 0.58. To be within one standard deviation of the average observed, the target value for N_β is 0.68. The dashed line in Figure 5.10 and labeled ‘ $\sigma - 1s$ ’ denotes the value of one sample standard deviation below the mean. As is evident in the figure, nearly all of the values of N_β calculated fall below this line, with the exception of the winglets longer than approximately $\ell_{wl} = 10.5$ m for $\Lambda_{wl} = 25^\circ$ and $\varphi = 0^\circ$. For comparison, two more lines are included in Figure 5.10: the value of $N_\beta = 0.345$ for the Boeing 747 at power approach conditions is marked as a dash-dot line and labeled ‘B747 PA’, and the value of $N_\beta = 0.157$ for the Lockheed C-5A at power approach conditions is marked as a dotted line and labeled ‘C-5A PA’. The Many more combinations of

winglet length, sweep angle, and cant angle on the Flying-V result in a value of N_β that lies above that of the B747 in power approach conditions; even more combinations result in a value that lies above that of the C-5A in power approach conditions. This indicates that, although every value of C_{n_β} calculated or predicted in the current research falls far below the ‘target’ values from literature, adequate directional stability may still be achieved by a winglet of moderate length at lower cant and lower leading edge sweep angles.

5.5. Lift-to-drag ratio

The optimized parameters θ are used to rank the design parameters on their influence on the lift-to-drag ratio in Table 5.6. From the table, it appears that the winglet leading edge sweep angle is the most active parameter, followed by the cant angle, winglet length, and wing taper ratio, and then the winglet taper ratio as the least active parameters. The winglet taper ratio has notably little influence on the lift-to-drag ratio, according to its optimal θ value.

Table 5.6: Ranking of parameters influencing C_L/C_D based on activity parameter θ

Parameter	θ
Sweep	1.1892
Cant	0.8836
Length	0.7807
Wing taper	0.6898
Winglet taper	0.0690

The influence of the winglet length, cant angle, and sweep angle on the lift-to-drag ratio based on the Kriging approximation model is shown in Figure 5.11. The figure shows the trends in C_L/C_D for varying winglet lengths from 3 m to 12 m, at seven values of cant angle and four values of leading edge sweep angle. The winglet taper ratio is fixed at 0.65 and the wing taper ratio is fixed at 0.15. Note that the value of $C_L/C_D = 22.83$ from the winglet-off analysis of the Flying-V is indicated in the figure by a dashed horizontal line. Increasing the cant angle has the effect of shifting the C_L/C_D curve downward, such that the lower cant angles most often result in a higher lift-to-drag ratio. For lower cant angles, the trend also shows an increase in C_L/C_D with increased winglet length for nearly the entire range

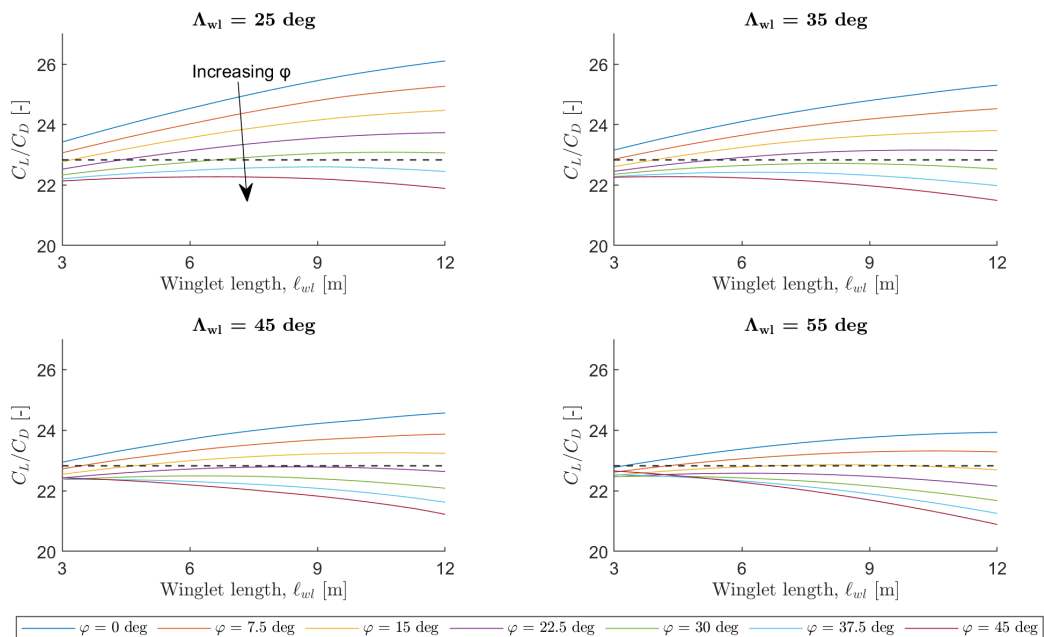


Figure 5.11: Influence of winglet length, cant angle, and leading-edge sweep angle on C_L/C_D

of winglet lengths, whereas for the higher cant angles, the curves reach a plateau and then begin to decrease again; this plateau is reached at progressively shorter winglet lengths as the cant angle is increased. Increasing the sweep angle also has the effect of shifting the C_L/C_D curves downward, as well as reducing the winglet length at which the curves plateau and begin to decrease. This results in curves that are decreasing for the entire range of winglet lengths when the cant and sweep angles are at the upper end of their ranges, meaning that any increase in winglet length will be at a detriment to the lift-to-drag ratio.

As is evident in Figure 5.11, many combinations of winglet length, sweep angle, and cant angle result in an aerodynamic efficiency greater than that of the baseline Flying-V without winglets. Introducing winglets on a wing may improve aerodynamic efficiency at a given lift coefficient by decreasing the lift induced drag, or more specifically, the trailing edge vortex drag [33]. The reduction in trailing edge vortex drag must exceed the increase in profile drag for the winglet to be effective in increasing aerodynamic efficiency. Only five of the 50 winglet configurations analyzed in FlightStream had greater induced drag than the baseline Flying-V without winglets; all of these configurations had a cant angle greater than $\varphi = 30^\circ$. This observation, as well as the trends observed in the figure for increasing cant angle, seem to contradict aerodynamic theory as well as past research [15], which suggest that increasing the outboard cant angle of the winglet should result in a greater reduction in trailing edge vortex drag. In fact, from lifting-line theory, the most efficient winglet would be a winglet with a cant angle $\varphi = 90^\circ$, which is in essence a wing tip extension [33]. There are a number of factors that may explain why this is not observed in the current research. First, the above assertion from lifting-line theory that a wing tip extension has the greatest reduction in induced drag is true for ab initio designs, i.e., when the winglet (or wingtip extension) is considered from the beginning of the design process. For winglets being added on existing wing designs, this is not always the case, and greater improvements in aerodynamic efficiency are sometimes achieved with winglets that have small cant angles. Additionally, the interaction between the wing and winglet, particularly at the wing-winglet juncture, may have a significant influence on the lift and drag of the outboard wing sections. This interaction can often only be measured with the use of an aerodynamic solver, and is unique to the configuration. As such, it is certainly possible that a combination of the chosen parametrization method, the interaction effects between wing and winglet not considered during the initial design of the wing, and the flight conditions (lift coefficient) chosen for aerodynamic analysis result in increased aerodynamic efficiency for more vertical winglets on the Flying-V.

Note that the spanwise lift distribution of the baseline Flying-V has not been altered or optimized

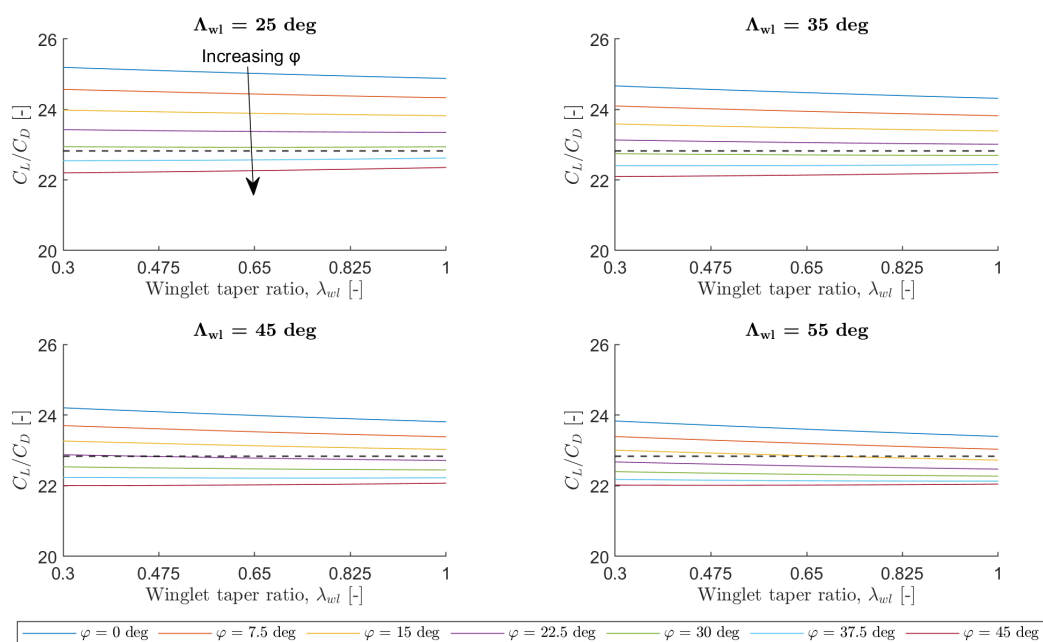


Figure 5.12: Influence of winglet taper ratio on C_L/C_D

either in cruise conditions or for the current flight conditions. This will influence the effect of the winglets on the aerodynamic efficiency. The incremental improvement in C_L/C_D with the addition of winglets is dependent on the spanwise loading of the wing. For example, the improvement in aerodynamic efficiency is often lower when the outboard wing has low wing loading, while the inboard wing has higher wing loading [33]. Fortunately, parameters like the wing twist, dihedral angle, outboard wing and winglet airfoils, winglet twist, and others may be optimized in a future design studies on the aerodynamic optimization of the wing-winglet combination.

The influence of the winglet taper ratio on C_L/C_D based on the Kriging approximation model is shown in Figure 5.12. The winglet length is fixed at 7.5 m and the wing taper ratio is fixed at 0.15. Note that the value of $C_L/C_D = 22.83$ from the winglet-off analysis of the Flying-V is indicated in the figure by a dashed horizontal line. As expected from the activity parameter analysis, the winglet taper ratio has a limited effect. The C_L/C_D curves are notably flat across the range of cant angles and sweep angles.

The trends in Figure 5.12 are logical when considering the activity parameter analysis and the observations discussed above. The slight decrease in aerodynamic efficiency for the lower cant angles may be attributed to an increase in profile drag with increasing winglet taper ratio. Nevertheless, the influence of the winglet taper ratio on the aerodynamic efficiency of the aircraft as a whole is marginal. This parameter could be altered in a future aerodynamic design optimization to maximize C_L/C_D .

The influence of the wing taper ratio on C_L/C_D based on the Kriging approximation model is shown in Figure 5.13. The winglet length is fixed at 7.5 m and the winglet taper ratio is fixed at 0.65. Note that the value of $C_L/C_D = 22.83$ from the winglet-off analysis of the Flying-V is indicated in the figure by a dashed horizontal line. Increasing the wing taper ratio appears to slightly increase the lift-to-drag ratio up until a wing taper ratio of approximately 0.17, at which point the C_L/C_D curve plateaus and begins to decrease again. This trend is seen across the range of cant angles and sweep angles.

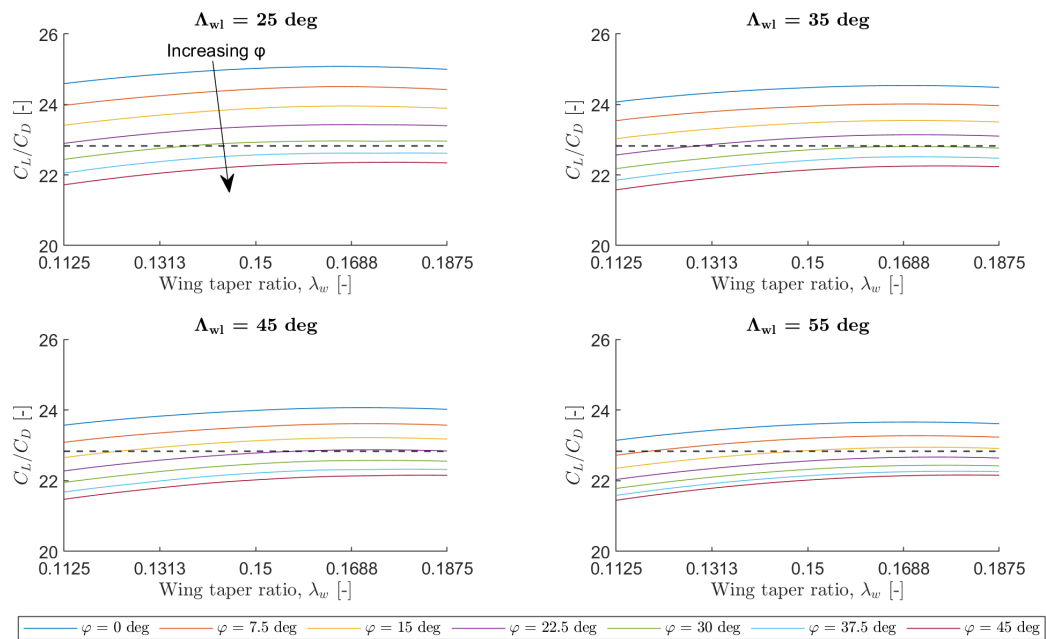


Figure 5.13: Influence of wing taper ratio on C_L/C_D

Altering the wing taper ratio will have an effect on the lift and drag properties of the outboard wing, as well as the spanwise lift distribution. This parameter may be altered in future aerodynamic design optimization exercises to maximize the aerodynamic efficiency of the aircraft.

5.6. Lateral control departure parameter

Using information on the rolling moment due to aileron deflection, $C_{l_{\delta_a}}$, and yawing moment due to aileron deflection, $C_{n_{\delta_a}}$, from the analysis of the Flying-V in Odilila [4], the lateral control departure parameter (calculated as shown in equation 3.3), a parameter indicating closed-loop roll control diver-

gence, is found to be negative for nearly every winglet geometric configurations tested in FlightStream. A negative LCDP is often indicative of roll control reversal; as such, the target value for this metric is 0.0. Note that roll reversal has not been observed in previous analyses of the Flying-V. However, this result is likely due to the different analysis techniques being used to determine the different quantities used to calculate the LCDP.

The optimized parameters θ are used to rank the design parameters on their influence on the lateral control departure parameter in Table 5.7. From the table, it appears that the winglet cant angle is the most active parameter, followed by the winglet length, winglet taper ratio, sweep angle, and wing taper ratio. All of the values of θ are notably close together, suggesting that each parameter influences the LCDP. However, this should be taken as a preliminary result requiring further investigation, as there is likely nontrivial error in the calculation of the LCDP as mentioned above.

Table 5.7: Ranking of parameters influencing LCDP based on activity parameter θ

Parameter	θ
Cant	1.3049
Length	1.1109
Winglet taper	0.9816
Sweep	0.9635
Wing taper	0.9458

The influence of the winglet length, cant angle, and sweep angle on the lateral control departure parameter based on the Kriging approximation model is shown in Figure 5.14. The figure shows the trends in LCDP for varying winglet lengths from 3 m to 12 m, at seven values of cant angle and four values of leading edge sweep angle. The winglet taper ratio is fixed at 0.65 and the wing taper ratio is fixed at 0.15. The trends in the figure closely match those observed in Figure 5.7. In almost all cases, increasing the winglet length increases LCDP, the exceptions being for cant angles at the upper end of the range tested and at higher sweep angles. Increasing the cant angle shifts the curve down, resulting in lower values of LCDP. Increasing the cant angle also appears to reduce the slope of the curve, particularly at higher sweep angles; this results in flat or even slightly negative trends for high cant angles at higher sweep angles. Increasing the sweep angle has the effect of shifting the curves down, as well as reducing the slope of each curve.

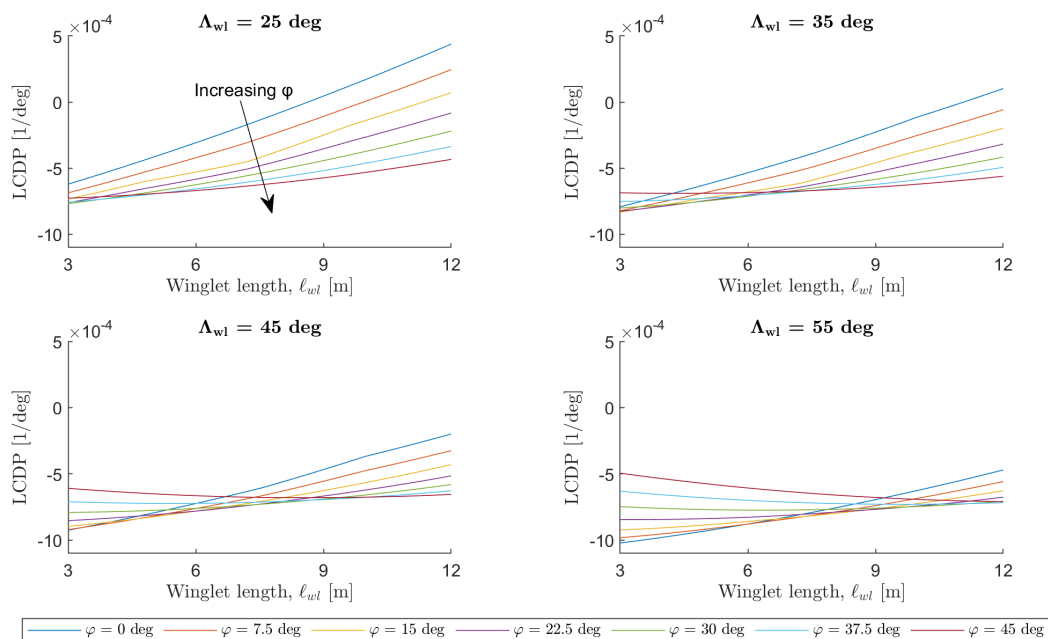


Figure 5.14: Influence of winglet length, cant angle, and leading-edge sweep angle on LCDP at forward CG location

The trends in Figure 5.14 are logical given the similarity of the trends to those observed in Figure 5.7 showing the effect of winglet length, sweep angle, and cant angle on C_{n_β} . The LCDP depends on both C_{n_β} and C_{l_β} ; however, the C_{l_β} term in equation 3.3 has notably smaller influence as the ratio $C_{n_{\delta_a}}/C_{l_{\delta_a}}$ is much less than 1 for the Flying-V (from the Odilila data [4]). As such, the trends for LCDP mirroring those observed for C_{n_β} is logical. For this reason, the figures showing the influence of winglet taper ratio and wing taper ratio are omitted.

Note that almost every combination of winglet length, sweep angle, and cant angle result in a negative predicted value of the LCDP, which, as mentioned above, would suggest roll control reversal. However, this should be taken as a preliminary result requiring further investigation, as there is likely nontrivial error in the calculation of the LCDP as mentioned above.

The parameter $C_{n_{\beta_{DYN}}}$, which is an open loop stability parameter calculated as shown in equation 5.1, is often used alongside the lateral control departure parameter to predict departure susceptibility. $C_{n_{\beta_{DYN}}}$ may be considered a rough estimate of the undamped natural frequency of the Dutch roll mode of an aircraft. A positive value of $C_{n_{\beta_{DYN}}}$ has been determined in literature to be an indicator of possible resistance to departure, though this criterion alone may be insufficient and should not be used alone to rule out departure susceptibility [27]. Some researchers have suggested a minimum value of 0.004 [1/deg] for $C_{n_{\beta_{DYN}}}$; this value will be considered the target value for this metric, though reaching this target is of less importance if certain criteria are met as described below. For comparison, the highest calculated value of $C_{n_{\beta_{DYN}}}$ from the configurations tested in FlightStream is 0.0029. Note that the values I_z and I_x used in the calculation of $C_{n_{\beta_{DYN}}}$ for the Flying-V winglet test cases are those from [4] for the Flying-V at operating empty weight; the value of C_{n_β} is calculated with the reference point at a forward CG location, i.e., with 15 % static margin.

$$C_{n_{\beta_{DYN}}} = C_{n_\beta} \cos \alpha - \frac{I_z}{I_x} (C_{l_\beta} \sin \alpha) \quad (5.1)$$

The most widely used departure and spin susceptibility criterion were derived empirically and developed by Weissman [34], and involve plotting the LCDP vs $C_{n_{\beta_{DYN}}}$. These values are plotted for the fifty configurations tested in FlightStream in the current research in Figure 5.15; each geometric configuration is marked on the plot with a black 'x'. Note that the values calculated for the baseline Flying-V without winglets are also plotted in the figure as a red circle. The different regions marked in the figure indicate potential susceptibility to departure as outlined below [20, 34]:

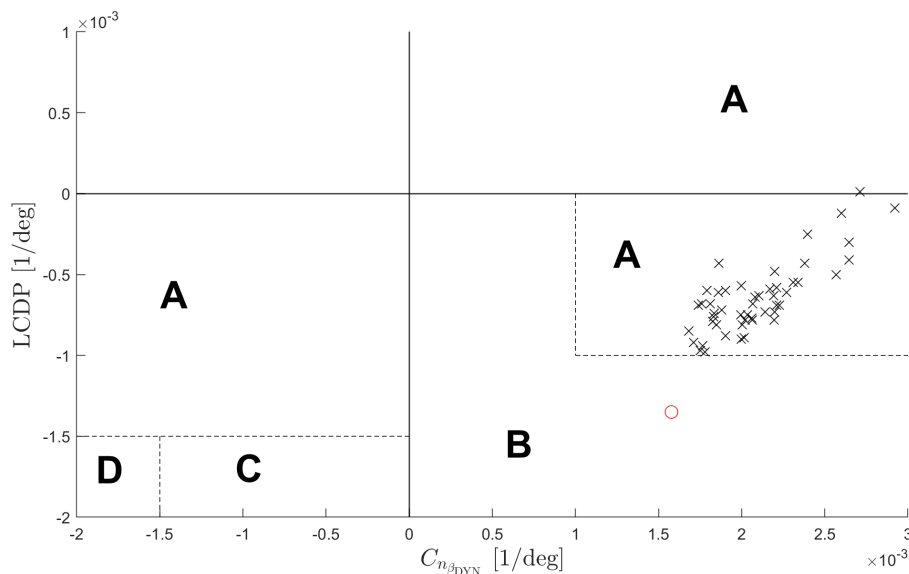


Figure 5.15: Weissman Departure and Spin Susceptibility Criterion

Region A: No departure.

Region B: Mild initial yaw divergence followed by roll reversal (mild rolling departure); low spin susceptibility.

Region C: Moderate initial yaw divergence followed by roll reversal (moderate rolling departure); moderate spin susceptibility.

Region D: Strong directional divergence with roll reversal; high spin susceptibility.

As is evident in the figure, all 50 configurations fall within region A, indicating that they would not be susceptible to yaw divergence, rolling departure, or spin. The baseline configuration without winglets falls within region B, indicating that it could exhibit mild initial yaw divergence, mild rolling departure, and low spin susceptibility. Note that the values indicated in the figure correspond to a Flying-V at operating empty weight, with the most forward CG location. Note also that a satisfactory assessment of the departure behavior of the aircraft necessitates a full dynamic analysis or piloted simulation; the dynamic behavior of the Flying-V in the current research is estimated only using static stability and control derivatives.

5.7. Yawing moment due to rudder deflection

Finally, an analysis of a rough empirical estimation of the yawing moment due to rudder deflection, as calculated in equations 3.4 and 3.5, is provided.

The optimized parameters θ are used to rank the design parameters on their influence on $C_{n_{\delta_r}}$ in Table 5.8. From the table, it appears that the winglet cant angle is by far the most active parameter, followed by the winglet length, winglet taper ratio, sweep angle, and wing taper ratio. The winglet sweep angle, as well as the wing taper ratio, have notably little effect on $C_{n_{\delta_r}}$ compared to the other design variables.

Table 5.8: Ranking of parameters influencing $C_{n_{\delta_r}}$ based on activity parameter θ

Parameter	θ
Cant	2.2082
Length	0.8203
Winglet taper	0.6404
Sweep	0.2379
Wing taper	0.0929

The influence of the winglet length, cant angle, and sweep angle on $C_{n_{\delta_r}}$ based on the Kriging approximation model is shown in Figure 5.16. The figure shows the trends in $C_{n_{\delta_r}}$ for varying winglet lengths from 3 m to 12 m, at seven values of cant angle and four values of leading edge sweep angle. The winglet taper ratio is fixed at 0.65 and the wing taper ratio is fixed at 0.15. The trends in the figure closely match those observed in Figure 5.1. In almost all cases, increasing the winglet length results in a more negative value of $C_{n_{\delta_r}}$, the exceptions being for higher cant angles at higher sweep angles. Increasing the cant angle shifts the curves upward and reduces the slopes of the curves, resulting in less negative values of $C_{n_{\delta_r}}$ and flat or even slightly increasing trends for high cant angles at higher sweep angles. Increasing the sweep angle has the effect of shifting the curves upward, as well as increasing the slope of each curve.

The trends in Figure 5.16 align well with what would be expected. As the value of $C_{n_{\delta_r}}$ is dependent on the lift curve slope of the vertical tail surfaces, which is equal to $C_{y_{\beta}}$ in the current research, it is logical that the trends seen in the figure closely mirror those seen in Figure 5.1. As the side area of the winglet increases, the control power of the a rudder-incorporated winglet increases as the side force of the winglets also increases. The figures showing the influence of winglet taper ratio and wing taper ratio are omitted as they also closely mirror the trends seen in the analysis of the side force derivative. Increasing the winglet taper ratio has the effect of increasing the side area, increasing the value of $C_{n_{\delta_r}}$. The wing taper ratio has notably little influence on $C_{n_{\delta_r}}$, as was suggested in the activity parameter analysis. Note that the values predicted in Figure 5.16 are calculated with reference point

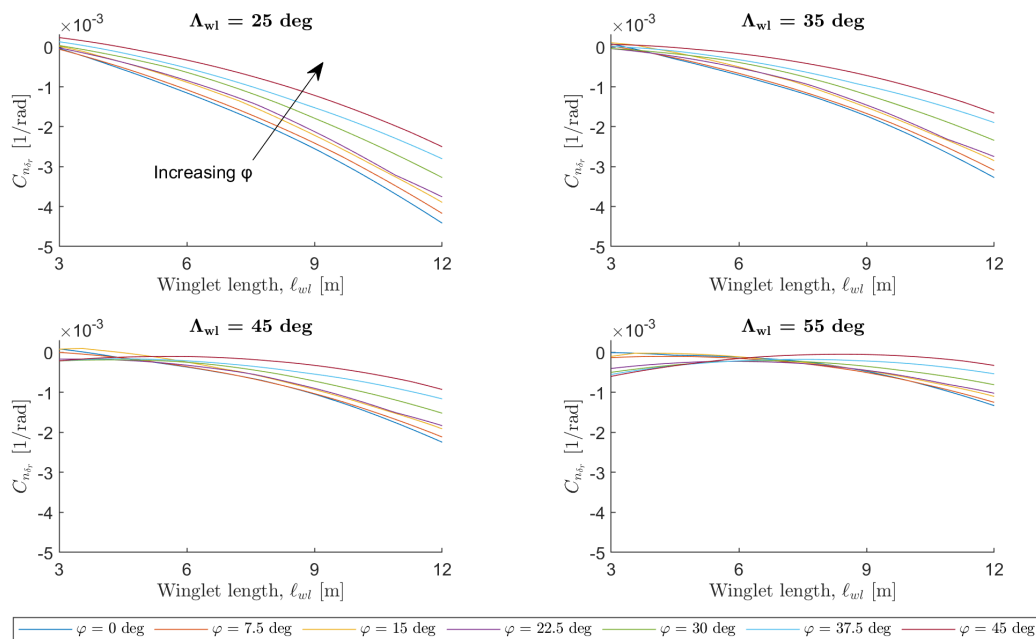


Figure 5.16: Influence of winglet length, cant angle, and leading-edge sweep angle on LCDP at forward CG location, $\tau = 0.8$

at a forward CG location. The tail efficiency factor is assumed to be 1 as the flow is assumed to be undisturbed at the winglets. The flap effectiveness parameter is assumed to be $\tau = 0.8$, which would correspond to a control surface area-to-lifting surface area ratio of approximately 0.7.

As a final note, the magnitude of the $C_{n\delta_r}$ values compared to a ‘target’ value from an analysis of existing handling quality data on representative contemporary transport aircraft [6] is discussed. The average value of $C_{n\delta_r}$ observed is -0.098 with a sample standard deviation of 0.018 . To be within one standard deviation of the average observed, the target value for $C_{n\delta_r}$ is -0.08 . As is evident in Figure 5.16, even the lowest predicted value of $C_{n\delta_r} = -0.0044$, for a winglet of length $\ell_{wl} = 12$ m, cant angle $\varphi = 0^\circ$ and leading edge sweep angle $\Lambda_{wl} = 25^\circ$, does not fall close to the range of observed values; it is at least one order of magnitude smaller. This indicates a deficiency in directional control power of the aircraft, which is consistent with previous analyses of the aircraft yaw control capabilities [4]. This will prove most challenging in critical flight conditions such as one engine inoperative and maximum crosswind landing. Note that this estimate of $C_{n\delta_r}$ is calculated using a very rough empirical estimation that is intended for use analyzing a conventional vertical tail on a conventionally configured aircraft. As such, this prediction should be regarded as preliminary and requiring further investigation, as there is likely nontrivial error in the calculation of $C_{n\delta_r}$. A dedicated study into the design and performance of the Flying-V directional control surfaces and control system is necessary. The possibility of employing split-drag rudders on the outboard wing or winglet, as suggested in [4], could still be a viable option to consider when addressing this directional control deficiency.

5.8. Winglet geometry recommendation for future work

From the presentation and analysis of the results of the current research on the effect of the parametric design of the Flying-V winglets on the lateral-directional stability and control properties of the aircraft, some conclusions may be drawn with respect to a best, or rather sufficient, geometric definition of the winglet to use as a starting point in future research. In terms of the winglet cant angle, a cant angle $\varphi = 0^\circ$ results in the best performance across all stability and control metrics; $\varphi = 0^\circ$ also exhibits the best aerodynamic efficiency predicted in the current research. Similarly, a leading edge sweep angle $\Lambda_{wl} = 25^\circ$ results in the best performance across all stability and control metrics; $\Lambda_{wl} = 25^\circ$ also exhibits the best aerodynamic efficiency predicted in the current research.

Given the relatively limited effect (in comparison to the other design variable) of the winglet taper

ratio on $C_{y\beta}$, $C_{l\beta}$, and $C_{n\beta}$, a winglet taper ratio $\lambda_{wl} = 0.65$ is suggested to limit a reduction in aerodynamic efficiency. Similarly, given the relatively limited effect of the wing taper ratio on $C_{y\beta}$, $C_{l\beta}$, and $C_{n\beta}$, a wing taper ratio $\lambda_w = 0.15$ is suggested. This is equal to the value of the wing taper ratio of the baseline Flying-V without winglets.

A suggestion for the winglet length is somewhat more nuanced. Given the data presented in this chapter, a winglet length of $\ell_{wl} = 12$ m could be suggested as it maximizes performance in terms of both the stability and control metrics as well as the aerodynamic efficiency. However, the change in wing weight is not considered in the current research, as the analysis was strictly an aerodynamic analysis; these results may change when the effect of adding the wing on the wing weight is analyzed. As such, a winglet as short as $\ell_{wl} = 9$ m may be sufficient. A winglet of this length and having the remaining design parameters as recommended above would still exhibit adequate performance particularly in terms of the dimensional directional stability derivative, as the value of N_β is predicted to lie well above those calculated for numerous representative contemporary transport aircraft in literature.

The recommended values for the winglet parameters to be used as a starting point for future research on the outboard wing and winglet are collected in Table 5.9. The resulting stability and control metrics predicted for this winglet geometry, along with the target values for these metrics, are shown in Table 5.10. The Flying-V configuration with this winglet geometry exhibits strong lateral stability, satisfactory directional stability from an analysis of N_β , an increase in C_L/C_D of 13.4% over the baseline aircraft without winglets, and is not shown to be susceptible to departure from a preliminary analysis of the lateral control departure parameter and $C_{n\beta_{DYN}}$. Note that the target value of the yawing moment due to rudder deflection is not met for any winglet within the design space of the current research.

Table 5.9: Recommended values of winglet design variables for future work

Parameter	Symbol	Value	Unit
Length	ℓ_{wl}	10.90	[m]
Cant angle	φ	0.00	[deg]
Leading edge sweep angle	Λ_{wl}	25.00	[deg]
Winglet taper ratio	λ_{wl}	0.65	[-]
Wing taper ratio	λ_w	0.15	[-]

Table 5.10: Stability and control metrics predicted for recommended winglet geometry

Metric	Value	Target	Unit
$C_{y\beta}$	-0.2421	-0.6900	[1/rad]
$C_{l\beta}$	-0.2656	-0.2200	1/[rad]
$C_{n\beta}$	0.0653	0.1100	[1/rad]
N_β	0.6834	0.6800	[1/s ²]
C_L/C_D	25.8996	maximize	[-]
LCDP	0.0003	0.0000	[1/deg]
$C_{n\beta_{DYN}}$	0.0030	0.0040	[1/deg]
$C_{n\delta_r}$	-0.0037	-0.0800	[1/deg]

Conclusions and Recommendations

6.1. Conclusions

Over the course of the current research task, a parametric definition of the winglet geometry of the Flying-V was devised and implemented within the framework of the knowledge based engineering environment ParaPy to generate a number of geometric configurations. From a thorough review of literature and through the process of defining the winglet geometry in ParaPy, the parameters chosen to most effectively define the geometry and positioning of the Flying-V outboard wing and winglet are: the winglet length, cant angle, leading-edge sweep angle, winglet taper ratio, blend radius, winglet tip twist angle, and overall wing taper ratio. The geometry generation tool ParaPy was used to generate 50 random winglet geometries in a space-filling Latin Hypercube sampling plan in order to achieve a uniform level of surrogate model accuracy throughout the design space and to limit statistical uncertainty of the computed approximation. Each geometry was analyzed using the aerodynamic solver FlightStream to extract aerodynamic data on the lift, drag, and lateral-directional stability characteristics of the configuration at a lift coefficient of $C_L = 0.8$, mach number $M = 0.2$, sea level standard conditions, and with forward CG location as reference point for the calculation of forces and moments. These outputs are then used to construct a global surrogate model in the form of a Kriging approximation model. A second order polynomial regression model and linear correlation model are chosen for the construction of the model to minimize the root mean square error of the prediction and ensure a good global model of the design space. The surrogate model is used to analyze the influence each design variable has on the aerodynamic coefficients and stability and control parameters chosen as good indicators of the aircraft's stability and control characteristics. These stability and control coefficients and parameters are the side force due to sideslip $C_{y\beta}$, the rolling moment due to sideslip $C_{l\beta}$, the yawing moment due to sideslip in both nondimensional form $C_{n\beta}$ and dimensional form N_β , as well as the lateral control departure parameter, an approximation of the undamped natural frequency of the Dutch roll mode $C_{n\beta_{DYN}}$, and an estimate of the rudder control capabilities of a rudder-incorporated winglet $C_{n_{\delta_r}}$.

The target value for the side force derivative $C_{y\beta}$ from a survey of handling quality data on representative contemporary transport aircraft is -0.69 . The winglet sweep angle, length, and cant angle are found to have the greatest influence on the side force due to sideslip. The winglet taper ratio and wing taper ratio have a limited influence on $C_{y\beta}$. The trends show that increasing winglet length almost always results in more negative values of $C_{y\beta}$. Reducing the cant angle and the sweep angle also have the effect of making $C_{y\beta}$ more negative. The value of the side force derivative closest to the target is $C_{y\beta} = -0.27$ for a winglet of length $\ell_{wl} = 12$ m, cant angle $\varphi = 0^\circ$, and sweep angle $\Lambda_{wl} = 25^\circ$.

The target value for the rolling moment due to sideslip $C_{l\beta}$ from a survey of handling quality data on representative contemporary transport aircraft is -0.22 . The winglet sweep angle, length, and cant angle are found to have the greatest influence on the rolling moment due to sideslip. The winglet taper ratio and wing taper ratio have a limited influence on $C_{l\beta}$. The trends show that increasing winglet length results in more negative values of $C_{l\beta}$. Reducing the cant angle and the sweep angle also have the effect of making $C_{l\beta}$ more negative. All predicted values of $C_{l\beta}$ fall below the target value, indicating

that the Flying-V wing with any winglet possesses strong, perhaps excessive, lateral stability.

The target value for the nondimensional yawing moment due to sideslip C_{n_β} from a survey of handling quality data on representative contemporary transport aircraft is 0.11. The winglet sweep angle, length, and cant angle are found to have the greatest influence on the yawing moment due to sideslip. The winglet taper ratio and wing taper ratio influence C_{l_β} to a lesser degree. The trends show that increasing winglet length results in greater values of C_{n_β} , except for cases when both the cant angle and sweep angle are at the upper end of their ranges. Reducing the cant angle and the sweep angle generally also have the effect of increasing C_{n_β} . For shorter winglets with a high sweep angle, the effect is reversed, and increasing the cant angle increases C_{n_β} . The value of the yawing moment due to sideslip closest to the target is $C_{y_\beta} = 0.074$ for a winglet of length $\ell_{wl} = 12$ m, cant angle $\varphi = 0^\circ$, and sweep angle $\Lambda_{wl} = 25^\circ$. The dimensional yawing moment due to sideslip N_β is influenced in the same way as described above. The target value for N_β from a survey of handling quality data on representative contemporary transport aircraft is 0.68. A winglet length $\ell_{wl} = 10.9$ m, cant angle $\varphi = 0^\circ$, and sweep angle $\Lambda_{wl} = 25^\circ$ satisfies this target value.

The target value for the lift-to-drag ratio is the maximum that can be achieved while satisfying restrictions on the stability and control of the aircraft. The winglet sweep angle, cant angle, and length are found to have the greatest influence on the lift-to-drag ratio. Increasing the winglet length increases C_L/C_D for the lower cant angles, but decreases C_L/C_D for the higher cant angles. Reducing the cant angle nearly always results in improved C_L/C_D ; the same trend is found for the sweep angle. The maximum predicted $C_L/C_D = 26.1$ is found for a winglet of length $\ell_{wl} = 12$ m, cant angle $\varphi = 0^\circ$, and sweep angle $\Lambda_{wl} = 25^\circ$.

The target value for the lateral control departure parameter is greater than 0.0. The LCDP is influenced largely in the same way as C_{n_β} as this quantity is the dominant contributor to the value of LCDP. The maximum predicted LCDP = 0.0004 is found for a winglet of length $\ell_{wl} = 12$ m, cant angle $\varphi = 0^\circ$, and sweep angle $\Lambda_{wl} = 25^\circ$. The target value for $C_{n_{\beta_{DYN}}}$ from literature is 0.004. This value is again influenced largely in the same way as C_{n_β} as this quantity is the dominant contributor to the value of $C_{n_{\beta_{DYN}}}$. The predicted value closest to the target is $C_{n_{\beta_{DYN}}} = 0.0032$ for a winglet of length $\ell_{wl} = 12$ m, cant angle $\varphi = 0^\circ$, and sweep angle $\Lambda_{wl} = 25^\circ$.

The target value for the yawing moment due to rudder deflection $C_{n_{\delta_r}}$ from a survey of handling quality data on representative contemporary transport aircraft is -0.08 . This value is influenced largely in the same way as C_{y_β} as this quantity is the dominant contributor to $C_{n_{\delta_r}}$. The predicted value closest to the target is $C_{n_{\delta_r}} = -0.004$ for a winglet of length $\ell_{wl} = 12$ m, cant angle $\varphi = 0^\circ$, and sweep angle $\Lambda_{wl} = 25^\circ$.

From the trends described above, conclusions are drawn with respect to a geometric definition of the Flying-V winglet with satisfactory stability and control performance that maximizes the lift-to-drag ratio, to be used as a starting point in future research. The recommended winglet has a length $\ell_{wl} = 10.9$ m, cant angle $\varphi = 0^\circ$, sweep angle $\Lambda_{wl} = 25^\circ$, winglet taper ratio $\Lambda_{wl} = 0.65$, and wing taper ratio $\Lambda_w = 0.15$. The Flying-V configuration with this winglet geometry exhibits strong lateral stability, satisfactory directional stability from an analysis of N_β , an increase in C_L/C_D of 13.4 % over the baseline aircraft without winglets, and is not shown to be susceptible to departure from a preliminary analysis of the lateral control departure parameter and $C_{n_{\beta_{DYN}}}$. Note that the target value of the yawing moment due to rudder deflection is not met for any winglet within the design space of the current research. Possible solutions include implementing split-drag rudders at the outboard wing or winglets to increase the yaw control capabilities of the aircraft. Note also that the wing weight, which will be affected by the winglet design, is not considered in the current research. As such, a winglet of this length may be found infeasible in a future design study incorporating wing weight in an optimization. The use of a certifiable yaw damper in closed-loop control may be sufficient to damp out oscillations and ensure certifiable departure and Dutch roll performance of the aircraft. As the winglet taper ratio and wing taper ratio were seen to have a limited effect on the stability and control characteristics of the aircraft, these values can be modified in future work to optimize lift and drag characteristics of the Flying-V.

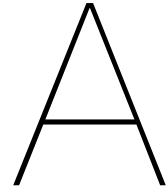
6.2. Recommendations for future work

From the recommended winglet geometry presented above, a full aerodynamic analysis and optimization of the outboard wing and winglet is the next step to ensure the winglet is functioning as a mechanism for lateral-directional stability and control, as well as for improving aerodynamic performance. Parameters such as the winglet twist angle, the airfoils used for the blend and winglet trunk profiles, and the blending radius, can be altered to improve the aerodynamic performance of the aircraft as a whole. A dedicated study into the control surfaces of the aircraft, in which the rudder is modeled and analyzed using an aerodynamic solver, is also necessary to investigate the deficiencies in directional control capability of the Flying-V. Additionally, a 6 degree-of-freedom flight dynamics model would also be beneficial to ensure that the dynamic stability and control properties of the aircraft, including Dutch Roll damping and departure analysis, are captured for varying winglet designs.

Bibliography

- [1] EASA, EEA, and EUROCONTROL. European aviation environmental report 2019. Technical report, European Union Aviation Safety Agency, 2019. Available at <https://www.easa.europa.eu/eaer/>.
- [2] J. Benad. The flying v - a new aircraft configuration for commercial passenger transport. In *Publikationen zum Deutscher Luft- und Raumfahrtkongress*, 2015.
- [3] F. Faggiano. Aerodynamic Design Optimization of a Flying V Aircraft. Master's thesis, Delft University of Technology, the Netherlands, 2016.
- [4] T. Cappuyns. Handling qualities of a flying v configuration. Master's thesis, Delft University of Technology, the Netherlands, 2019.
- [5] Egbert Torenbeek. *Synthesis of Subsonic Airplane Design*. Delft University Press, Delft, NL, 1982. ISBN 90-247-2724-3.
- [6] Robert K. Heffley and Wayne F. Jewell. Aircraft handling qualities data. Technical Report NASA CR-2144, National Aeronautics and Space Administration, Systems Technology, Inc., Hawthorne, Calif., December 1972.
- [7] Walter E. McNeill. Calculated and flight-measured handling-qualities factors of three subsonic jet transports. Technical Report NASA TN D-4832, National Aeronautics and Space Administration, Ames Research Center, Moffett Field, Calif., November 1968.
- [8] C.P. van Dam and J Roskam. Analysis of nonplanar wing-tip-mounted lifting surfaces on low-speed airplanes. 1983. NASA Contractor Report 3684.
- [9] Maximilian Tomac and Gloria Stenfelt. Predictions of stability and control for a flying wing. *Aerospace Science and Technology*, 39:179–186, 2014. ISSN 12709638. doi: 10.1016/j.ast.2014.09.007.
- [10] Bernard Etkin and Lloyd D. Reid. *Dynamics of flight : stability and control*. Wiley, New York, 3rd ed. edition, 1996. ISBN 0471034185 9780471034186.
- [11] Paolo Teofilatto. Preliminary aircraft design: lateral handling qualities. *Aircraft Design*, 4(1):63–73, 2001.
- [12] K. Nickel and M. Wohlfahrt. *Tailless Aircraft: In Theory and Practice*. American Institute of Aeronautics and Astronautics, Inc., Washington DC, 1994. A corrected and widely enlarged translation of the book 'Schwanzlose Flugzeuge' of the two authors, printed 1990 by the Birkhäuser Verlag, Basel.
- [13] Keizo Takenaka, Keita Hatanaka, Wataru Yamazaki, and Kazuhiro Nakahashi. Multidisciplinary design exploration for a winglet. *Journal of Aircraft*, 45(5):1601–1611, 2008. ISSN 0021-8669 1533-3868. doi: 10.2514/1.33031.
- [14] Paul Park and Kamran Rokhsaz. Effects of a winglet rudder on lift-to-drag ratio and wake vortex frequency. In *21st AIAA Applied Aerodynamics Conference*, 2003. doi: 10.2514/6.2003-4069.
- [15] R. Hageman. Rudder Incorporated Winglet Design for Blended Wing Body Aircraft. Master's thesis, Delft University of Technology, the Netherlands, 2016.
- [16] Gianfranco La Rocca. Knowledge based engineering: Between ai and cad. review of a language based technology to support engineering design. *Advanced Engineering Informatics*, 26(2):159–179, 2012. ISSN 14740346. doi: 10.1016/j.aei.2012.02.002.

- [17] G. La Rocca and M. van Tooren. A knowledge based engineering approach to support automatic generation of fe models in aircraft design. In *Proceedings of the 45th AIAA Aerospace Sciences Meeting and Exhibit*. doi: 10.2514/6.2007-967.
- [18] M. Hillen. Parametrisation of the flying-v outer mould line. Master's thesis, Delft University of Technology, the Netherlands, 2020.
- [19] Brenda M. Kulfan. Universal parametric geometry representation method. *Journal of Aircraft*, 45(1):142–158, 2008. ISSN 0021-8669 1533-3868. doi: 10.2514/1.29958.
- [20] Erik D. Olson and Cindy W. Albertson. Aircraft high-lift aerodynamic analysis using a surface-vorticity solver. In *54th AIAA Aerospace Sciences Meeting*, 2016. doi: 10.2514/6.2016-0779.
- [21] Imon Chakraborty, Vivek Ahuja, Anthony Comer, and Omkar Mulekar. Development of a modeling, flight simulation, and control analysis capability for novel vehicle configurations. In *AIAA Aviation 2019 Forum*, page 3112, 2019. doi: 10.2514/6.2019-3112.
- [22] Vivek Ahuja and R. J. Hartfield. Aerodynamic loads over arbitrary bodies by method of integrated circulation. *Journal of Aircraft*, 53(6):1719–1730, 2016. ISSN 0021-8669 1533-3868. doi: 10.2514/1.C033619.
- [23] Vivek Ahuja, Imon Chakraborty, and Roy J. Hartfield. Aero-propulsive analysis for contemporary conceptual design. In *AIAA Aviation 2019 Forum*, page 3019, 2019. doi: 10.2514/6.2019-3019.
- [24] Alexander I.J. Forrester, András Sóbester, and Andy J. Keane. *Engineering Design via Surrogate Modelling: A Practical Guide*. John Wiley & Sons, West Sussex, United Kingdom, 2008. ISBN 978-0-470-06068-1.
- [25] Jason L. Loeppky, Jerome Sacks, and William J. Welch. Choosing the sample size of a computer experiment: A practical guide. *Technometrics*, 51(4):366–376, 2009. ISSN 0040-1706 1537-2723. doi: 10.1198/tech.2009.08040.
- [26] Donald R. Jones, Matthias Schonlau, and William J. Welch. Efficient global optimization of expensive black-box functions. *Journal of Global Optimization*, 13(4):455–492, 1998. ISSN 09255001. doi: 10.1023/A:1008306431147.
- [27] Robert M. Seltzer and Glenn R. Rhodeside. Fundamentals and methods of high angle-of-attack flying qualities research. Technical Report NADC-88020-60, Air Vehicle and Crew Systems Technology Department, Naval Air Development Center, Warminster, PA, January 1988.
- [28] Robert C. Nelson. *Flight stability and automatic control*. WCB/McGraw Hill, Boston, Mass., 2nd ed. edition, 1998. ISBN 0070462739 9780070462731 0071158383 9780071158381.
- [29] Søren N. Lophaven, Hans Bruun Nielsen, and Jacob. Søndergaard. Aspects of the matlab toolbox dace. Technical Report IMM-REP-2002-13, Informatics and Mathematical Modelling, Technical University of Denmark, Kongens Lyngby, Denmark, 2002.
- [30] Vivek Ahuja. *Aerodynamic Loads Over Arbitrary Bodies by Method of Integrated Circulation*. PhD thesis, Auburn University, Auburn, Alabama, August 2013.
- [31] Lynn W. Hunton and Joseph K. Dew. The effects of camber and twist on the aerodynamic loading and stalling characteristics of a large-scale swept-back wing. Technical Report NACA RM A50J24, National Advisory Committee for Aeronautics, Ames Aeronautical Laboratory, Moffett Field, Calif., January 1951.
- [32] M. Palermo. The Longitudinal Static Stability and Control Characteristics of a Flying V Scaled Model. Master's thesis, Delft University of Technology, the Netherlands, 2019.
- [33] Engineering Sciences Data Unit (ESDU). Aerodynamic principles of winglets. Technical Report 98013, June 1998.
- [34] Robert Weissman. Preliminary criteria for predicting departure characteristics and spin susceptibility of fighter-type aircraft. *AIAA Journal of Aircraft*, 10(4), April 1973.



UML Class Diagram

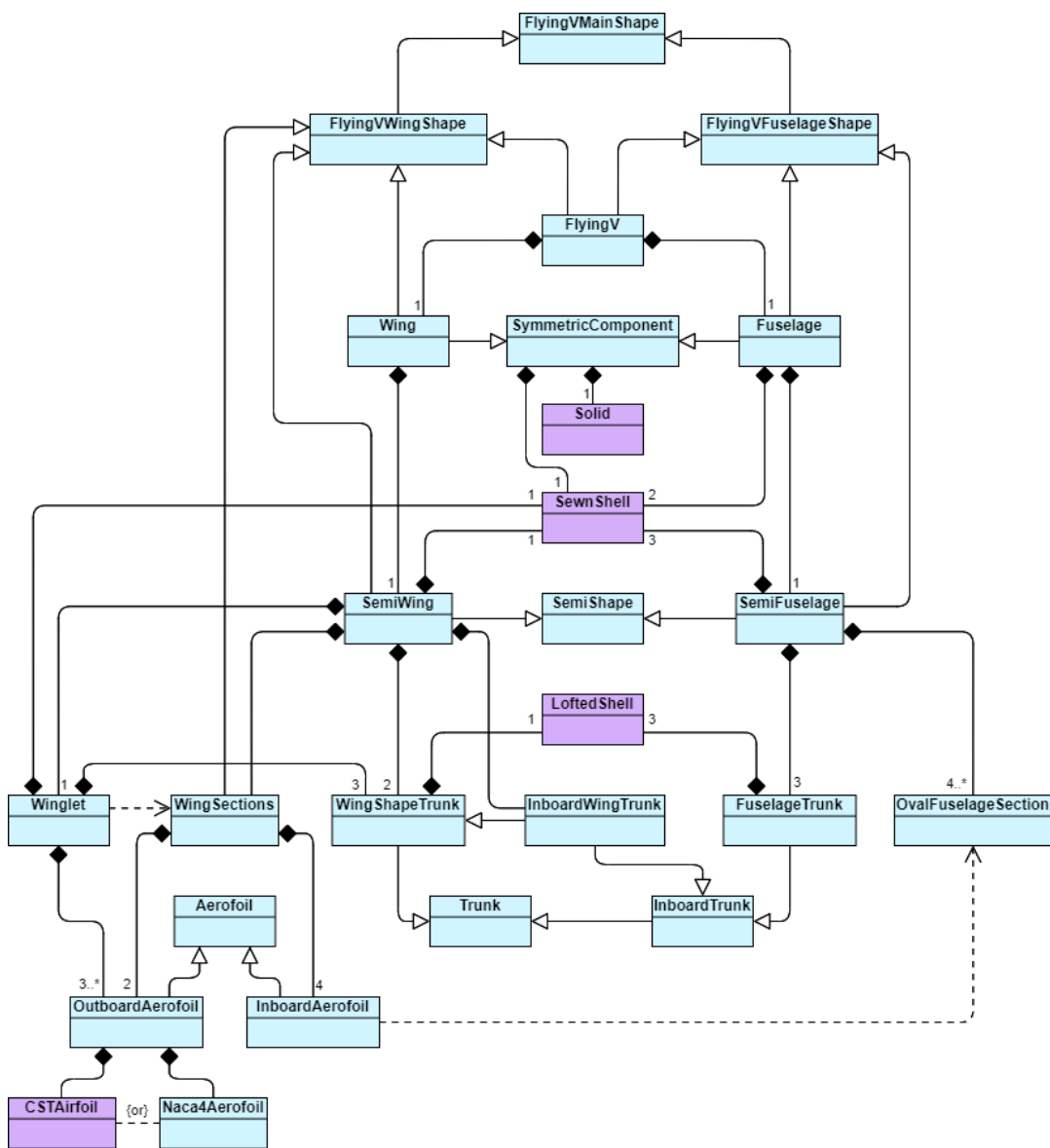


Figure A.1: UML class diagram of Flying-V ParaPy model

B

Sampling Plan

Table B.1: Parameters defining the 50 samples used to construct the Kriging approximation model

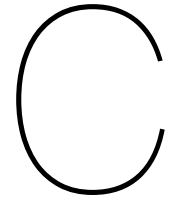
Sample	Length [m]	Cant [deg]	Sweep [deg]	Winglet taper [-]	Wing taper [-]
1	5.7551	32.1429	25.0000	0.6000	0.1737
2	10.5306	7.3469	51.3265	0.9714	0.1584
3	7.9592	18.3673	50.1020	0.8429	0.1676
4	5.5714	37.6531	29.8980	0.3714	0.1247
5	8.3265	22.0408	52.5510	0.5286	0.1309
6	4.6531	10.1020	38.4694	0.9000	0.1844
7	6.4898	39.4898	46.4286	0.9571	0.1722
8	7.2245	15.6122	29.2857	0.6571	0.1538
9	8.5102	42.2449	35.4082	0.7143	0.1829
10	7.0408	40.4082	47.0408	0.7429	0.1278
11	7.4082	8.2653	37.8571	0.8857	0.1156
12	7.5918	11.0204	43.3673	0.3000	0.1431
13	6.1224	25.7143	39.6939	0.4143	0.1875
14	9.9796	1.8367	40.9184	0.6143	0.1492
15	9.2449	41.3265	26.2245	0.4714	0.1508
16	7.7755	34.8980	39.0816	0.5143	0.1615
17	8.8776	20.2041	51.9388	0.3286	0.1798
18	9.4286	23.8776	36.6327	0.5571	0.1140
19	9.0612	0.9184	34.7959	0.7714	0.1783
20	5.2041	33.9796	53.7755	0.6714	0.1477
21	11.8163	16.5306	45.8163	0.7571	0.1263
22	5.3878	3.6735	45.2041	0.7000	0.1339
23	5.0204	43.1633	31.1224	0.8286	0.1462
24	11.4490	21.1224	30.5102	0.4286	0.1385
25	10.8980	22.9592	26.8367	0.8143	0.1707
26	8.1429	31.2245	28.0612	0.7857	0.1125
27	4.1020	29.3878	36.0204	0.6429	0.1293
28	5.9388	44.0816	48.2653	0.3429	0.1523
29	4.8367	12.8571	31.7347	0.3143	0.1768
30	6.8571	27.5510	27.4490	1.0000	0.1569
31	9.6122	6.4286	25.6122	0.4000	0.1661
32	3.5510	14.6939	50.7143	0.5714	0.1186
33	11.6327	28.4694	49.4898	0.5429	0.1630
34	6.3061	13.7755	55.0000	0.4857	0.1645
35	10.3469	9.1837	48.8776	0.4429	0.1171
36	10.7143	19.2857	42.1429	0.6286	0.1860
37	3.0000	26.6327	32.9592	0.8000	0.1691
38	12.0000	36.7347	33.5714	0.6857	0.1324
39	9.7959	30.3061	54.3878	0.9143	0.1202
40	11.0816	38.5714	42.7551	0.3857	0.1232
41	3.3673	24.7959	44.5918	0.9429	0.1416
42	3.9184	35.8163	47.6531	0.5857	0.1814
43	4.2857	5.5102	41.5306	0.4571	0.1599
44	10.1633	11.9388	34.1837	0.9286	0.1446
45	4.4694	0.0000	53.1633	0.7286	0.1753
46	3.1837	17.4490	37.2449	0.3571	0.1355
47	3.7347	4.5918	28.6735	0.8714	0.1370
48	11.2653	45.0000	43.9796	0.8571	0.1554
49	6.6735	2.7551	32.3469	0.5000	0.1217
50	8.6939	33.0612	40.3061	0.9857	0.1401



Figure B.1: Sampling Plan: Samples 1-25



Figure B.2: Sampling Plan: Samples 26-50



FlightStream Data

Table C.1: Raw data from analysis of 50 samples in FlightStream at $C_L = 0.80$, $M = 0.2$, sea level standard conditions; X_{ref} at forward CG location, $S_{ref} = 927.11 \text{ m}^2$, $\bar{c} = 18.23 \text{ m}$ (longitudinal reference length), $b_{ref} = 64.6 \text{ m}$ (lateral reference length)

Sample	X_{ref} [m]	X_{NP} [m]	C_{m_α} [1/rad]	C_{L_α} [1/rad]	C_D [-]	C_{y_β} [1/rad]	C_{l_β} [1/rad]	C_{n_β} [1/rad]
1	30.2552	33.3402	-0.4713	3.1407	0.0355	-0.0926	-0.2681	0.0054
2	30.5609	33.6507	-0.4876	3.2515	0.0339	-0.1166	-0.2687	0.0133
3	30.4730	33.5565	-0.4919	3.2793	0.0349	-0.0840	-0.2746	-0.0003
4	29.2754	32.4102	-0.4584	3.0553	0.0358	-0.0726	-0.2140	0.0145
5	29.6792	32.8072	-0.4718	3.1444	0.0358	-0.0753	-0.2341	0.0087
6	30.8108	33.8997	-0.4996	3.3300	0.0350	-0.0841	-0.2765	-0.0007
7	30.2591	33.3826	-0.4899	3.2656	0.0360	-0.0620	-0.2616	-0.0024
8	30.6620	33.7479	-0.4982	3.3211	0.0338	-0.1262	-0.2730	0.0154
9	29.8718	33.0095	-0.4819	3.2106	0.0359	-0.0937	-0.2782	0.0064
10	29.3827	32.5414	-0.4744	3.1630	0.0366	-0.0601	-0.2312	0.0038
11	30.6573	33.7602	-0.4996	3.3315	0.0343	-0.1005	-0.2553	0.0102
12	30.5347	33.6280	-0.5008	3.3381	0.0341	-0.0966	-0.2448	0.0124
13	30.4031	33.4987	-0.4864	3.2424	0.0352	-0.0858	-0.2681	0.0026
14	30.7466	33.8337	-0.5022	3.3475	0.0329	-0.1501	-0.2555	0.0324
15	29.3606	32.4994	-0.4595	3.0616	0.0358	-0.1062	-0.2568	0.0141
16	29.7275	32.8404	-0.4675	3.1163	0.0354	-0.0852	-0.2559	0.0083
17	30.5047	33.6167	-0.4947	3.2959	0.0348	-0.0887	-0.2691	0.0050
18	29.3164	32.4814	-0.4664	3.1094	0.0357	-0.1065	-0.2459	0.0179
19	31.0703	34.1280	-0.5074	3.3813	0.0322	-0.1869	-0.2673	0.0421
20	29.9950	33.1225	-0.4819	3.2114	0.0360	-0.0524	-0.2303	0.0025
21	29.7281	32.8689	-0.4724	3.1501	0.0353	-0.1183	-0.2671	0.0174
22	30.7404	33.8476	-0.5019	3.3446	0.0345	-0.0699	-0.2522	-0.0002
23	29.8369	32.9665	-0.4735	3.1576	0.0359	-0.0612	-0.2422	0.0030
24	29.5937	32.7126	-0.4638	3.0928	0.0345	-0.1634	-0.2825	0.0286
25	29.9679	33.0587	-0.4804	3.2014	0.0335	-0.2113	-0.2872	0.0474
26	29.1647	32.3179	-0.4555	3.0350	0.0360	-0.1016	-0.2612	0.0164
27	30.1141	33.2388	-0.4801	3.2005	0.0356	-0.0607	-0.2396	0.0015
28	29.7639	32.9020	-0.4784	3.1891	0.0360	-0.0542	-0.2244	0.0067
29	30.8122	33.8776	-0.4847	3.2300	0.0344	-0.0919	-0.2637	0.0054
30	30.3550	33.4622	-0.4947	3.2979	0.0349	-0.1125	-0.2739	0.0110
31	30.6867	33.7263	-0.5013	3.3426	0.0317	-0.2023	-0.2645	0.0493
32	30.2267	33.3544	-0.4876	3.2484	0.0354	-0.0491	-0.2372	-0.0051
33	29.8031	32.9347	-0.4853	3.2346	0.0358	-0.1010	-0.2719	0.0102
34	30.2485	33.3492	-0.4819	3.2126	0.0348	-0.0672	-0.2468	0.0017
35	30.1782	33.2938	-0.4853	3.2361	0.0347	-0.0924	-0.2597	0.0049
36	30.2978	33.3934	-0.4867	3.2464	0.0344	-0.1536	-0.2904	0.0249
37	30.4437	33.5706	-0.5042	3.3624	0.0359	-0.0555	-0.2567	-0.0066
38	28.6633	31.8349	-0.4558	3.0370	0.0368	-0.1203	-0.2563	0.0224
39	29.3867	32.5553	-0.4658	3.1043	0.0372	-0.0684	-0.2561	0.0024
40	28.7292	31.9166	-0.4506	3.0026	0.0379	-0.0766	-0.2488	0.0119
41	30.6335	33.7556	-0.5022	3.3406	0.0359	-0.0476	-0.2483	-0.0073
42	30.5922	33.7087	-0.4988	3.3183	0.0359	-0.0464	-0.2575	-0.0080
43	30.6034	33.6805	-0.4902	3.2633	0.0343	-0.0743	-0.2519	0.0008
44	30.2098	33.3090	-0.4841	3.2243	0.0335	-0.1705	-0.2790	0.0340
45	30.9981	34.0859	-0.5056	3.3638	0.0349	-0.0604	-0.2642	-0.0076
46	30.2771	33.3851	-0.4847	3.2266	0.0352	-0.0613	-0.2307	0.0036
47	30.3221	33.4192	-0.4879	3.2504	0.0345	-0.0795	-0.2353	0.0081
48	28.8981	32.0881	-0.4532	3.0201	0.0369	-0.0795	-0.2670	0.0074
49	30.7912	33.8920	-0.4996	3.3243	0.0333	-0.1020	-0.2580	0.0111
50	29.7016	32.8492	-0.4761	3.1702	0.0359	-0.0900	-0.2651	0.0071

Table C.2: Raw data from analysis of 50 samples in FlightStream at $C_L = 0.80$, $M = 0.2$, sea level standard conditions; X_{ref} at aft CG location, $S_{ref} = 927.11 \text{ m}^2$, $\bar{c} = 18.23 \text{ m}$ (longitudinal reference length), $b_{ref} = 64.6 \text{ m}$ (lateral reference length)

Sample	X_{ref} [m]	X_{NP} [m]	C_{m_α} [1/rad]	C_{L_α} [1/rad]	C_D [-]	C_{y_β} [1/rad]	C_{l_β} [1/rad]	C_{n_β} [1/rad]
1	32.8261	33.3402	-0.0785	3.1407	0.0355	-0.0926	-0.2682	0.0016
2	33.1315	33.6507	-0.0814	3.2515	0.0339	-0.1165	-0.2686	0.0090
3	33.0373	33.5565	-0.0819	3.2793	0.0349	-0.0837	-0.2744	-0.0031
4	31.8967	32.4102	-0.0765	3.0564	0.0358	-0.0725	-0.2145	0.0100
5	32.2818	32.8072	-0.0785	3.1447	0.0358	-0.0752	-0.2341	0.0047
6	33.3857	33.8997	-0.0831	3.3300	0.0350	-0.0843	-0.2771	-0.0035
7	32.8614	33.3826	-0.0816	3.2656	0.0360	-0.0620	-0.2615	-0.0050
8	33.2342	33.7479	-0.0828	3.3209	0.0338	-0.1262	-0.2729	0.0105
9	32.4877	33.0095	-0.0805	3.2103	0.0359	-0.0936	-0.2782	0.0022
10	32.0176	32.5414	-0.0791	3.1630	0.0366	-0.0601	-0.2313	0.0008
11	33.2442	33.7602	-0.0831	3.3312	0.0343	-0.1005	-0.2551	0.0064
12	33.1145	33.6280	-0.0834	3.3381	0.0341	-0.0966	-0.2447	0.0083
13	32.9818	33.4987	-0.0811	3.2429	0.0352	-0.0856	-0.2680	-0.0004
14	33.3198	33.8337	-0.0837	3.3475	0.0329	-0.1501	-0.2555	0.0258
15	31.9798	32.4994	-0.0765	3.0630	0.0358	-0.1061	-0.2581	0.0095
16	32.3194	32.8404	-0.0782	3.1166	0.0354	-0.0854	-0.2560	0.0041
17	33.0884	33.6167	-0.0825	3.2971	0.0348	-0.0887	-0.2691	0.0015
18	31.9545	32.4814	-0.0776	3.1094	0.0357	-0.1063	-0.2464	0.0134
19	33.6103	34.1280	-0.0848	3.3825	0.0322	-0.1868	-0.2675	0.0339
20	32.6055	33.1225	-0.0802	3.2123	0.0360	-0.0525	-0.2304	-0.0007
21	32.3488	32.8689	-0.0785	3.1501	0.0353	-0.1182	-0.2676	0.0128
22	33.3284	33.8476	-0.0839	3.3444	0.0345	-0.0699	-0.2523	-0.0027
23	32.4477	32.9665	-0.0788	3.1576	0.0359	-0.0612	-0.2423	-0.0002
24	32.1945	32.7126	-0.0771	3.0931	0.0345	-0.1634	-0.2824	0.0221
25	32.5453	33.0587	-0.0799	3.2017	0.0335	-0.2113	-0.2874	0.0377
26	31.7934	32.3179	-0.0759	3.0352	0.0360	-0.1015	-0.2611	0.0188
27	32.7185	33.2388	-0.0799	3.2003	0.0356	-0.0606	-0.2394	-0.0013
28	32.3797	32.9020	-0.0799	3.1891	0.0360	-0.0541	-0.2244	0.0030
29	33.3671	33.8776	-0.0808	3.2300	0.0344	-0.0918	-0.2637	0.0019
30	32.9435	33.4622	-0.0825	3.2979	0.0349	-0.1125	-0.2738	0.0066
31	33.2246	33.7263	-0.0837	3.3426	0.0317	-0.2018	-0.2640	0.0402
32	32.8344	33.3544	-0.0814	3.2481	0.0354	-0.0491	-0.2372	-0.0069
33	32.4102	32.9347	-0.0811	3.2346	0.0358	-0.1009	-0.2717	0.0061
34	32.8321	33.3492	-0.0805	3.2126	0.0348	-0.0672	-0.2470	-0.0014
35	32.7754	33.2938	-0.0811	3.2361	0.0347	-0.0925	-0.2597	0.0021
36	32.8726	33.3934	-0.0811	3.2472	0.0344	-0.1535	-0.2903	0.0186
37	33.0514	33.5706	-0.0839	3.3624	0.0359	-0.0555	-0.2567	-0.0084
38	31.3011	31.8349	-0.0759	3.0378	0.0368	-0.1204	-0.2564	0.0166
39	32.0275	32.5553	-0.0776	3.1043	0.0372	-0.0683	-0.2560	-0.0005
40	31.3790	31.9166	-0.0753	3.0029	0.0379	-0.0766	-0.2497	0.0086
41	33.2330	33.7556	-0.0839	3.3403	0.0359	-0.0476	-0.2484	-0.0089
42	33.1907	33.7087	-0.0831	3.3180	0.0359	-0.0464	-0.2575	-0.0096
43	33.1675	33.6805	-0.0819	3.2633	0.0343	-0.0744	-0.2521	-0.0017
44	32.7992	33.3090	-0.0802	3.2252	0.0335	-0.1704	-0.2794	0.0277
45	33.5704	34.0859	-0.0845	3.3635	0.0349	-0.0604	-0.2642	-0.0094
46	32.8684	33.3851	-0.0805	3.2269	0.0352	-0.0613	-0.2307	0.0006
47	32.9044	33.4192	-0.0814	3.2507	0.0345	-0.0794	-0.2353	0.0042
48	31.5542	32.0881	-0.0759	3.0201	0.0369	-0.0796	-0.2666	0.0035
49	33.3748	33.8920	-0.0837	3.3243	0.0333	-0.1020	-0.2578	0.0069
50	32.3265	32.8492	-0.0791	3.1705	0.0359	-0.0899	-0.2651	0.0033